DEVELOPMENT AND EVALUATION OF A NOVEL TECHNOLOGY FOR MONITORING PATIENT MOTION DURING STEREOTACTIC RADIOTHERAPY

by

Parisa Sadeghi

Submitted in partial fulfilment of the requirements
for the degree of Doctor of Philosophy

at

Dalhousie University
Halifax, Nova Scotia
August 2021

TABLE OF CONTENTS

LIST OF TABLES

LIST OF FIGURES

ABSTRACT

Stereotactic Radiosurgery (SRS) and stereotactic Body Radiotherapy (SBRT) are two of the most precise therapeutic radiation delivery techniques available. These techniques involve accurate delivery of high radiation doses to the target volume while minimizing the amount of radiation received by the adjacent healthy tissue. To achieve this precision, patients need to be accurately positioned with respect to the treatment unit, and the position must be maintained throughout the treatment delivery. While immobilization techniques reduce patient motion, they do not eliminate it. Thus, there exists a need for continuous position monitoring during treatment. An ideal monitoring system would provide real-time, high-accuracy measurements of patient position without using ionizing radiation or reliance on deformable surrogates such as skin. Additionally, the ideal system would be insensitive to the thermoplastic immobilization material and would not require direct view of the patient. While multiple monitoring systems are used in practice currently, none meet all of these requirements. Our research is focused on the development of a novel and non-invasive capacitive monitoring method that can fulfill the above-mentioned prerequisites.

This thesis includes four manuscripts. The first, entitled "*A novel intra-fraction motion monitoring system for stereotactic radiosurgery: proof of concept,*" describes the design and implementation of a prototype capacitive monitoring device capable of performing 3D motion detection. The second manuscript, "*Finite Element Analysis of a capacitive array for 6D intrafraction motion detection during stereotactic radiosurgery,*" focuses on the use of finite element analysis to simulate different array designs and introduces a method to compare the sensitivity of different designs to determine a capacitive array design capable of 6D cranial motion detection. The third manuscript, "*Six-dimensional intrafraction cranial motion detection using a novel capacitive monitoring technique: evaluation with human subjects,*" presents the results of a volunteer study with the most promising capacitive array for 6D cranial motion detection. The fourth manuscript, "*Capacitive monitoring system for real-time respiratory motion monitoring during radiation therapy,*" describes the implementation of capacitive monitoring technique for respiratory motion detection during SBRT.

These manuscripts form the basis for design, fabrication, and performance evaluation of capacitive monitoring systems for cranial and respiratory-induced intrafraction motion.

LIST OF ABBREVIATIONS USED

3D	Three-dimensional
6D	Six-dimensional
Linac	Linear Accelerator
FEA	Finite Element Analysis
CBCT	Cone Beam Computes Tomography
SRS	Stereotactic Radiosurgery
SBRT	Stereotactic Body Radiation Therapy
AVM	Arteriovenous Malformations
CSF	Cerebrospinal Fluid
SNR	Signal to Noise Ratio
ADC	Analog to Digital Converter
DIBH	Deep Inspiration Breath Hold
DEBH	Deep Exhalation Breath hold
RPM	Real-time Position Management
RGSC	Respiratory Gating for Scanners
ROI	Region of Interest
CMS	Capacitive Monitoring System
IR	Infrared
MR	Magnetic Resonance

ACKNOWLEDGEMENTS

I would like to thank all the people who have helped me through this project. My supervisor, Dr. Robar, for his guidance and mentorship. My colleagues and fellow students for their friendship and comradery, and the clinical staff at the NSCC for their help and support during the clinical portion of the work.

Above all, I would like to thank my parents for supporting me in my path, and Peter for believing in me even when I did not believe in myself.

Special thanks to Ben and Jelly bean for their companionship that helped me more than they may realize.

CHAPTER 1 INTRODUCTION

1.1 PREAMBLE

This thesis presents a novel technology for continuous motion monitoring for patients during radiation therapy treatment. The system is designed to be modular, non-ionizing, and non-contact. Importantly, the system is insensitive to thermoplastic masks, which are commonly used for patient immobilization during treatment. Development of this technology was done with the aim that the use of such a system during treatment could detect patient motion and help reduce the radiation dose received by surrounding healthy tissue by reducing geometric uncertainty resulting from intrafraction patient motion during stereotactic radiosurgery or radiotherapy.

The objective of this work is to introduce capacitive monitoring as a tool for motion management and design and construct a prototype to investigate the detection capabilities of the system. To this end, this thesis is divided into multiple major bodies of work, each examining one aspect of the design, utilization, or implementation of the capacitive monitoring system for a specific treatment site. The main focus of this research is on cranial motion detection with some additional information for motion monitoring in extracranial treatment sites.

1.2 CANCER AND RADIATION THERAPY

Nearly 1 in 2 Canadians (45 % of men and 43 % of women) is expected to develop cancer during their lifetimes and about 1 out of 4 Canadians (26 % of men and 23 % of women) is expected to die from cancer [12]. Cancer treatments vary based on the pathology

and progression of disease, but most common treatment regimens could include a combination of surgery, chemotherapy, and radiation therapy [13] with roughly 60 % of cancer patients indicated for receiving radiation therapy [14].

Radiation therapy can help by damaging the DNA of the target cells, thus triggering cell death or causing ablative effects [15]. To this end, accurate and precise delivery of radiation is required to localize radiation dose to the target volume while minimizing the damage to healthy tissue.

Radiation therapy can be delivered with internal and external sources. Internal radiation delivery (brachytherapy) involves the placement of the radiation source on the surface of, or within the patient's body to irradiate the target volume. External beam radiotherapy, which is the type of radiation delivery associated with the devices focused on in this thesis, involves directing a radiation source from outside of the patient's body. This treatment can be delivered through different fractionation schemes. Below, we will discuss two major hypo-fractionated delivery regimens which are the focus of this study.

1.2.1 Stereotactic Radiosurgery/Radiotherapy

Stereotactic Radiosurgery and Stereotactic Radiotherapy (SRS/SRT) are the treatment of small volume(s) of tissue within the brain with large doses of radiation delivered in a single or a few treatment fractions. In these methods, high radiation doses are accurately delivered to the affected areas of the brain while minimizing the amount of radiation received by the healthy tissue immediately adjacent to the target.

SRS is one of the most precise and accurate radiation delivery techniques available with high positional accuracy (often within ± 1 mm) and accurate dose delivery to the target volume (within ± 5 %) [16–18].

1.2.1.1 SRS/SRT Indications

SRS is largely used in treatment of small brain tumors and metastases [19–21] secondary to lung, melanoma, breast, renal, and colorectal cancer [22]. Some of the main indications are non-malignant tumors. For example, SRS/SRT offers high control rates and lower likelihood of hearing loss and morbidity compared to surgical alternatives in treatment of acoustic neuroma [23,24] and provides growth control in cases of meningioma with or without prior surgical intervention [24–26]. SRS/SRT is also an important tool for treatment of other brain abnormalities such as deep-seated arteriovenous malformations (AVMs) [27,28] leading to symptomatic relief from seizures and reduction in likelihood of hemorrhage [24]. Functional disorders such as drug resistant epilepsy [24,29,30] and trigeminal neuralgia [29,31,32] can also be treated with SRS/SRT without the risk of peri-surgical complications such as bleeding, infection and post-operative pain.

1.2.1.2 SRS/SRT Treatment Delivery

Since its inception in 1951 by Lars Leksell [33] Stereotactic Radiosurgery treatment delivery methods have been refined significantly. The initial delivery system employed a stereotactic frame and orthovoltage (100keV to 500 keV) x-ray beams, as shown in figure 1.1. The setup involved an arc-centered frame attached to the patient's skull to establish a three-dimensional coordinate system with the principle of having the target in the center

of a semicircular arc and irradiating the target by cross-firing with narrow radiation beams.

This specific setup was first used for the treatment of trigeminal neuralgia [33]. Since orthovoltage x-rays could not provide the required penetration for deeper targets, and Co-60, with an average energy of 1.25 MeV and a half-life of 5.26 years, was already used as a radiation source for external beam radiotherapy [34], a refined SRS treatment delivery system was developed using Co-60 as a radiation source. The first such unit included 179 sources and was used for treatment of arteriovenous malformations (AVMs) , tumors, and functional disorders [35,36].

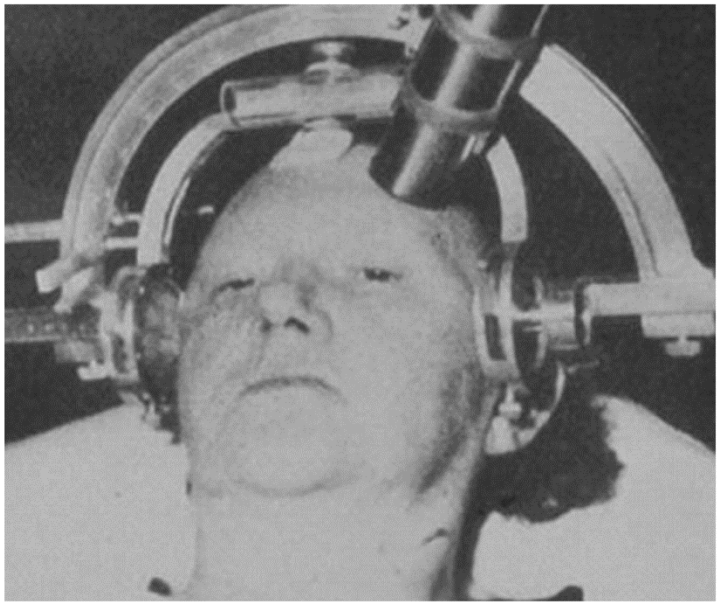

Figure 1.1 First Radiosurgery treatment using a 200 kVp x-ray tube mounted on a stereotactic frame [1].

The promising results of the first unit, led to the development of a second SRS treatment unit capable of delivering circular radiation beams. These machines were referred to as Gamma Knife, as shown in figure 1.2, and are currently manufactured by Elekta (Elekta AB, Stockholm, Sweden). The modern Gamma Knife units use Co-60 as

a radiation source and deliver circularly collimated beams of radiation with different collimation sizes (4 mm, 8 mm, 14 mm, and 18 mm) and radiation treatment is delivered using different collimators, to different stereotactic locations, using differing dwell times [37].

Figure 1.2 Lars Leksell and the first Gamma Knife unit [1].

Following the introduction of Gamma Knife Radiosurgery, multiple attempts were made to adopt this technique on the conventional isocentrically-mounted linear accelerator machine. Earliest examples of linac-based radiosurgery were introduced in 1982 by Betti *et al*. in Buenos Aires [38], followed by Columbo *et al*. in Vicenza [39] and Lutz *et al*. in Boston [40]. Linac-based radiosurgery combines the use of 6 MV to 10 MV x-ray photons with small field collimation (10 mm to 40 mm) to deliver the radiation dose to the target volume. High precision collimation is achieved either in the form of a set of collimators (radiosurgical cones) to define small circular diameter radiosurgical beams or a micro multileaf collimator (MLC), capable of defining small irregularly shaped fields.

Linac-based radiosurgery is performed with high positional accuracy (often within ± 1 mm) and provides accurate dose delivery to the target volume (within ± 5 %) [16–18]. SRS is often used to deliver prescribed doses larger than 10 Gy to small planning target volumes, typically ranging from 1 cm^3 to 35 cm^3 [16]. One advantage of linac-based SRS treatment delivery is that it uses a standard isocentric linac with stringent mechanical and dosimetric tolerances sufficient for radiosurgery and therefore, unlike the Gamma Knife, the machine is not limited to radiosurgery treatment delivery. Furthermore, linac-based radiosurgery and Gamma Knife systems have shown comparable dosimetric outcomes for the same indications [41]. Figure 1.3 illustrates the two modern Gamma Knife and linear accelerator systems used for SRS treatment.

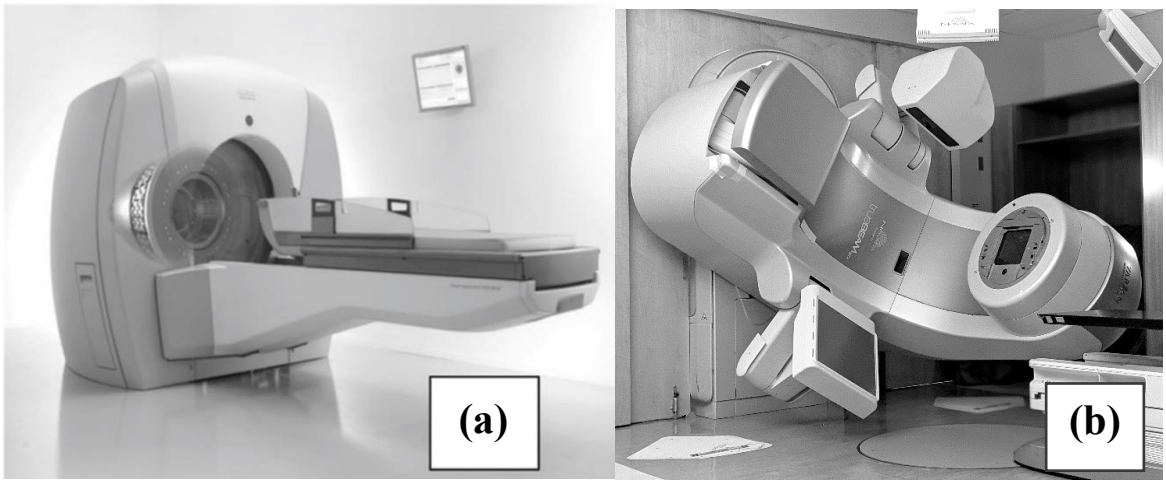

Figure 1.3 Illustrations of SRS treatment delivery systems: (a) Gamma Knife [2], and (b) linear accelerator (Varian TrueBeam STx).

1.2.2 Stereotactic Body Radiotherapy

The success of SRS techniques for cranial treatments led to the adaptation of radiosurgical methods for treatment of extracranial treatment sites. This method of radiation treatment, referred to as Stereotactic Body Radiotherapy (SBRT), most

commonly involves the delivery of a high dose of radiation in 1 to 6 fractions [42]. In order to minimize damage to the surrounding healthy tissue, conforming the high doses to the target and ensuring rapid fall-off of doses away from the target is critical [43]. With improvements in hardware and image guidance, the SBRT technique has become highly effective in the treatment of early stage primary and metastatic cancers in abdominal, pelvic, and thoracic regions as well as spinal and paraspinal areas, with outcomes comparable to surgery and with minimal adverse effects [42–44]. Multiple clinical studies have shown improved outcome and disease control as well as reduced toxicity in SBRT treatment of lung tumors [45,46], liver primary and metastatic tumors [47–49], spinal tumors and metastases [50–52], pancreatic cancer [53,54], and breast tumors [55,56].

1.3 Motion In SRS/SRT and SBRT

A fundamental aspect of the safe application of radiosurgical treatment modalities is the high spatial precision and accuracy of treatment delivery. This includes two aspects: the accuracy of delivering the radiation distribution at the prescribed location, and the sharp dose fall off from the target volume. The large treatment dose and conformal nature of SRS/SRT and SBRT treatments require a high level of confidence in the accuracy of the entire treatment delivery since any spatial inaccuracies in radiation delivery may lead to irradiating normal tissue to dangerously high dose levels that are associated with a much greater risk of long-term toxicity. The accuracy of SRS/SRT and SBRT treatments are generally considered to be approximately 1 mm to 2 mm using modern radiotherapy delivery methods, appropriate quality assurance, and image guidance [43,57]. To this end, minimizing or accounting for patient motion, is an important

step in accurate radiation delivery. While imaging techniques, such as stereoscopic x-ray imaging and Cone Beam CT (CBCT), are often used to ensure accurate patient positioning at the beginning of or at a few time points during treatment, intrafraction patient motion during radiation treatment delivery remains a source of geometrical inaccuracy [58] and is the main focus of this research. The following section provides a review of different patient motion and monitoring techniques for SRS/SRT and SBRT.

1.3.1 Cranial Motion Observed in Patient Studies

SRS and SRT treatments deliver a high radiation dose in a single or a few fractions and therefore are often accompanied by stringent patient immobilization during treatment. While immobilization can reduce the intrafraction motion, it cannot fully eliminate it [7–9,59,60]. Several studies have been conducted to investigate the extent and patterns of intrafraction cranial motion during SRS/SRT treatment. Multiple studies have shown motion to be highly patient dependent with some patients consistently exhibiting larger and more frequent cranial motion than others [4,60,61]. The largest study performed by Murphy *et al*. identified 18 patients out of 250 (7.2 %) who exhibited repeated (three or more instances of) translational shifts larger than 2 mm during one treatment, while 109 patients (43.6 %) moved by this amount only once or twice [4,60,61]. Furthermore, the treatment duration has been shown to play an important role in the extent of motion exhibited by patients [59,62–64]. Tarnavski *et al.* investigated the frequency of patient motion during the first five minutes of treatment, the second five minute interval of treatment, and after the first ten minutes of treatment time had passed. They reported a significant increase in frequency of large patient motion (more than 2 mm of translation or 2° of rotation) with progression in treatment duration [63]. Similarly, Mangesius *et al.*

investigated intrafraction patient motion during treatments that were no longer than 20 minutes, and reported better positioning accuracy within the first six minute interval of treatment delivery compared to the rest of the treatment [62]. Guckenberger *et al.* reported a significant increase in intrafraction motion for treatments longer that 23 minutes, [59] and Kang *et al.* recommended different treatment margin considerations for longer treatment durations [64].

The immobilization technique utilized during treatment can also affect the intrafraction motion. The SRS immobilization techniques fall into two major categories of frame-based and frameless immobilization. Frame-based immobilization involves the attachment of a metal stereotactic frame to the skull using metal pins. The frame serves as an immobilizer as well as a localizer by providing a reference frame for patient positioning during treatment. To this end, a localizer box is used for imaging to define a coordinate system around the cranium. Figure 1.4 shows a frame-based immobilizer and a localizer box. The fiducials embedded in the localizer box appear in the CT data and define a three-dimensional Cartesian coordinate system, referred to as "stereotactic coordinates".

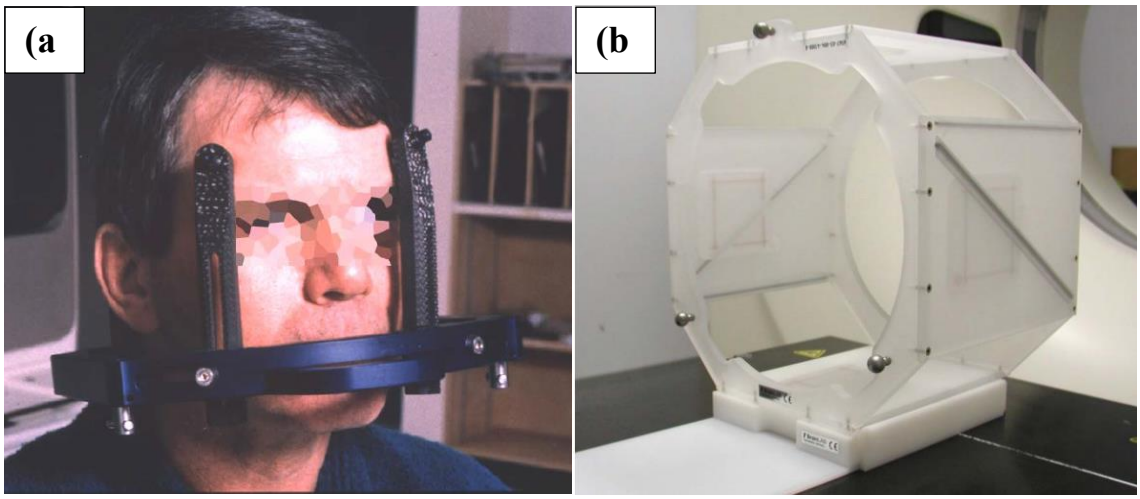

Figure 1.4 (a) Stereotactic head-frame system affixed to the skull (Brainlab AG) and (b) stereotactic localizer box [3].

Alternatively, non-invasive thermoplastic masks can be molded to the patient's cranium and facial features to produce a relocatable frameless immobilization device. There are a variety of mask systems available for frameless immobilization, some of which are shown in figure 1.5. Figure 1.5 (a) [4] shows a simple patient-specific thermoplastic mask molded to the facial features (Civco Medical, Iowa). Figure 1.5 (b) shows a combination of thermoplastic mask and a patient specific dental mold (BrainLab AG, Munich). The mold is used as a bite block to further help in reducing cranial motion [5]. The system can also be used without the bite block, as shown in figure 1.5 (c) [6]. Figure 1.5 (d) shows a patient fitted with a near-rigid relocatable head frame (Aktina Medical, NY). This system uses a head fixation device coupled with a bite block attached to a vacuum device via tubing that provides suction. The bite block contains a patient-specific dental mouthpiece with continuous mild vacuum suction to the upper hard palate. An external component consists of the dental mouthpiece secured to a metal arch frame that

is affixed to the treatment couch. The patient-specific thermoplastic head support is formed by creating an impression of the back of the skull [7].

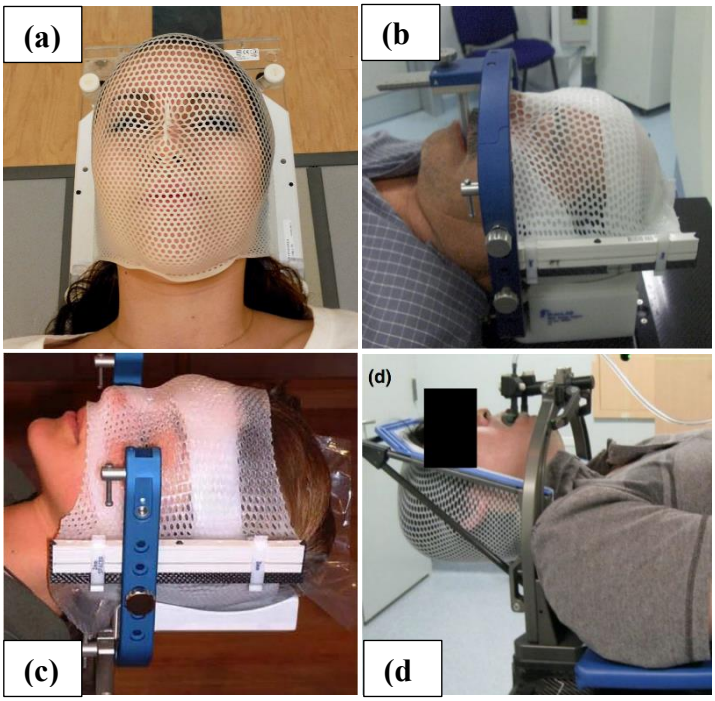

Figure 1.5 (a) A full-face patient-specific thermoplastic mask molded to the facial features [4]. (b) A combination of thermoplastic mask and a patient-specific bite block [5]. (c) A similar system can be used without the use of bite block [6]. (d) A thermoplastic "cradle" coupled with a bite block and an active suction system [7].

Frame-based systems are generally considered to be the gold standard for their ability in restricting intrafraction motion [7,8]. A study by Ramakrishna *et al.* evaluated 3-dimensional intrafraction motion for 102 cases of frame-based and 110 cases of frameless immobilization by acquiring pre-treatment and post-treatment stereoscopic x-ray images [8]. The results shown in figure 1.6 illustrate a cumulative histogram of the 3D intrafraction motion for frame-based and frameless immobilization. The data indicate that about 22 % of patients with frameless immobilization exhibited intrafraction motion over

1 mm while the number was reduced to about 4 % for the patients with frame-based immobilization. Furthermore, the frameless immobilization allowed for a larger degree of motion (< 2.6 mm) compared to the extent of motion observed with frame-based immobilization (< 1.6 mm).

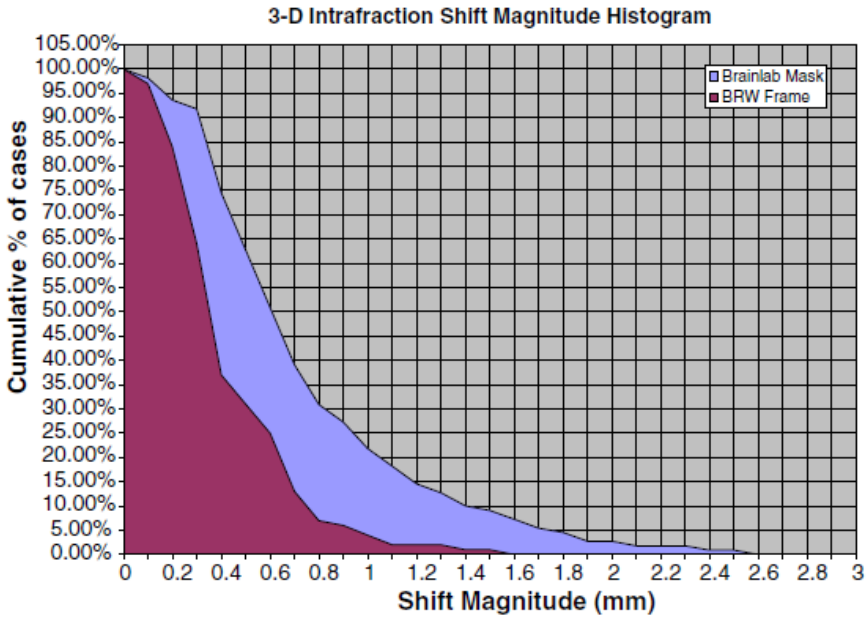

Figure 1.6 A histogram of 3D intrafraction motion for frame-based (BRW) versus mask-based (Brainlab Mask system) immobilization [8].

However, frame-based immobilization systems are invasive, require longer recovery time, and patients could experience side effects such as pain and bleeding [65]. Additionally, with frame-based systems the process of imaging, planning, and treatment needs to happen in one day, and cranial motion is still not fully eliminated. As a result, rigid, relocatable mask-based immobilization techniques are commonly used during SRS/SRT treatment delivery. As such, multiple studies have been performed to investigate cranial intrafraction motion using frameless immobilization techniques.

A study into translational and rotational intrafraction motion [9] using the Brainlab SRS mask system was conducted with a cohort of 40 patients by Gevaert *et al*. They acquired stereoscopic x-ray images before and after the treatment to investigate the degree of patient motion during treatment. The results shown in figure 1.7 illustrate intrafraction translational motion as high as 0.9 mm, 1.75 mm, and 1.4 mm in vertical, longitudinal, and lateral directions, respectively. Maximum intrafraction rotations were reported around the vertical, longitudinal, and lateral axes as 1.25°, 0.9°, and 1.6°, respectively. While intrafraction motion over 1 mm and 1°is observed in some cases, a population study of 967 treatment setups performed by Badakhshi *et al.* concluded that the average proportion of intrafraction translational motions exceeding 1, 2, and 3 mm in each direction were 12 %, 3 %, and 1 %, respectively [66,67].

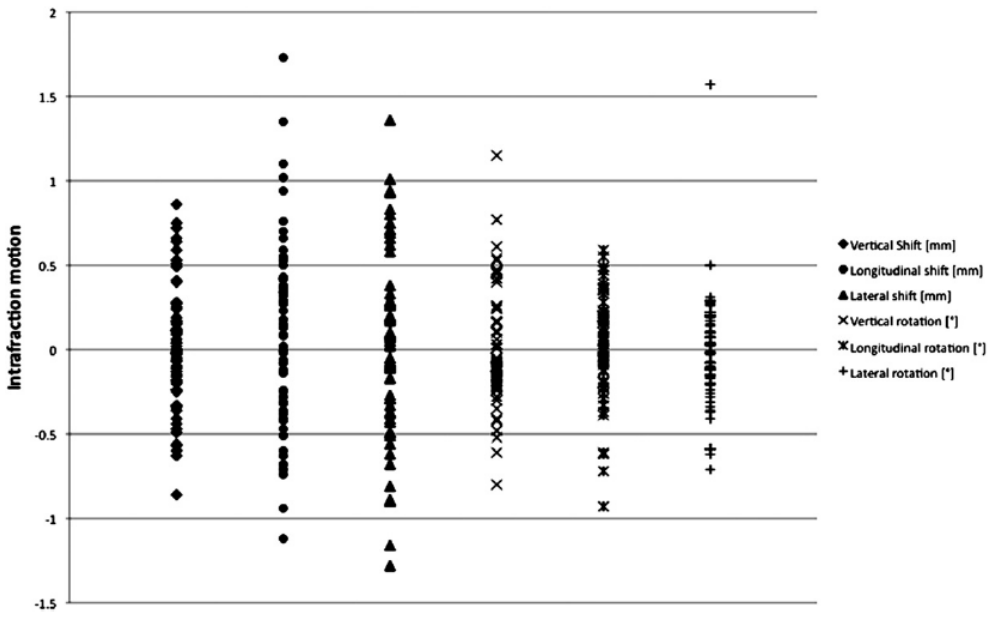

Figure 1.7 Six-dimensional intrafraction cranial motion information during SRS treatment using frameless immobilization [9].

While large intrafraction motion is often observed in a smaller cohort of patients and the extent of intrafraction motion may vary based on the mask system used [7], it is evident that intrafraction motion can occur during SRS/SRT treatment, and therefore the use of a patient position monitoring system is recommended in conjunction with frameless immobilization techniques [4,9].

1.3.2 Management and Monitoring of Cranial Motion in SRS/SRT

Multiple non-invasive monitoring devices are commercially available to detect intrafraction motion during SRS/SRT treatment. In addition to increasing the accuracy of treatment delivery, accurate and near real-time patient position monitoring may allow for less rigid and more comfortable immobilization for patients.

1.3.2.1 Motion Monitoring Techniques

Some non-invasive motion monitoring systems employ stereoscopic imaging to provide 3D motion information. Stereoscopic imaging uses two different views of the same scene in a fixed geometry. The system identifies spatially invariant or known features in the first image (feature extraction) and locates the corresponding features in the second image (feature correspondence). The system then computes the 3D coordinates of the features using the intersection of the perspective projections. Therefore, the features must be clearly visible in both images. These features could be original parts of the image scene or could be added to the image [68,69]. Stereoscopic imaging systems, such as ExacTrac (Brainlab AG, Munich), implement this method with x-ray images acquired simultaneously from the patient, providing 3D positional information by using the bony anatomy as stereoscopic features. Repeating the imaging

process could provide information regarding patient motion between discrete time points. Due to the nature of x-ray imaging, the system provides motion information by detecting the cranium rather than relying on surrogates and provides positional information with sub-millimeter and sub-degree accuracy [70,71]. However, this form of imaging uses ionizing radiation and is often not continuous.

The premise of stereoscopic imaging can also be used in conjunction with optical imaging in the form of photogrammetry. A known pattern of structured light projected onto the patient adds known features to the image. The cameras use these features to extract 3D information. This method provides continuous motion monitoring without the use of ionizing radiation. However, this method detects facial motion by monitoring the patient skin during treatment. Using a deformable surrogate such as skin to determine cranial motion could lead to false positive and false negative results [72,73]. Additionally, the system requires unobstructed view of the target to perform motion detection. As a result, less restrictive open-faced mask systems need to be used in conjunction with the optical monitoring system. Most recently, MR imaging systems have been used in conjunction with linac treatment units. These MR-Linacs provide 2D snapshots in near real-time to monitor patient motion. However, patients with metal implants, for example, non-MRI-compatible pacemakers and prosthetics, or large patients cannot be imaged using this technology [74].

1.3.3 Extracranial Motion

Respiratory motion is one of the most prevalent causes of extracranial intrafraction motion in treatment of thoracic, abdominal, and pelvic tumors [75–78]. A recent review

showed that live respiratory motion management plays a large factor in reduction of toxicity outcomes in these treatment sites [78]. With regards to extracranial SBRT, this thesis focuses on the respiratory motion as the most common source of intrafraction motion.

1.3.4 Management and Monitoring of Extracranial Motion During SBRT

Various attempts have been made to synchronize the delivery of radiation with respiration as early as 1989 [79]. Since then, different techniques and technologies have been introduced to reduce or mitigate the effects of respiratory-induced motion.

In general, these techniques fall into two major categories of motion suppression and motion monitoring [74]. A detailed description of these methods is provided below.

1.3.4.1 Motion Monitoring Techniques

The first step to minimizing the effects of respiratory-induced motion is restricting the motion [76]. This can be achieved using breath hold maneuvers such as deep inspiration breath hold (DIBH) or deep expiration breath hold (DEBH) where the patient is coached to hold their breath at the deep inhale or exhale position and radiation is delivered in the absence of normal respiratory motion. A reproducible DIBH state is advantageous for treating thoracic tumors. Not only can it significantly reduce respiratory tumor motion, but it also changes internal anatomy in a way that often protects critical normal tissues by moving the heart posteriorly and inferiorly away from the breast which may reduce cardiac and lung toxicity [74,75]. However DEBH maneuvers have reportedly shown higher reproducibility and stability [80,81].

Alternatively, abdominal compression devices can limit respiratory motion by applying external pressure to the upper abdominal region, forcing the patients to adopt shallow breathing. This technique has been shown to minimize respiratory-induced tumor motion for lung and liver targets [76,82,83].

Spirometry techniques can also be used to measure and monitor the airflow into the lungs which in turn, are used to estimate the volume of air inside the lungs. To this end, the patient is instructed to breathe through a mouthpiece while wearing a nose clip to ensure breathing occurs exclusively through the mouth. Additionally, a scissor valve can be added to maintain the air volume at a pre-specified level, therefore ensuring the reproducibility of the DIBH/DEBH states [74–76].

Another technique that aims to limit the respiratory-induced motion during treatment is gating, i.e., synchronizing the treatment delivery with respiratory motion by gating the treatment beam. The treatment beam can be turned on and off at specific breathing phases or amplitudes, leading to the treatment delivery during a portion of the breathing cycle [58,76].

Multiple non-invasive monitoring devices are available to provide information regarding the respiratory motion to facilitate gating or breath-hold maneuvers. A belt equipped with pressure sensors and placed around the abdominal section of the patient can detect respiratory motion and monitor the respiratory cycle. This information can be used for respiratory gating or monitoring DIBH or DEBH states [74]. The Anzai belt system (Anzai Medical, Tokyo) is an example of this technology.

Infrared markers can also be used to monitor the breathing cycle during treatment. The combination of infrared (IR) markers placed on the patient's chest or abdomen, and a camera that monitors the position of the markers, can provide continuous information regarding the respiratory cycle. Examples of this technology are the Real time Position Management (RPM) system and the Respiratory Gating for Scanners (RGSC) system (Varian Medical Systems, California) which use a plastic block with different arrangements of IR reflective markers where the plastic block is placed on the chest or abdomen and monitor the motion using a room-mounted IR-sensitive camera.

Optical stereoscopic systems can also be used to provide continuous respiratory motion information [74]. These systems require room-based cameras and a direct unobstructed view of the target.

1.4 Capacitive Monitoring Technique

The focus of this thesis is a technology that uses capacitive monitoring to provide continuous intrafraction motion monitoring during SRS and SBRT treatment. Below, we describe the fundamental physics behind the design and development of this technology.

1.4.1 Capacitance

Capacitance is a quality associated with a conductor or arrangement of conductors and is the ratio of the charge stored on the conductors (Q) and the voltage applied to the conductors (V) as shown in equation 1.1, where C represents capacitance.

$$C = {}^{Q}/_{V} \qquad \text{eq 1.1}$$

By definition, capacitance can be defined for any single conductive object capable of holding electric charge, where the electric potential difference is measured between the object and ground [84]. This is referred to as self-capacitance [84]. Mutual capacitance, most commonly referred to as capacitance, is defined for an arrangement of two conductive objects in close proximity. Capacitors can be used to store charge and electric potential energy and are commonly used in a variety of electric circuits. The stored potential energy (W) can be calculated using equation 1.2 where C and V represent the system capacitance and voltage across the capacitor, respectively.

$$W = {}^{1}/_{2}\ CV^{2} \qquad \text{eq 1.2}$$

In general, the capacitance of a system is solely dependent on the system geometry (shape, size and separation of the two conductors) and the dielectric material between the conductors [85]. We present a detailed discussion on the behavior of dielectric materials in the presence of an electric field in the following section.

1.4.1.1 Polarization Effects

When a dielectric material is introduced in the gap between the conductors, it results in an increase in the capacitance. This capacitance increase can be explained from a molecular point of view. The dielectric response to the external electric field depends on the type of dielectric used. Dielectrics may be polar or non-polar. Polar dielectrics have molecules with permanent electric dipole moments. In the absence of an external

electric field, the dipole molecules are oriented randomly. When an external field is applied, the dipoles rearrange themselves to further align with the field. This behavior is illustrated in figure 1.8. Even though the alignment is not complete due to random thermal motion of the molecules, the aligned dipoles generate an electric field. This electric field is smaller in magnitude and in opposite direction compared to the external electric field.

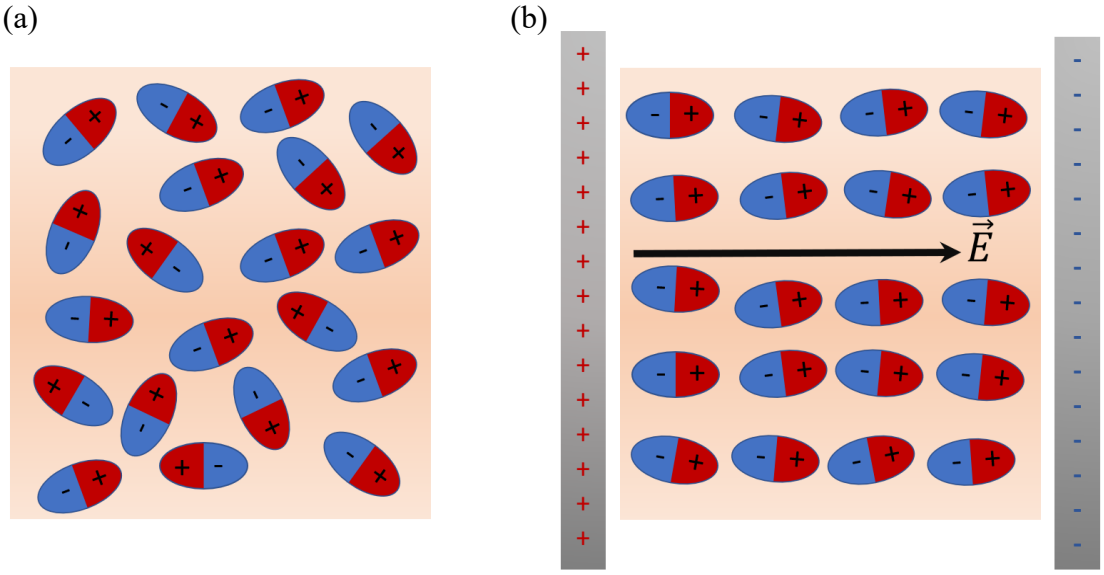

Figure 1.8 (a) Orientation of polar molecules in the absence of an electric field.
(b) Alignment of molecular dipoles in the presence of external electric field resulting from the charged parallel plate capacitor and $\vec{E}$ represents the total electric field.

The second type of dielectrics is non-polar, with molecules that do not possess permanent electric dipoles. When exposed to an external electric field however, electric dipole moments are induced in the molecules. Figure 1.9 illustrates the behavior of a non-polar dielectric material in the absence and presence of external electric field. Induced dipole moments align in the field and generate an electric field that is smaller in magnitude and in opposite direction compared to the external electric field.

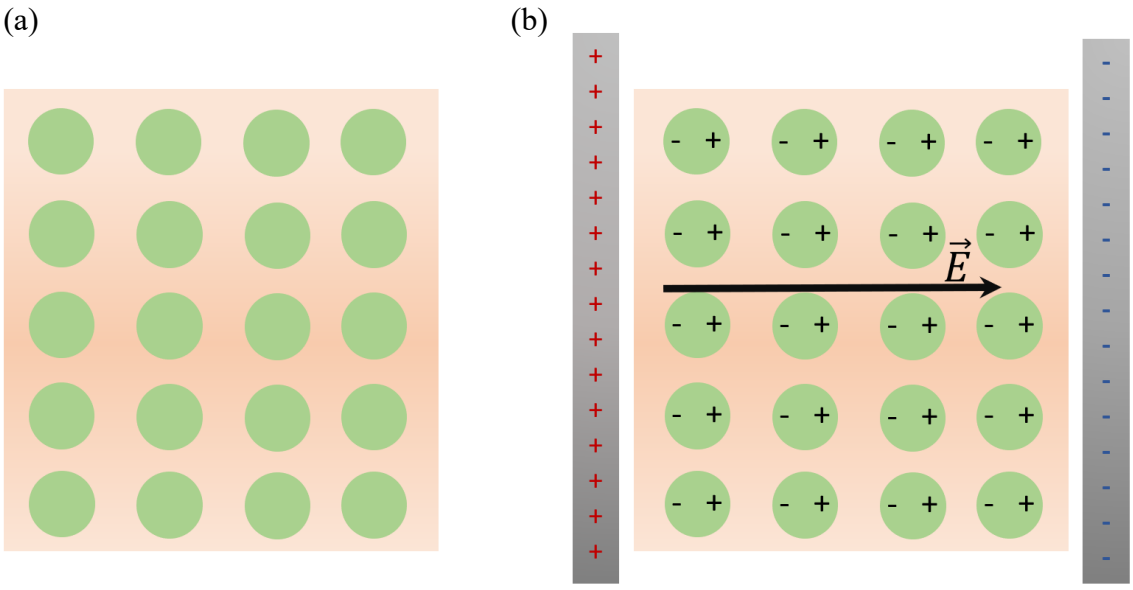

Figure 1.9 (a) Orientation of non-polar molecules in the absence of an electric field. (b) Induced electric dipole moments in the presence of external electric field resulting from the charged parallel plate capacitor and $\vec{E}$ represents the total electric field.

The effect of the dielectric material on the net electric field depends on the average electric field produced by the alignment of the dipole moments within the dielectric. In general, an electric dipole moment ($\vec{p}$) resulting from a negative and a positive point charge (q) separated by a distance of $\vec{d}$ is defined by equation 1.3 where $\vec{p}$ and $\vec{d}$ vectors point from the negative charge towards the positive. The polarization of a region ($\vec{P}$) is defined as the sum of dipole moments ($\vec{p}$) per unit volume (V) as shown in equation1.4. Since electric fields resulting from the arranged dipoles are in the opposite direction of the polarization vector ($\vec{P}$), the total electric field resulting from the polarization within the dielectric ($\vec{E}_p$) can be calculated using equation 1.5, where ε_o is vacuum permittivity.

$$\vec{p} = q\,\vec{d} \qquad \text{eq 1.3}$$

$$\vec{P} = \sum \vec{p} / V \qquad \text{eq 1.4}$$

$$\vec{E}_p = - \vec{P} / \varepsilon_o \qquad \text{eq 1.5}$$

On the other hand, the electric field resulting from the arranged dipoles are in the opposite direction of the external field ($\vec{E}_o$). Therefore, the total electric field ($\vec{E}$) can be defined by equation 1.6.

$$\vec{E} = \vec{E}_o + \vec{E}_p = \vec{E}_o - \vec{P} / \varepsilon_o \qquad \text{eq 1.6}$$

Since the polarization and dipole arrangement is a direct result of the external electric field, in most cases (with some exceptions such as ferroelectric materials), the polarization ($\vec{P}$) is linearly proportional to the external electric field ($\vec{E}_o$) and the total electric field ($\vec{E}$). Such materials are referred to as linear dielectrics and the relationship between the polarization ($\vec{P}$) and total electric field ($\vec{E}$) can be described by equation 1.7, where the coefficient χ_e is referred to as electric susceptibility.

$$\vec{P} = \varepsilon_o \, \chi_e \, \vec{E} \qquad \text{eq 1.7}$$

Combining equations 1.6 and 1.7 results in equation 1.8, where ε_r is the relative dielectric constant.

$$\vec{E}_o = (1 + \chi_e)\vec{E} = \varepsilon_r \, \vec{E} \qquad \text{eq 1.8}$$

Since electric susceptibility is a positive value, the relative dielectric constant is always larger than one, and therefore, the presence of dielectric material in the capacitor will always result in a decrease of the total electric field. Equation 1.9 describes the relationship between the electric potential (V) and electric field ($\vec{E}$) according to Maxwell's equations, where a decrease in the electric field leads to a decrease in electric potential. Since capacitance of the system is inversely related to the electric potential (equation 1.1), the presence of a dielectric material leads to an increase in capacitance of the system.

$$\vec{E} = -\nabla V \qquad \text{eq 1.9}$$

1.4.1.2 Frequency Effects

The description in the previous section shows linearity between the external electric field and the total field resulting from the superposition of the external field and dipole-induced electric field as per equation 1.8. As such, if the external field is oscillating, the total electric field would be oscillating as well. Since polarization is directly correlated to the electric field (equation 1.7), this affects the behavior of the dipoles and results in the absorption of electric energy by the dielectric subjected to an alternating electric field [86–88]. This effect is known as dielectric loss. As a result, the dielectric constant (permittivity) becomes a function of the electric field oscillation. The dielectric function of a material is generally described as a complex number using equation 1.10 below, where ε' is the relative permittivity of the material and ε'' is the loss factor. The loss

factor is defined by equation 1.11, where σ is the total conductivity of the material, ε_o is the permittivity of free space, and ω is the angular frequency [88].

$$\varepsilon = \varepsilon' - j\varepsilon'' \qquad \text{eq 1.10}$$

$$\varepsilon'' = {}^{\sigma(\omega)}/_{\omega\varepsilon_o} \qquad \text{eq 1.11}$$

It is important to note that conductivity is also frequency dependent [89–91] and can be defined using the universal dynamic response model, as shown in equation 1.12, where σ_o is the conductivity in direct current (DC) conditions and A is a coefficient dependent on the material and thermal conditions [89,92].

$$\sigma(\omega) = \sigma_o + A\,\omega^n \quad , \quad 0 < n < 1 \qquad \text{eq 1.12}$$

It should be noted that conductivity is not a binary attribute. As such, conductors used in real-life have some inherent resistance. Similarly, dielectric materials can have some inherent electrical conductivity. The next section provides a detailed review on the conductivity and permittivity of biological tissue.

1.4.2 Electrical Conductivity of Human Body

In this research, we are focused on the behavior of biological materials in the presence of electrical fields. The dielectric properties of biological tissue result from interactions between the electric field and the biological tissue on a cellular and

molecular level. Tissues also have finite ionic conductivities associated with the nature and extent of their electrolyte content and ionic mobility [10,88,93,94].

In general, the behavior of the biological tissue in alternating fields can be explained based on equations 1.10-1.12. An increase in electric field frequency has been experimentally observed to result in an increase in conductivity and a reduction in permittivity [10,88,95]. Figure 1.10 displays the frequency-dependent change in permittivity and conductivity for a biological sample (spleen) [10].

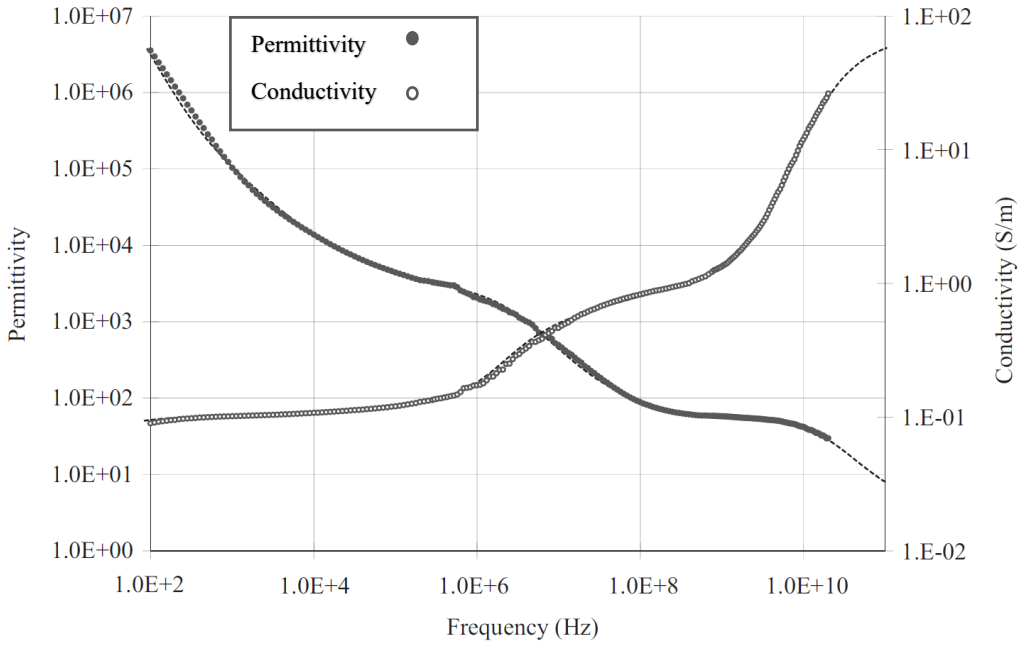

Figure 1.10 Frequency- dependant change in permittivity and conductivity for a biological sample (spleen) [10].

Different reports of conductivity and permittivity of biological tissues have been published. The reported values cover a wide range depending on the sample, method of measurement, and sample temperature [10,88,95–97]. Most reported values are measured on excised tissue of different animals and are prone to underestimations of the conductivity [98,99]. Even conductivity measurements performed on living intracranial tissue samples in patients with brain tumors have shown inter- and intra-patient variations [98]. Conductivity values reported in table 1.1 for grey matter, white matter, and cerebellum are acquired using experimental measurements fitted to theoretical equations at human body temperature (37°C) [10,96]. Conductivity of human cerebrospinal fluid (CSF) at body temperature has been reported by Bauman *et al.* as 1.79 S/m [99]. A review of electrical properties of bone performed by Singh *et al.* reported that conductivity values can vary based on the sample [100], but in general, bone exhibits low conductivity in the range of 4.5 $\times 10^{-3}$ S/m to 10^{-2} S/m. Skin also exhibits low conductivity with values around 10^{-5} S/m at low frequencies [101] and is considered an insulator [102]. Muscle tissue possesses a conductivity of 0.2 S/m to 0.3 S/m [95]. Cranial tissue conductivity values in a DC electric field are listed in table 1.1.

The information in table 1.1 is used in the modelling of the cranium for biomedical applications with skin and bone modelled as insulating layers enclosing a conductive core (brain) [103,104]. Alternatively, more detailed models of layered volumes with different brain tissues incorporated into the model can be used to simulate the behavior of cranial tissue in the presence of electric field [103,104]. The relative dielectric constant values for bone [96] and skin [96] are reported as 14.9 to 22.1 and 10^4 to 10^6, respectively.

In general, the conductivity of human body is primarily due to the electrolyte content, and tissues with higher electrolyte content show higher conductivity [105]. As such, multiple studies have looked at the experimental and theoretical behavior of different concentrations of electrolytes in alternating fields of different frequencies [96,106]. They concluded that higher concentration electrolytes exhibit higher conductivity and the relationship holds up to at least the 10 MHz frequency range [96,106].

Table 1.1 Conductivity values for intracranial tissue.

Tissue	**Conductivity (S/m)**
Cerebrospinal fluid (CSF)	1.79
Grey matter	1.03
Cerebellum	0.89
White matter	0.47
Brainstem	0.47
Muscle	0.2 - 0.3
Bone	≤ 0.01
Skin	10^{-5}

In the context of our study, skin and bone are considered non conductive and cranial tissue (due to its higher electrolyte concentration) is considered conductive. A more detailed discussion is provided in chapter 3.

1.4.3 Capacitive Sensing

The conductivity of human tissue is a feature that can be leveraged in capacitive sensing. In a simple case of an ideal parallel plate capacitor, two conductive plates are placed in proximity of each other to form a capacitor. Ignoring the fringe field effects, the system capacitance (C) can be defined by equation 1.13, where (A) is the surface area of the plate, (d) is the distance between the conductive plates, (ε_r) is the relative permittivity of the dielectric material in-between the plates, and (ε_o) is the permittivity of vacuum with a value of 8.854×10^{-12} F/m.

$$C = \varepsilon_r \varepsilon_o {}^{A}/_{d} \qquad \text{eq 1.13}$$

Now consider replacing a conductor plate with a human body (hand) where the human motion would result in a change in distance (d) and, subsequently, a change in capacitance. This sensing mode is referred to as the loading mode and is illustrated in figure 1.11(a). This method is used in detecting human hand gestures in air [107] as well as its proximity to objects [108], and tracking a human's position on conductive tile flooring [109]. Alternatively, the human body can be introduced in between two capacitors to alter the electric field. This detection method is often used to increase operator safety and detect the presence of workers in the vicinity of production lines [110], for example. This method of sensing can be accomplished through two different modes, namely the shunt mode and the transmit mode. In both cases the human body is introduced into the field. In shunt mode, the body effectively becomes a grounded shield as the electric field lines from the conductive plate couple into the hand and are directed away from the second

conductive plate forming the original capacitor [11] as illustrated in figure 1.11 (b). Alternatively, if the body lies close to or contacts the conductive plate, the body becomes an extension of the conductive plate. The capacitance now increases as a function of body proximity to the conductive plate [11]. This mode is illustrated in figure 1.11 (c).

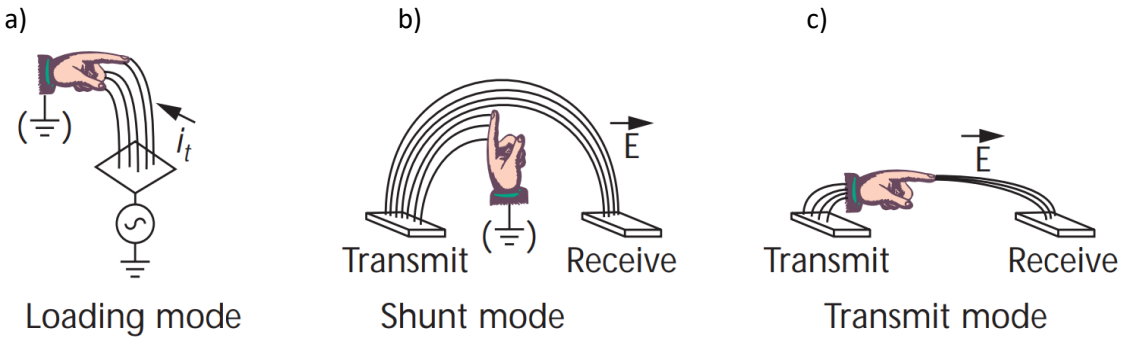

Figure 1.11 Different modes of capacitive sensing: (a) loading mode, (b) shunt mode, and (c) transmit mode [11].

1.5 Research Objectives

This thesis explores the use of capacitive monitoring as a continuous motion monitoring system during radiation therapy treatment, primarily for cranial motion detection in SRS/SRT, but the technology has also been extended for respiratory motion management in SBRT. An ideal monitoring system would provide real-time, high-accuracy measurements of patient position without using ionizing radiation or reliance on deformable surrogates such as skin. Additionally, the ideal system would be insensitive to the thermoplastic immobilization material and would not require direct view of the patient. Our research is focused on the development of a novel and non-invasive capacitive monitoring method that can fulfill the above-mentioned prerequisites. A series

of manuscripts is included, addressing the following separate research objectives: proof of concept for capacitive monitoring and clinical potential, optimizing the capacitive array design to detect cranial rotation and translation motion, investigation of system performance through a volunteer study, and adaptation of the technology for respiratory motion detection.

Manuscript 1 is presented in chapter 2 and addresses the first research objective. It describes the design and implementation of a prototype capacitive monitoring device capable of performing 3D motion detection for SRS/SRT. This work also investigates the effect of radiation on the detection system output, as well as the capability of the monitoring system to detect the cranium through the thermoplastic immobilization device.

Manuscript 2 is presented in chapter 3 and addresses the second research objective. Following the proof-of-concept established in manuscript 1, it aims to identify a more optimal array geometry using finite element analysis to simulate different designs. This study develops a method to compare sensitivities among different designs to determine a capacitive array design capable of 6D cranial motion detection.

Manuscript 3 is presented in chapter 4 and addresses the third research objective. It presents the results of a human volunteer study with the most promising capacitive array for 6D cranial motion detection as identified in manuscript 2. The study evaluates the performance of the array with different cranium sizes and shapes.

Manuscript 4 is presented in chapter 5 and addresses the fourth research objective. It describes the extension of the capacitive monitoring technology for respiratory motion

detection in SBRT. This includes prototype design, testing, and performance comparison with a commercial system.

CHAPTER 2 A NOVEL INTRAFRACTION MOTION MONITORING SYSTEM FOR STEREOTACTIC RADIOSURGERY: PROOF OF CONCEPT

2.1 PREAMBLE

The following manuscript serves as a proof of concept for the capacitive monitoring technique and shows that the system is capable of intrafraction cranial motion detection during SRS treatment. The manuscript describes the design of capacitor plates that act as motion sensors. A capacitive array is designed to detect cranial translation motion and the performance of the array was tested with the help of a volunteer. Additionally, the stability of the system was investigated with radiation present. The system was shown to be insensitive to the thermoplastic mask and able to detect the cranium within. The system is designed to be modular, non-ionizing, and non-contact.

The following chapter only differs from the below published manuscript in minor editorial details. Publication: P. Sadeghi, J. Lincoln, EA Avila Ruiz, and J. L. Robar. "A novel intrafraction motion monitoring system for stereotactic radiosurgery: proof of concept." *Physics in Medicine & Biology* 63, no. 16 (2018): 165019. https://iopscience.iop.org/article/10.1088/1361-6560/aad643/meta.

2.2 ABSTRACT

The purpose of this work was to develop a prototype system for continuous, three-dimensional (3D) monitoring of patient cranial motion during stereotactic radiosurgery. Using novel capacitive detector plates, the goal was to provide detection of cranial

position inside a thermoplastic immobilizing mask, without relying on skin monitoring or use of ionizing radiation.

A novel capacitive detector array was used to detect cranial translations with sub-millimeter accuracy. The array was comprised of four conductive plates arranged around the cranium. One superior plate was positioned at the cranial vertex, two lateral plates were positioned in sagittal planes at the lateral aspects of the cranium, and one plate was located in a coronal plane anterior to the face. The system was calibrated by parameterizing the capacitive signal for each dimension as a function of spatial translation. The detector array performance was evaluated with the help of a volunteer in the absence of radiation. Separately, possible effects of electromagnetic interference and irradiation in the linac suite were assessed.

Detector plates mounted at 1 cm original distance to the thermoplastic mask can detect sub-millimeter lateral and superior cranial motion. Detection of sub-millimeter anterior motion is possible when the plate is mounted closer to the patient (5-10 mm). No signal interference was observed when the capacitive array was irradiated.

Our prototype detector array provides continuous, 3D translation detection with sub-millimeter precision. The signal provides sufficient signal to noise ratio (SNR) and is stable in a linac room environment and in a direct radiation beam. The detector plate is sensitive to the position of the cranium inside a mask and offers the advantage of being insensitive to the mask itself. Future work will involve modifying the array to detect patient rotation.

2.3 INTRODUCTION

Techniques such as stereotactic radiosurgery (SRS) and stereotactic radiation therapy (SRT) require high patient positioning accuracy [57,64,111], and most approaches use stringent patient immobilization during treatment delivery. Commonly, rigid, relocatable mask systems are employed, but these have been reported to allow a degree of patient motion during the treatment [7–9,59,60,112]. For example, a 3D intrafraction shift magnitude of up to 2.6 mm [8] has been observed when using a relocatable stereotactic frame with a thermoplastic mask (Brainlab Cranial Mask System, Brainlab AG). Therefore, the use of a patient position monitoring system is recommended in conjunction with the frameless immobilization technique [4]. In addition, accurate and near real-time patient position monitoring may allow for less rigid and more comfortable immobilization for patients.

The ideal monitoring system would provide continuous positional information using non-invasive and non-ionizing methods. Additionally, a reliable monitoring system should use stable surrogates for monitoring to reduce false positive response rate. Multiple monitoring systems are commercially available, but none fulfills all the above requirements. Stereoscopic x-ray imaging systems provide single images of the patient position using ionizing radiation [71,113]. Optical surface monitoring methods [72,114–116] on the other hand, provide continuous monitoring without the use of ionizing radiation. They use skin as a surrogate for patient motion and therefore require sections of the thermoplastic immobilization device to be removed, which leads to a less restrictive immobilization device. In addition, using a deformable surrogate such as skin could result in false positive and false negative responses [72,73].

In this paper, we introduce a novel capacitive monitoring system for continuous monitoring of patient motion during SRS treatments. We present a prototype system that is passive and produces near real-time positional data using the principles of capacitance. This approach was explored because i) the human body offers a high permittivity compared to plastics, allowing sensing of the entire cranium inside the mask, but not the mask itself, ii) capacitive proximity sensors can be read out at sufficient temporal frequency (e.g., with 1 ms to 128 ms sampling period) [117], and iii) in concept, capacitive plates can be fabricated with minimal thickness, resulting in low attenuation of megavoltage (MV) photon beams. Finally, there is a precedent of using capacitive sensors on the treatment platform, for example, as a collision sensor integrated into on-board imaging systems (e.g. Truebeam, Varian Medical Systems, Inc., Palo Alto, USA).

2.4 Materials and Methods

The following section provides a description of the process of detector and capacitive array design. It also provides the details of the experimental methods used for array calibration and stability measurements.

2.4.1 Detector Design

The proposed detector leverages the physics of capacitance by placing conductive plates proximal to the cranium. In a simple case of parallel plate capacitors, the system capacitance can be determined using equation 2.1, where A and d denote the area of the parallel plates and separation between the plates, respectively, ε_r is the relative dielectric constant of the material between the plates, and ε_o is the vacuum permittivity.

$$C = \frac{\varepsilon_r \varepsilon_0 A}{d} \qquad \text{eq 2.1}$$

We incorporate a similar system in our experimental setup, where the cranium would assume the role of one of the conductive bodies and a copper plate placed proximal to the cranium would act as the second plate. As a result, the two form a capacitor and the capacitance can be measured. Since the capacitance is a function of the distance between the conductors, changes in the capacitance of the system can be used to determine the change in the distance and detect relative motion. Furthermore, by placing multiple, thin conductive plates around the cranium, we can produce multiple capacitors, and with strategic plate placement, 3D positional information can be acquired by constant monitoring of the capacitance. This paper provides a proof of concept for patient translation detection using this novel method.

It should be noted that conductivity is not a binary attribute. As such, conductors used in real-life capacitors have some inherent resistance. Similarly, dielectric materials can have some inherent electrical conductivity. These aspects of a capacitor are modeled as resistors [118,119], as shown in figure 2.1. A resistor in series with the capacitor depicts the resistivity of the capacitor plates and is often referred to as equivalent series resistance (ESR). Another resistor in parallel with the capacitor is referred to as the shunt resistance or insulation resistance (Rs) and accounts for the leakage through the dielectric material. An ideal capacitor would have an infinitely high Rs value to prevent any leakage of current to pass through the plates. For a functioning capacitor, the Rs value should be high to minimize the leakage. Our capacitor design goal includes physical clearance between the cranium and the conductor plate (filled with air) with a

conductivity in the range of 3×10^{-15} S/m to 8×10^{-15} S/m [120] so leakage effects become negligible. Considering the case where both plates of the capacitor are made of a material such as copper with conductivity of 5.96×10^{7} S/m [121], the ESR can be approximated to zero. For proximity detection of a human, we can replace one of the copper plates with a human cranium to depict our experimental conditions. Cerebral spinal fluid (CSF), which is a major source of cranial conductivity, has a conductivity of 1.79 S/m [99] . This non-ideal conductor can be modeled in conjunction with a non-zero ESR value. As stated previously, the capacitance, by definition, does not depend on the level of conductivity of the plates. Adding an ESR produces a drop in the applied voltage to the capacitor and resulting in a lower stored charge.

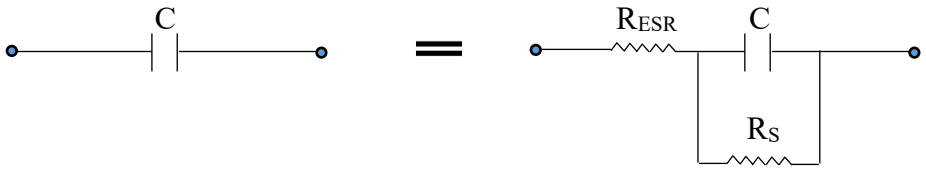

Figure 2.1 Equivalent circuit diagram of a non-ideal capacitor.

For initial testing of a single detector, a parallel plate arrangement was used to compare the performance of two different plate materials, copper and aluminized Mylar, as well as the dependence of response on thicknesses of the conductors. Experiments were performed using copper and aluminized Mylar plates of 0.127 mm thickness and varying plate areas of 3×3 cm^2, 4×4 cm^2, and 5×5 cm^2 to compare the performance of the two materials. Coaxial cable was soldered on the copper plates and glued on the aluminized Mylar plate using conductive silver paste. To investigate the effects of plate thickness on sensitivity, copper plates of 3×3 cm^2, 5×5 cm^2, and 10×10 cm^2 were used

with 0.0762 mm and 0.254 mm thickness. For these experiments, one plate was fixed in position and the second plate was moved using a H-820 6-Axis hexapod stage (Physik Instrumente (PI) GmbH & Co. KG, Auburn, Massachusetts, USA) while the capacitance was being monitored. The Hexapod can perform translation motion in steps as small as 10 μm with a reproducibility of ± 2 μm for horizontal motion and ± 1 μm for vertical motion. A capacitive touch sensing integrated circuit (MPR 121, Adafruit Industries, NYC, NY & Freescale semiconductor, Austin, TX) was used for acquisition of capacitance measurements. The MPR 121 measures the capacitance by applying a constant DC current to the copper plate. The resulting voltage is sampled at the end of each charge cycle and reported as a 10-bit ADC value. This value is inversely proportional to the capacitance. An I2C interface device (NI USB-8452, National Instruments, Austin, TX) was used to control the acquisition process through a Matlab interface developed in-house.

2.4.1.1 Capacitive Array Design

An array containing four conductive plates was designed to detect patient translation in three-dimensions. The array consisted of a superior plate positioned at the cranial vertex, two lateral plates positioned in front of the ears, and an anterior plate placed in front of the nose, as shown in figure 2.2. The conductive copper plates were 15.2 cm by 10.2 cm and mounted on acrylic backings. The relatively large plate sizes were chosen to increase the capacitive signal as per equation 2.1. Although the backings in this prototype would be highly attenuating for a therapeutic photon beam, the intention for future versions is to use, for example, thin carbon fibre as a substrate. The 0.0254 mm copper conductor used will attenuate a 6 MV photon beam by only approximately

0.095 %. A constraint in the design was to place the detectors at least 1 cm away from the surface of the mask to allow clearance for a range of cranial separations, however, compared to single-detector testing results, it was anticipated that the sensitivity would also depend on curvature of the cranium below the detector area.

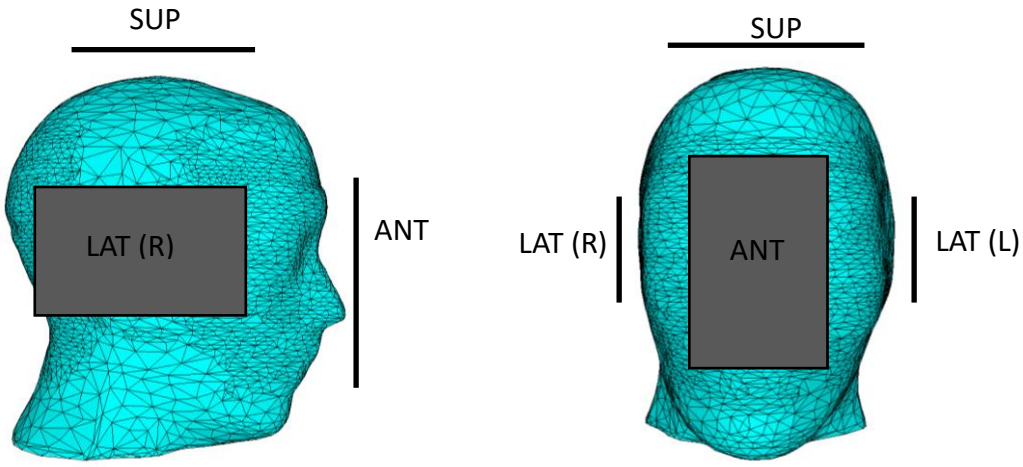

Figure 2.2 Diagram of the array sensor positions with respect to patient cranium. Superior, right, left, and anterior plates are marked as SUP, LAT (R), LAT (L), and ANT, respectively.

2.4.2 Array Calibration and Readout Using a Human Subject

The capacitive array was calibrated to provide translational information in millimeters based on detected changes in capacitive signal (ADC values). A volunteer was immobilized using an S-frame thermoplastic mask. To avoid moving the volunteer, the array was translated in three directions (lateral, superior, and anterior) relative to the cranium in 1 mm steps to simulate patient motion, with all detectors translating in tandem. These data were acquired at 190 Hz and used to produce a calibration curve of capacitive signal versus relative cranium-plate position for each dimension of motion.

Subsequently, a predefined, arbitrary trajectory was applied to move the array relative to the subject, and the calibration curves were used to return motion in calibrated units.

A hypothesis of this work was that the detected signal is indeed arising from the cranium and not from the thermoplastic mask itself. To evaluate this, data were acquired with the setup shown in figure 2.3 in the presence of the thermoplastic mask and absence of the volunteer. The array was translated in 1 mm steps in three-dimensions in +X direction (superior plate moving away from the cranium), +Y (right lateral plate moving away from the cranium) and +Z (anterior plate moving away from the cranium). The array was translated five steps with a displacement of (1 mm, 1 mm, 1 mm) per step and data were acquired for three seconds at each step. The same experiment was conducted when the mask was moved out of proximity of the array.

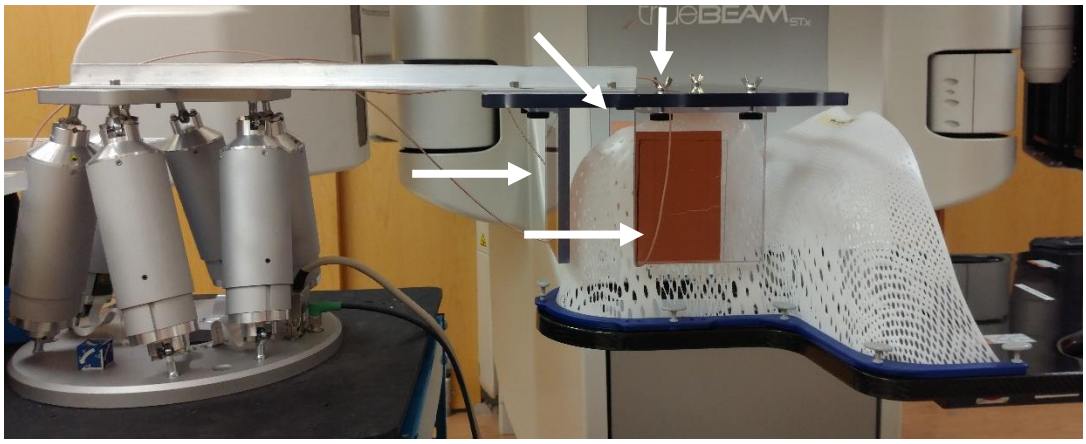

Figure 2.3 Experimental setup in the linac environment. The detector array is placed around the thermoplastic mask. The hexapod stage on the left is used to simulate motion by translating the array. The white arrows point to the copper plates in the picture.

2.4.3 System Stability in Linac Environment and in the Presence of Ionizing Radiation

In order to determine the feasibility of capacitive monitoring in linac room conditions, the capacitive array was used to investigate any potential signal interference. Data were gathered for 90 s without radiation. Subsequently, the array was irradiated for 90 seconds at a dose rate of 1400 MU/minute with a 6 MV flattening filter free (6X-FFF) beam from a TrueBeam STx linear accelerator (Varian Medical Systems, Inc., Palo Alto, CA). The array was centered in the field and all four detectors were within the primary radiation field. Data were collected from all four plates in the absence and in the presence of radiation. The acquired data were reviewed at times corresponding to beam on/off to assess for possible transients, e.g., due to EM interference.

2.5 RESULTS

2.5.1 Detector Design

Two different plate materials (copper and aluminized Mylar) were investigated in a parallel plate setup as potential detectors. As shown in figure 2.4, the copper plates offer higher sensitivity (change in capacitive signal per millimeter change in plate separation) compared to Mylar plates of the same length and width. Therefore, copper was chosen as the detector material. As shown in figure 2.4, thinner plates offer higher sensitivity at small plate distances, and overall, larger plates offer higher sensitivity. However, using larger plates can lead to higher sensitivity at larger distances, as shown in figure 2.4. For example, the 10×10 cm^2 copper plate displays sensitivity of 8 ADC counts/mm motion at 18 mm of plate separation. Based on these results, a thin copper foil with 0.0254 mm thickness with 0.0406 mm thick conductive adhesive backing was chosen as the detector.

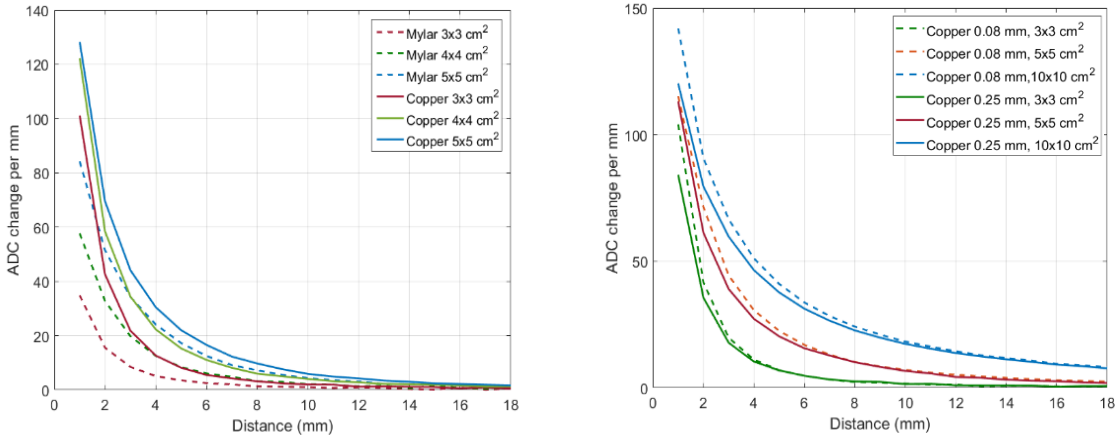

Figure 2.4 Sensitivity comparison between different sizes of Mylar and copper conductive plates (left), and sensitivity comparison between different thicknesses of copper conductive plates (right).

2.5.2 Array Calibration and Readout Using a Human Subject

Figure 2.5 below shows the ADC signal as a function of translation in different directions. As shown in figure 2.5, change in ADC signal is observed for plates in the respective direction of motion. This change in signal corresponds to the respective direction of motion for lateral and superior plates. However, this effect is not as prominent in the anterior direction with the change in signal resulting from the motion spanning 7 ADC counts per 5 mm of motion. This can be explained by the fact that although the distance of the anterior detector from the most proximal aspect of the patient surface was comparable to the other detectors, the surface curved away from this detector, resulting in a much larger average distance and thus lower sensitivity. The lateral and superior signal shown in figure 2.5 were used for calibrating their respective detectors using a second order polynomial functions (R^2 =1). Equation 2.2 shows the calibration function for the superior plate, where y_{sup} depicts the position in millimeters

and x_{sup} is the ADC signal from the superior plate. Similarly, equation 2.3 shows the calibration function for the lateral direction, where y_{lat} shows the position of right lateral plate and x_{lat} is the differential signal received from the two lateral plates.

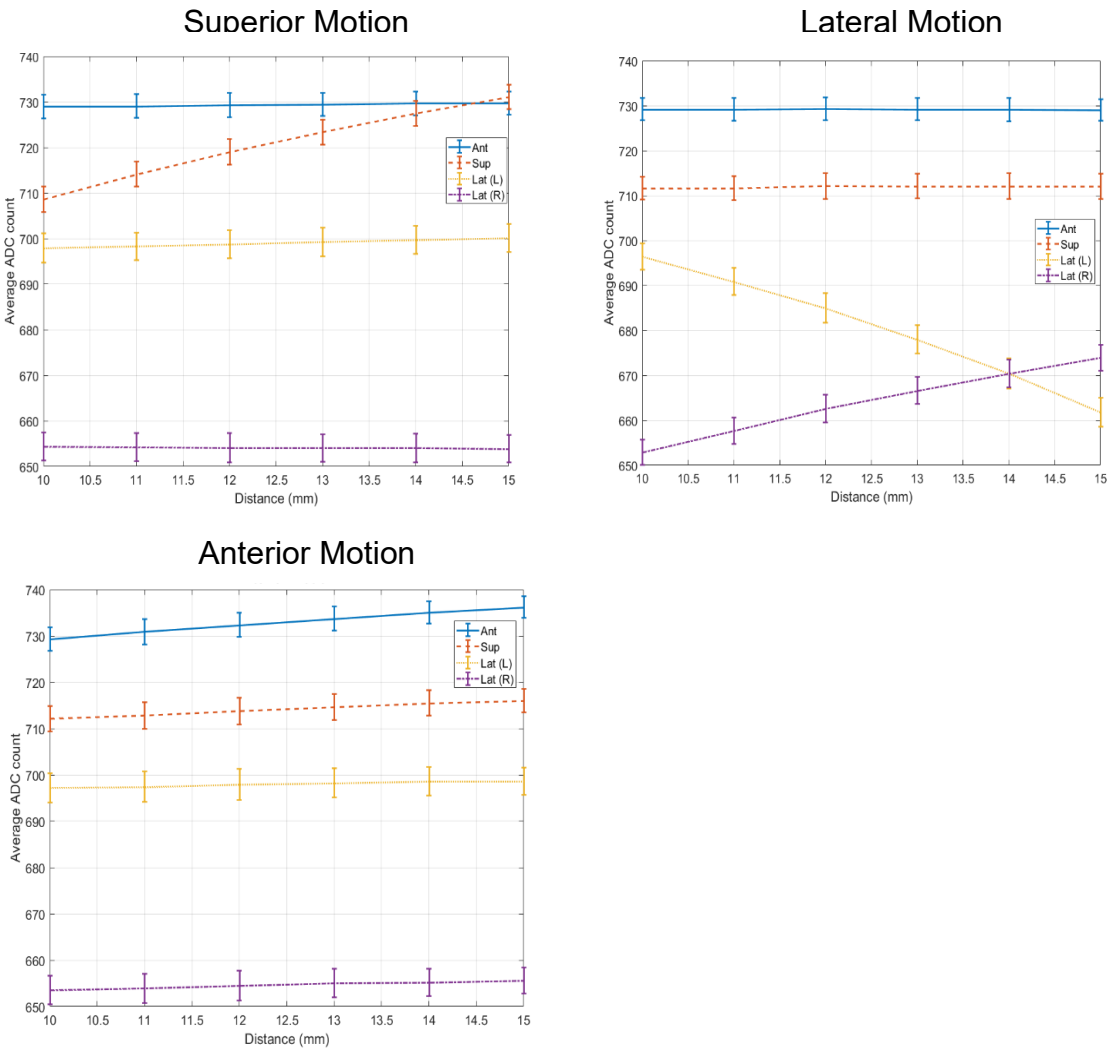

Figure 2.5 Plots showing the ADC signal at different cranial distances. Direction-specific change in signal is observed that corresponds to the respective direction of motion. The error bars depict two standard deviations.

$$y_{sup} = 0.002548\, x_{sup}^2 - 3.446\, x_{sup} + 1172 \qquad \text{eq 2.2}$$

$$y_{lat} = -0.0001411\, x_{lat}^2 - 0.08547\, x_{lat} + 13.99 \qquad \text{eq 2.3}$$

Data were acquired by translating the mask system in the absence of the volunteer to verify that the cranium was the source of the signal. Data were averaged over three seconds at each position with a readout frequency of approximately 190 Hz. The results shown in figure 2.6 illustrate the signal in the absence of the volunteer with and without the thermoplastic mask placed in between the detector plates. Our results illustrate that the change in signal (depicted by the slope of the lines in figure 2.6) show a similar trend in the absence and presence of the mask. This underlines a desirable feature of the capacitive detection approach, i.e., the system should be sensitive to the cranium inside the mask, and not the mask itself.

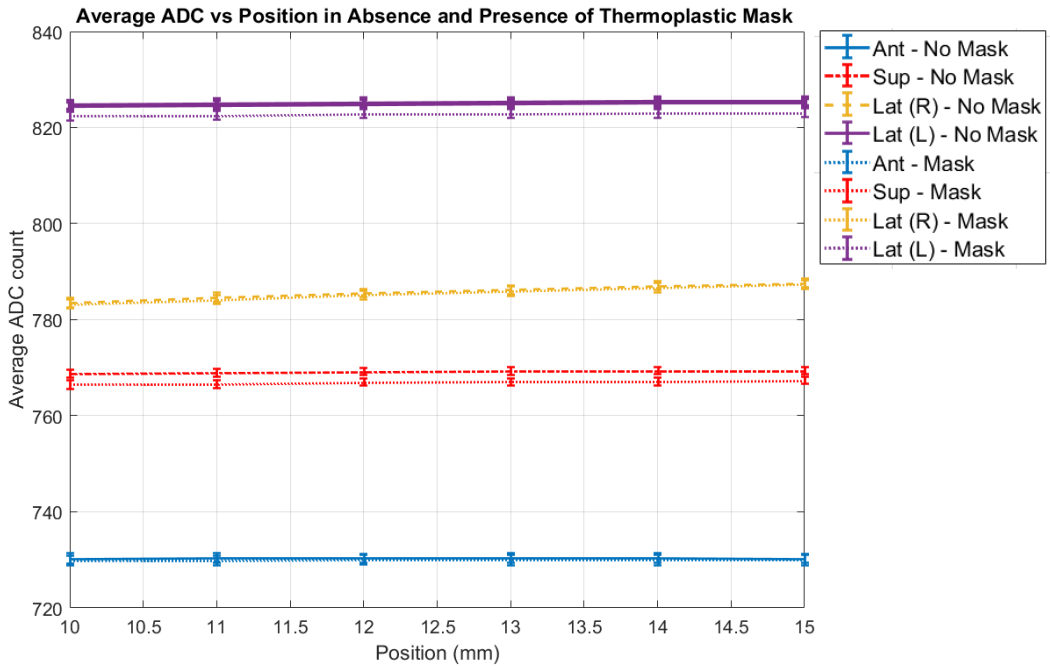

Figure 2.6 Capacitive signal collected in the absence of the volunteer, in the presence and absence of the thermoplastic mask.

During the first phase of performance testing, superior and lateral motion detection was tested since their respective calibration curves showed promising sensitivity. In order to test the performance of the array in these two directions, predetermined translations were introduced in lateral and superior directions and the calibration curves were applied to detected capacitive signal to return the direction and magnitude of the motion in millimeters. The known motion included two steps in the superior direction and two steps in the lateral direction. The plates were originally positioned at 10 mm distance from the patient. They were then moved to 10.5 mm and 11 mm distance for both superior and right lateral detector plates. Data were averaged for three seconds at each position at approximately 190 Hz. The data were averaged using a running average of eighteen data points where the value of each data point n is substituted with the resulting average of data points n to n+17. This helps reduce random noise in the data and increase the average SNR value over all four channels from 256 ± 35 to 1909 ± 261 (mean ± stdev). The results are shown in figure 2.7. Respective calibration equations were used to convert the capacitive signal to position information. Reference lines were added to indicate the average detected position at each step. As illustrated in figure 2.7, the system detected the two occurrences of motion in both superior and lateral directions. The detected steps were 0.5 mm and 0.4 mm for the first and second motion, respectively, which compares well to the actual introduced motion of 0.5 mm. Additionally, absolute patient position was detected in terms of distance from the capacitive plate. The detected positions in the lateral direction show a minimum and maximum disparity of 0 mm and 0.1 mm compared to the actual position data. In the superior direction, however, the absolute positional information shows a minimum and maximum disparity of 0.6 mm and

0.7 mm, respectively, compared to the known positional information. Nonetheless, the goal of our design was to detect relative motion and the system was able to easily detect 0.5 mm steps of motion using a calibration curve that was obtained with 1 mm step size with an accuracy of 0.1 mm.

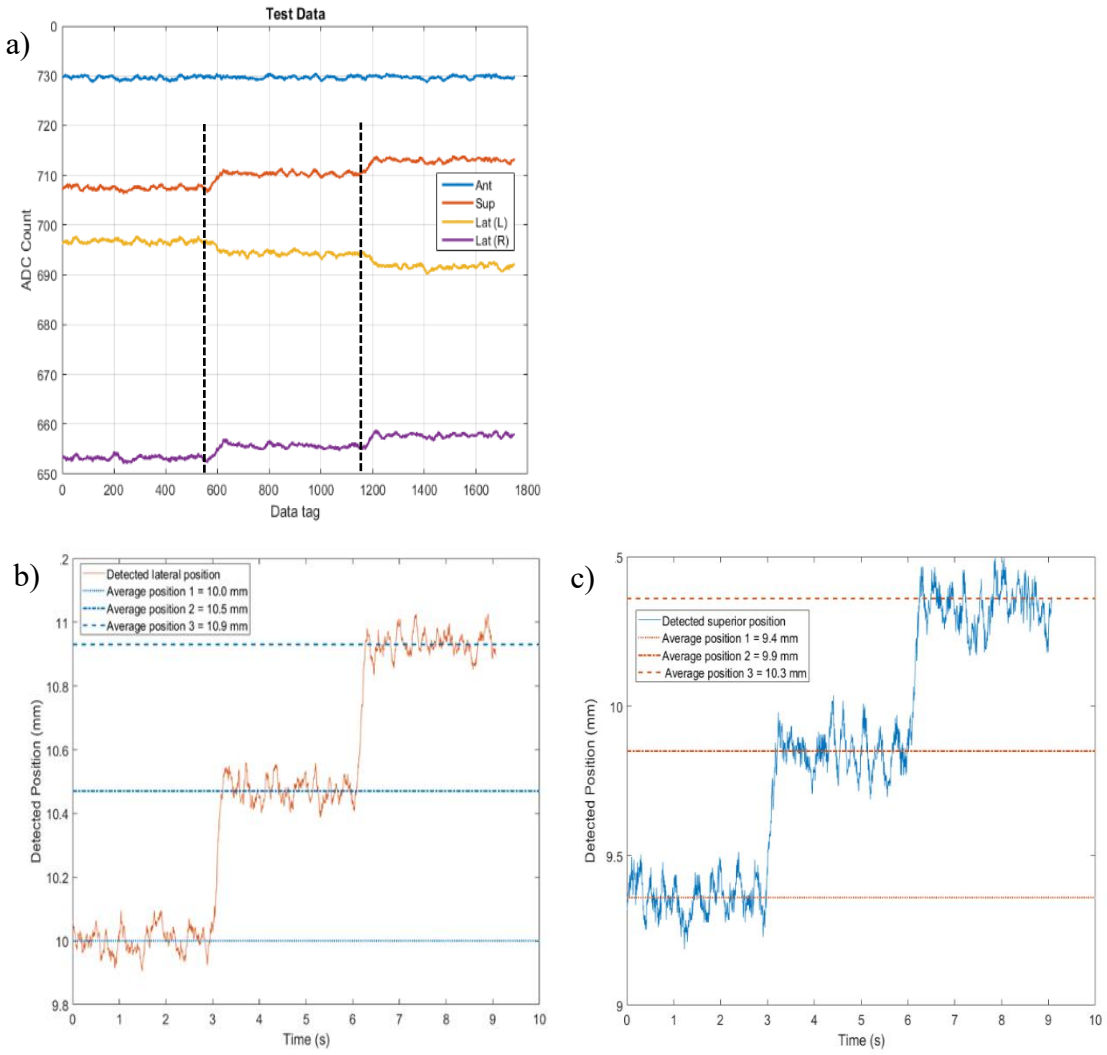

Figure 2.7 (a) Signal resulting from controlled motion, introducing 0.5 mm translations in the superior and lateral dimensions. Vertical lines indicate time points of introducing translations. (b) Detected lateral motion. Horizontal lines depict the average detected position. Motion is detected with 0.1 mm accuracy for 0.5 mm steps. (c) Detected superior motion. Horizontal lines depict the average detected position. Motion is detected with 0.1 mm accuracy for 0.5 mm steps.

2.5.2.1 Anterior-Posterior Motion

As illustrated in figure 2.5, the sensitivity (change in ADC counts per mm of motion) in the anterior-posterior direction was not sufficient to detect sub-millimeter motion when the detector is located 10 mm to 15 mm away from the thermoplastic mask. This prompted us to investigate the possibility of increasing sensitivity by placing the anterior plate closer to the cranium, thus reducing the average cranium-detector plate distance. To investigate this option, data were collected from an array with the help of a volunteer where the anterior plate was mounted at 0 cm from the closest point of contact with the mask (i.e. touching the mask) while the other plates were at 1 cm distance from the mask. The array was retracted from the mask in 1 mm increments. The resulting change in capacitive signal is shown in figure 2.8. Based on the observed sensitivity (i.e., the slope of the plot between consecutive data points) sensitivity declines at larger distances. Therefore, the anterior plate was mounted at 5 mm distance from the mask to avoid contact with the mask during the experiments while still providing sufficient sensitivity. Known motion was introduced to test the detection system and a second order polynomial calibration curve for the range of 5 mm to 10 mm was applied to the signal and the detected motion is illustrated in figure 2.8. Equation 2.4 shows the calibration equation, where y_{ant} depicts the position in millimeters and x_{ant} is the ADC signal from the anterior plate. As shown in figure 2.8, it is evident that, for this arrangement, the anterior plate is capable of detecting 0.5 mm steps with 0.1 mm accuracy.

$$y_{ant} = 0.003177\, x_{ant}^2 - 4.096\, x_{ant} + 1321 \qquad \text{eq 2.4}$$

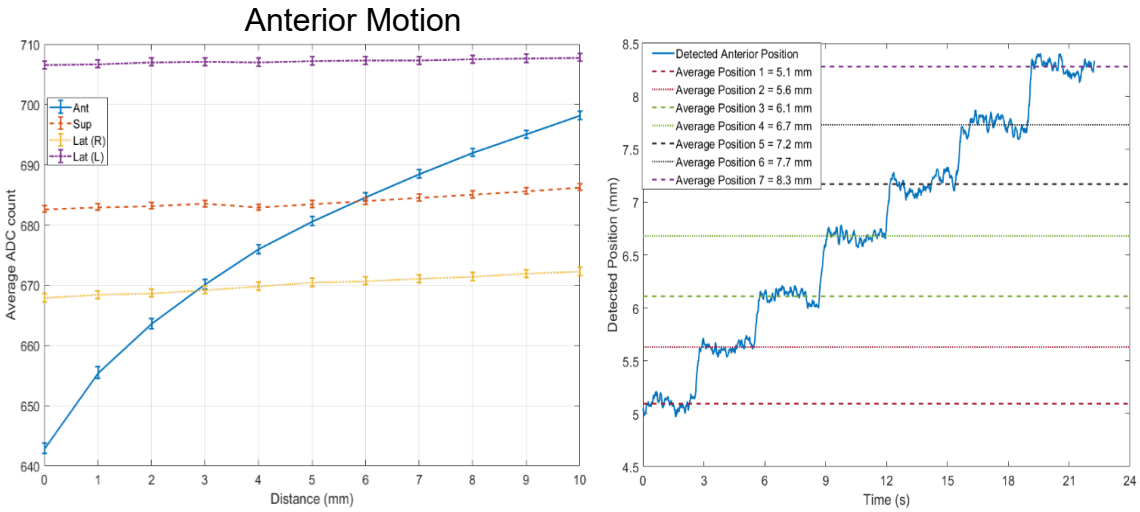

Figure 2.8 Signal from the anterior sensor plate at different distances from the mask (left). Detected motion for anterior plate mounted at 5 mm distance from the mask with lines showing the average detected position in each step (right).

2.5.3 System Stability in Linac Environment and in the Presence of Ionizing Radiation

A histogram of the capacitive signal collected from each plate in the capacitive array in the presence and absence of radiation beam is shown in Figure 2.9. The data clearly show that radiation has no effect on the capacitive signal values (shown in the form of ADC count) as a student's t-test performed on the data showed no significant difference between the two sample sets ($p < 0.001$). Table 2.1 provides additional information regarding the behavior of the system in the radiation field. The data presented show that radiation does not affect the mean capacitance signal or the standard deviation. The SNR, defined as mean signal divided by the standard deviation, is high (range 930 to 1555) in all cases.

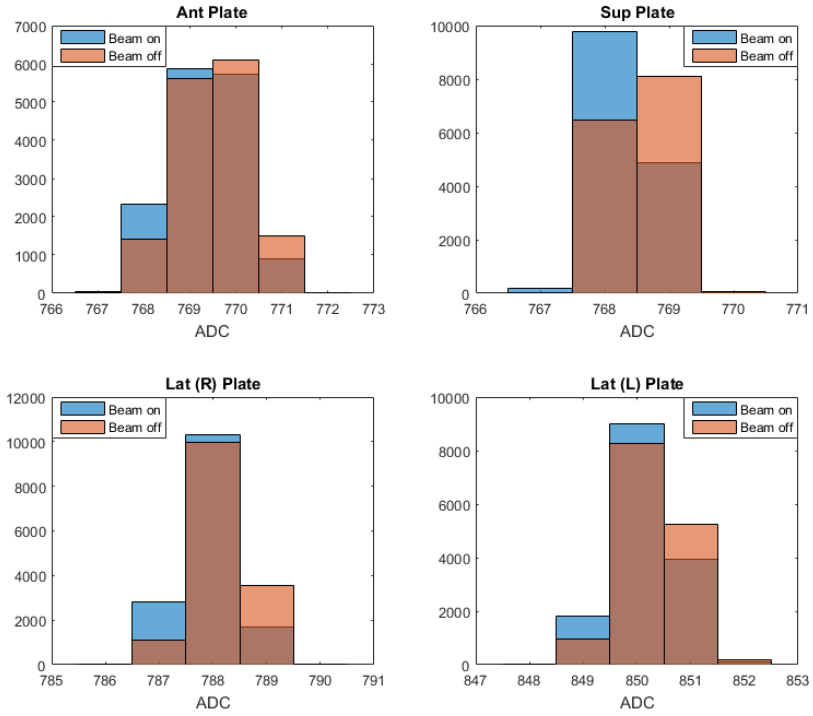

Figure 2.9 Histogram of signal in linac room conditions. Comparison of capacitive array signal in the radiation field under beam on (blue) and beam off (orange) conditions. Brown regions depict overlap of the two data sets.

Table 2.1 Signal Stability in linac room conditions. Comparison of capacitive array signal in the radiation field under beam-on and beam-off conditions. Student's t-test showed no significant difference between the data acquired under beam-on and beam-off conditions ($p < 0.001$). SNR is defined as mean signal divided by the standard deviation.

	Anterior Plate		**Superior Plate**		**Lateral Plate (Right)**		**Lateral Plate (Left)**	
Beam	*ON*	*OFF*	*ON*	*OFF*	*ON*	*OFF*	*ON*	*OFF*
Stdev	0.8	0.8	0.5	0.5	0.6	0.5	0.6	0.6
Mean	769.4	769.5	768.3	768.6	787.9	788.2	850.2	850.3
SNR	933.2	950.5	1554.7	1509.1	1425.9	1449.9	1357.1	1386.7

2.6 DISCUSSION

The purpose of this investigation was to develop a first prototype for continuous monitoring of patient motion during stereotactic radiosurgery. The current design of the system shows high signal stability in the linac environment and inside the radiation field. The array has the capability to detect 3D translations with sub-millimeter accuracy. This near real time (~190 Hz) monitoring device is not sensitive to the position of the mask and responds to the position of the cranium. As a result, the system does not require any modification to the thermoplastic mask. This provides an advantage in comparison to optical systems that require a removal of sections of the immobilizing mask to determine patient motion. This technology can detect sub-millimeter motion with 0.1 mm accuracy, which can be compared to the reported residual error of 3-0.3 mm observed when using optical systems depending on the fields of view with 0.3 mm root mean square error achieved when field of view is larger than 1000 vertex points [114]. Also, with comparison to either optical surface imaging or stereoscopic x-ray systems, this approach is compact, modular and does not require significant additions to the treatment room, e.g., mounting of cameras.

We see the role of this system as complementing existing image guidance systems, such as ExacTrac [70,71,113] and cone beam computed tomography (CBCT) [122–124], whereby initial setup could be done under image guidance to set a baseline position from which real-time motion would be detected. While this work has presented some results indicating absolute positioning of the subject with the array, achieving this in a robust manner would be more complex since the system would have to be registered to room coordinates. This could be done, for example, by attaching optical reflectors to the frame

to which the detector plates are attached. However, this would increase the cost and complexity of the overall system. Currently, the symmetry of lateral plates allows for better absolute position detection, but this feature is not available in other directions, leading to higher discrepancy in determining absolute positions. With regard to detecting relative motion, we have shown that our system is capable of detecting 0.5 mm translations. This was deemed a practical limit since AAPM practice guidelines [125] recommend 1 mm minimum positioning/repositioning accuracy for SRS treatments, and the CBCT repositioning error [126] is shown to be $\geq$ 0.5 mm and typical CBCT head scan protocols yield a voxel size on the order of 0.5 mm [127]. As such, the capacitive system provides motion detection accuracy that is comparable to CBCT image guidance. Higher motion thresholds can be set depending on planning parameters, treatment indications, and PTV margins on a case-by-case basis.

The design of the system is prototypical, for example, in that the copper conductors were adhered to highly attenuating acrylic backings. This was done for ease of construction at this state, but the intention is to couple these to highly radio-transmissive carbon fibre in a frame, similar to the frameless radiosurgery positioning array [128] from Brainlab (Brainlab AG, Munich, Germany). Although the plate areas were quite large in the present prototype, they can be integrated into a frame that will make them unobtrusive relative to current hardware.

While the capacitive array shows promise with regard to sensitive detection of cranial motion, it can be improved in several respects. A prospective design constraint of this first prototype was to leave 1 cm clearance between the mask and the patient surface. While this constraint can be met for lateral and posterior/anterior motion, it does not

provide effective sensitivity for anterior motion. While the results demonstrate that one method of remedying would be to simply place the detector plate closer to the patient, a less intrusive approach may be to also include a posterior detector plate. This detector plate could be placed immediately below a standard hollow headrest and thus could be close to the patient's posterior surface. In this case it may be possible to remove the anterior detector plate entirely (thus clearing the view for the patient), or the anterior detector plate could be maintained to give robust detection of anterior-posterior motion, similar to the lateral detector plates in the current prototype.

With regard to the design of the single detector plate element, figure 2.4 shows adequate sensitivity. However, as for any capacitive system, the sensitivity declines with distance. The copper conductors facilitate a simple design, but likely there exist methods to increase the sensitivity that could allow reduction of detector plate area or increase of distance from the patient, or both. For example, materials with extremely high dielectric constants, such as copper calcium titanate (CCTO) [129], could be used as a layer on the detector plate, thus forming a "super-capacitive" detector plate. However, any design would have to maintain sufficient radio-transmissive properties for the photon beam qualities anticipated. Further work to explore this area is underway. Finally, the goal of this first iteration prototype was detection of translations only, which would provide functionality similar to existing real-time tracking systems, such as Calypso [130,131], for example. Future work will include enhancement and modification of the array to detect patient rotations.

2.7 CONCLUSION

This work serves as proof of concept for a novel, non-ionizing, continuous detector array that can be used to detect intrafraction patient motion. The current prototype can detect 0.5 mm motion with 0.1 mm accuracy in three-dimensions. The system can operate at frequencies as high as 190 Hz, providing near real-time positional data. The system is insensitive to the thermoplastic mask and detects only the cranium within, therefore, no modifications to the thermoplastic mask are required. Future work is focused on cranial rotation detection, alternative calibration methods, and increasing system sensitivity to a point where the sensors can be placed further away from the cranium without any loss in detection.

CHAPTER 3 FINITE ELEMENT ANALYSIS OF A CAPACITIVE ARRAY FOR 6D MOTION DETECTION DURING STEREOTACTIC RADIOSURGERY

3.1 PREAMBLE

Following the proof-of-concept established in manuscript 1 (Chapter 2), this manuscript aims to identify a more optimal array geometry. The following manuscript is focused on the comparison of different capacitive array designs to identify an array geometry capable of detecting intrafraction cranial rotation and translation motion. A Finite Element Analysis (FEA) model was devised and different capacitive array designs were modelled. Cranial rotations and translations were simulated using the cranial FEA model, and changes in capacitance between the capacitive array elements (sensor plates) and the model cranium were used to determine array sensitivity to motion. The cranial FEA model was validated using experimental data acquired with the help of volunteers. The manuscript introduces a method to compare sensitivities between different designs to determine a capacitive array design capable of 6D cranial motion detection.

The following chapter only differs from the below manuscript in the addition of revisions to improve clarity. Publication: P. Sadeghi, and J. L. Robar. "Finite Element Analysis of a capacitive array design for 6D intrafraction motion detection during stereotactic radiosurgery." *(Accepted)*.

3.2 ABSTRACT

This work presents a non-contact, non-ionizing solution for the continuous detection and characterization of intrafraction cranial motion with six motion dimensions. This capacitive monitoring system is a modular tool capable of detecting the cranial position through a thermoplastic mask without the use of skin as a surrogate. The purpose of this investigation is to develop an array of capacitive monitoring sensor plates capable of detecting translational and rotational cranial motion during radiotherapy.

This study compares the performance of different capacitive monitoring array designs for their potential to detect intrafraction cranial translations and rotations. To this end, a Finite Element Analysis (FEA) model of the human cranium was used to calculate the system capacitance while simulating translational (superior-inferior, left-right, anterior-posterior) and rotational (roll, pitch, yaw) cranial motion. The model was validated by comparing simulation results against experimental results acquired with the help of human volunteers. The verified FEA model was then used to compare multiple potential array designs. The arrays' sensitivities to translational and rotational motion and uniqueness of response were compared to determine the most promising design for six-dimensional motion detection. The most promising array design was chosen for a clinical volunteer study.

3.3 INTRODUCTION

Hypofractionated high precision radiotherapy techniques, such as stereotactic radiosurgery (SRS) and stereotactic radiation therapy (SRT), require patient motion management and high-accuracy positioning [57,64,111]. A combination of relocatable

thermoplastic mask systems and intrafraction motion monitoring techniques is recommended to achieve target accuracy and precision [4].

Commercially available motion monitoring systems often employ stereoscopic x-ray or optical surface monitoring techniques. Stereoscopic x-ray imaging systems provide a snapshot of the patient position using ionizing radiation [71,113]. On the other hand, optical surface monitoring techniques [72,114–116] offer continuous motion monitoring without the use of ionizing radiation by using the skin as a surrogate for cranial motion. The use of optical methods require less restrictive, open-faced thermoplastic immobilization devices, but using a deformable surrogate such as skin could lead to false positive and false negative results [72,73].

A novel, non-contact, capacitive monitoring technique was recently introduced to provide continuous intrafraction motion monitoring information [132–134]. In a simple case of a parallel plate capacitor, the system capacitance follows equation 3.1, where A and d denote the area of the parallel plates and separation between the plates, respectively, ε_r is the relative dielectric constant of the material between the plates, and ε_o is the vacuum permittivity.

$$C = \varepsilon_r \varepsilon_o \, {}^{A}/_{d} \qquad \text{eq 3.1}$$

To monitor motion with capacitance, one leverages the conductive properties of the human body: the cranium assumes the role of one of the conductive bodies, and a conductive sensor plate placed proximal to the cranium serves as the second plate. As a result, the two components form a capacitor. As shown in equation 3.1, system

capacitance is a function of distance between the conductors, and any changes in the capacitance of the system can be used to detect and determine the relative motion.

The electrical properties of human tissue have been studied extensively [88,97,99,135]. Since the conductivity of human body is primarily due to the electrolyte content, tissues with higher electrolyte content show higher conductivity [105] . In the context of this research, we primarily focus on electrical properties of different parts of the cranium. In this context, bone is reported to have high electrical resistance in a DC field [97]. The conductivity values can vary based on the sample [100], but are in the range of 10^{-3} to 4.5×10^{-3} S/m [97]. Skin also exhibits low conductivity with values around 10^{-5} S/m at low frequencies [88] and can be considered an insulator [102]. In contrast, other elements show high conductivity, for example, cerebral spinal fluid has 1.79 S/m conductivity [99], grey matter 1.03 S/m [135], white matter and brainstem 0.47 S/m [135], and cerebellum 0.89 S/m [135]. Thus for biomedical modelling of the cranium, the skin and bone can be modelled as insulating layers enclosing a conductive core (brain) or as a layered volume with different brain tissues incorporated into the model [103,104]. The relative dielectric constant values for bone [135] and skin [88] are reported as 14.9 to 22.1 and 10^4 to 10^6, respectively. The muscle tissue also possesses a conductivity of 0.2 S/m to 0.3 S/m [95].

Our previous report outlined the capabilities of the capacitive monitoring method in detecting translational motion in three-dimensions through the thermoplastic mask [132]. In order to design a system capable of detecting rotations as well as translations, a robust simulation tool was necessary to investigate the behavior of different sensor plate placements on the arrays' capabilities in six-dimensional motion detection. This is especially important in cranial motion detection because the reported patient cranial

intrafraction motion, while immobilized, is on the order of a few degrees of rotation and a few millimeters of translation [9]. Considering this, and that the capacitive monitoring system signal change is dependent on changes in cranium-sensor plate separation, initial characterization and ranking of different capacitor array designs is best suited to computer modelling. In this paper, we explore different options for detecting rotational and translational information with modified array designs. A Finite Element Analysis (FEA) model of a cranium is defined and verified with experimental data for a single array setup. This FEA model is then used to compare different array designs by comparing their simulated sensitivity (signal change per 1 mm or 1°of motion) for each motion, as well as the uniqueness of their response to each motion. We then compare the performance of multiple design options for six-dimensional cranial motion detection.

3.4 Materials and Methods

3.4.1 Array Designs

The proposed array designs leverage one or a combination of the following operation modes for capacitive proximity sensing [11]. An illustration depicting the different operation modes is provided in figure 3.1.

• Transmit mode: this mode operates via the coupling on the human body (i.e., cranium) with a sensor plate. The capacitance signal readout provides information regarding the distance between the cranium and the plates.

• Shunt mode: this mode works by introducing the grounded body part (i.e., cranium) into the electric field present between two conductive plates. The changes introduced into the electric field translate into changes in capacitance readout.

• Loading mode: this mode, replaces a conductive plate with a grounded body part (i.e., cranium) and therefore only requires a single conductive plate.

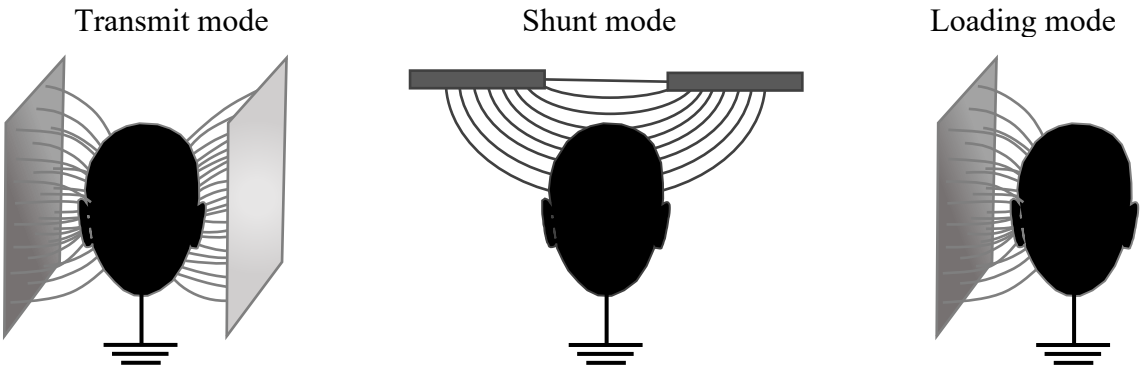

Figure 3.1 Different operation modes for capacitive proximity sensing.

Different array designs were devised with a combination of the above modes while following the design principles below:

• **Symmetry** – placing conductive sensor plates in a symmetric arrangement is advisable in array design [136], and this principal was followed where it was anatomically permissible.

• **Minimal obstruction** – in a simple case of parallel plate capacitor, as shown in equation 3.1, an increase in sensor plate size leads to an increase in capacitance. However, to assist with patient comfort, we aimed to provide a minimally intrusive design by reducing the obstruction of the patient's field of view through decreasing the size and number of the array components for a 6D prototype wherever possible.

Therefore, we tried to strike a balance between increasing the system sensitivity while minimizing the sensor plate obstruction in each array design.

• **Sensor plate placement** – all arrays were placed superior to the Temporal Mandibular Joint (TMJ) to reduce the possibility of false positive detection due to motion of the joint.

• **Sensor plate separation** – all quadrilateral sensor plates positioned in the same plane have a 4 cm interplate separation. The curved sensor plates have a minimum of 5 mm interplate separation. The interplate separation was implemented to reduce cross-talk between sensors while still ensuring that multiple plates can fit in the area around the cranium.

• **Number of plates/readout frequency** – the capacitive signals are read out serially in groups of four by the FDC-2214 capacitive proximity sensor (Texas Instruments Incorporated, Texas, USA). Therefore, the addition of plates could reduce the read-out frequency.

Figure 3.2 illustrates the four array designs chosen for this analysis. The first array, shown in figure 3.2 (a), is a symmetric ring design at the cranial vertex with four quarter sensor plates and is referred to as design I. The array has an inner diameter of 8 cm and an outer diameter of 16 cm. There is a 5 mm gap between the closest edges of neighboring sensor plates. This design uses the shunt mode for motion detection. A key motivation behind this array design is minimizing the use of facial features by placing the sensor plates away from the anterior and lateral aspects of the cranium to potentially reduce the patient-specific signal variations based on the muscle and fat components of the individuals. This

design is symmetrical along the anterior-posterior, and lateral directions and has the added advantage of not blocking the patient's view. Due to the limited available area around the cranium, the sensor plate sizes were chosen such that they would minimize crosstalk (by allowing room for interplate separation) and still possess a minimum area of 25 cm^2 per sensor.

Figure 3.2 (b) illustrates another design with four sensor plates (design II). Here, the rationale is to have sensor plates positioned along each motion axis. This guarantees a change in cranium-sensor distance during motion along each axis. To this end, two lateral plates of 5×5 cm^2 are placed symmetrically above the ears, a 10×10 cm^2 superior plate is placed at the cranial vertex, and an anterior plate of 5×10 cm^2 is placed anteriorly to the forehead.

Figure 3.2 (c) depicts design III with five sensor plates. This design contains the same lateral and anterior plates as design II. However, this design includes two superior sensor plates, 5×10 cm^2 each, positioned at the anterior and posterior aspects of the cranial vertex. Since the brain is not symmetrical in the anterior-posterior direction, the idea behind this design is that having two sensors monitoring the anterior and posterior capacitive signals could be helpful for rotation detection.

Design IV, shown in figure 3.2 (d), further expands this idea and includes two lateral plates on each side of the cranium that are 5×10 cm^2 each and 4 cm apart to help improve the rotation detection capabilities. The model also includes two superior plates similar to design III. However, since the superior plates were already positioned along the anterior-posterior axis of motion, the anterior plate was removed from this design.

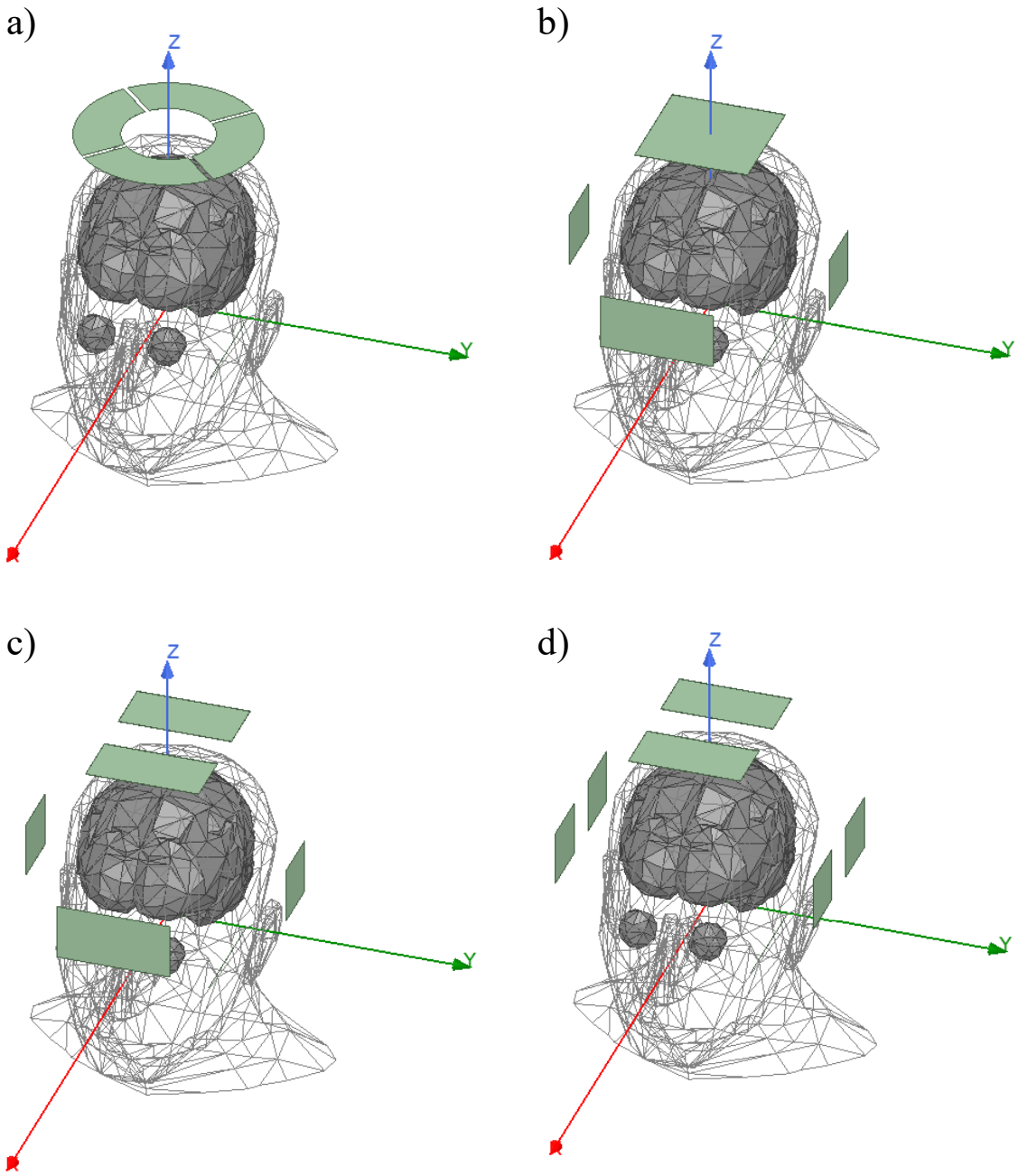

Figure 3.2 Four cranial array designs with four, five and six sensor plates.

All plates are placed 2 cm away from the cranial model. Where there are multiple sensor plates in the same plane, the whole plane is at 2 cm distance from the closest point of the cranium model to the plane. The 2 cm clearance was chosen to accommodate different cranium sizes without the need for patient specific adjustments on the prototype.

3.4.2 Finite Element Analysis (FEA)

Finite Element Analysis (FEA) is a numerical method used for solving partial differential equations by dividing the entire volume domain into a set of sub-sections referred to as finite elements. The neighboring finite elements are connected by sharing their nodes. Within each finite element, the solution is often approximated as a polynomial form of the neighboring nodes [137]. FEA can be used as a simulation tool to compare the performance of different array designs in the presence of human cranium [104,138]. In this paper, we use the Ansys Electronics software suite (ANSYS©, Pennsylvania, USA) for FEA simulations. The software starts by discretizing all the objects in the model into tetrahedral elements. These elements are referred to as the mesh. The aim is to solve Maxwell's equations in a finite region of space with specified boundaries or initial conditions.

The software solves for the unknown characteristic of the field, such as electric potential, inside each mesh element. Since the unknown characteristic for the field being calculated are represented as polynomials of second order inside each tetrahedral, regions with high spatial field variation require higher mesh density to provide the required solution accuracy. This is performed by the software and is referred to as adaptive mesh refinement.

In order to calculate the capacitance of the system, the solver first calculates the electric potential for each node using equation 3.2, where ε_r, ε_o, φ, and ρ_v, represent the relative permittivity, permittivity of vacuum, the electric potential, and volume density of the electric charge, respectively. There are ten nodes associated with each tetrahedral, and the electric potential inside each tetrahedral can be calculated using a quadratic approximation.

$$\nabla.(\varepsilon_r.\varepsilon_0\,\nabla\varphi) = -\rho_v \qquad \text{eq 3.2}$$

Once the electric potential is calculated, the electric field (E) is calculated using equation 3.3.

$$\vec{E} = -\nabla\varphi \qquad \text{eq 3.3}$$

After the solution for electric field is reached, the solver performs an error analysis, and if the stopping conditions are not satisfied in any of the tetrahedral, the mesh is refined and the electric field is recalculated. Once stopping criteria is satisfied, electric flux density (D) is calculated using equation 3.4.

$$\vec{D} = \varepsilon_r.\varepsilon_0.\vec{E} \qquad \text{eq 3.4}$$

Similarly, the energy stored in a static field (U) is derived using equation 3.5.

$$U = \int \vec{E}.\vec{D}\,dv \qquad \text{eq 3.5}$$

Determining the above-mentioned field characteristics, enables the solver to calculate additional system characteristics such as capacitance.

In this study, an FEA model was constructed using the Ansoft Human Body Model (ANSYS©, Pennsylvania, USA) and different arrangements of copper sensor plates. The average male cranium model consisted of conductive components including brain, cerebellum, eyes, and muscle tissue. Any volume of the model not occupied with organs (eyes, brain, cerebellum), face and neck muscle tissue, or bones were considered to have material properties somewhere between water and fat and were automatically assigned a relative dielectric constant of 50. The conductive array components were made of 0.025 mm thick copper to match the experimental conditions [132–134].

Simulations were conducted to calculate the capacitance between each component of the array and the conductive components of the cranium as a whole. Cranial motion was simulated by introducing translations in 1 mm steps, and capacitance was calculated at each step. Cranial rotations were simulated around the patient-specific rotational pivot point [139] in 1° steps. The first rotation axis was defined as the virtual line connecting through the ear canals. The second axis was perpendicular to the first, intersecting at the center of the first line and exiting through the cranial vertex. The third axis was defined to be perpendicular to both previously described axes and exiting towards the nasal septum. The three axes cross at the origin of the rotation [139]. This method of determining the rotational axes was chosen due to its clear definition of external landmarks in the absence of any other previously published data with subjects placed in a geometry similar to that used in this study.

3.4.2.1 Comparison of FEA Model to Experimental Prototype

Model validation was performed by comparing simulated and experimental data for array design I. This array offers the advantage of minimizing the use of facial features by placing the sensor plates away from the anterior and lateral aspects of the cranium. This can potentially reduce the patient-specific signal variations, thus making this array a desirable choice for comparing volunteer data with a design modelled after an average cranium. The simulated motions ranged from -3 mm to 3 mm and -3° to 3° around the neutral position in 1 mm and 1° increments. The same array design was fabricated in the lab using 0.025 mm think copper foil with 0.0406 mm thick conductive adhesive backing on 3D printed polylactic acid substrate. The capacitance was monitored using an FDC-2214 capacitive proximity sensor (Texas Instruments Incorporated, Texas, USA) at 20 Hz. The array was mounted on a H-820 6-Axis hexapod stage (Physik Instrumente (PI) GmbH & Co. KG, Auburn, Massachusetts, USA). Experiments were conducted in a linac environment with a volunteer fitted with an S-frame thermoplastic mask laying on the treatment couch, as shown in figure 3.3. The array was rotated and translated about the volunteer's cranium in 1° and 1 mm steps similar to the simulated conditions. Due to the limitations on the hexapod stage, data was acquired in the range of -2 mm to 2 mm for translations and -2° to 2° for rotations, except the pitch rotation where the data was acquired in the -1 to 1° range. Data were acquired for approximately five seconds in each position. The rotation axes were set using the anatomical landmarks as previously described. Three volunteers were used to acquire experimental datasets. The simulation data were normalized and plotted with an error bar equal to the simulation percent error (0.05 %) as specified by the simulation software. The experimental data were normalized

and plotted as average data in each state with an error bar equal to the standard deviation of the data acquired at each position for the experiments. A second degree polynomial fit was previously shown to represent the relationship between capacitive signal and motion [132]. Similarly, a second degree polynomial fit was performed on both simulation and experimental data to facilitate direct comparison. The normalized simulated and experimental results we used for comparison because the absolute values are provided in pF and ADC counts, respectively.

Figure 3.3 The experimental setup with the volunteer fitted with an S-frame thermoplastic mask. The capacitive array is positioned at the cranial vertex. The illustrated X, Y, and Z axes represent the lateral, superior-inferior, and anterior-posterior cranial motion, respectively.

3.4.2.2 Comparison of Array Designs

A favorable array design is required to have high sensitivity to motion. Sensitivity is defined as the change in array signal resulting from 1 mm of translation or 1° of rotation. In order to compare different array performances, it is necessary to perform a

direct sensitivity comparison between array designs with different number of sensor plates.

Equation 3.6 defines sensitivity for each dimension and step of motion, where S and X depict the sensitivity and capacitive signal readout, respectively. Subscripts i, j, and D specify the sensor plate, motion step, and dimension, respectively. Sensitivity could be a positive or a negative value depending on the increase or decrease in the signal. Average sensitivity for each sensor plate during a specific motion can then be calculated using equation 3.7, where N depicts the number of steps, which is six in the case of our simulations. Using equations 3.6 and 3.7 will provide a sensitivity value for each sensor plate. However, to calculate a sensitivity value for the whole array we need to combine the individual sensor plate sensitivities based on their response to the introduced motion.

$$S_{i,j,D} = X_{i,j+1,D} - X_{i,j,D} \quad , \quad j \in [-3, -2, 1, 0, 1, 2] \qquad \text{eq 3.6}$$

$$S_{i,D} = \left[\sum_{j=-3}^{2} \left(X_{i,j+1,D} - X_{i,j,D}\right) \right] / N \qquad \text{eq 3.7}$$

The comparison between different array designs was performed based on two metrics regardless of the number of active sensor plates in the design. A Spearman correlation was performed between the sensor plate capacitance values for each one of the six dimensional motions. For example, for superior-inferior motion, the simulated capacitance for each plate over the range of positions from -3 mm to 3 mm motion leads to seven separate capacitance values. For an array with four sensor plates, the Spearman

correlation between the plates would lead to a four-by-four correlation matrix. The matrix is symmetric and the main diagonal element are equal to one (self-correlation). A correlation matrix is calculated for each of the six motion dimensions. The matrix elements are in the range of -1 to 1 and rounded to the nearest integer or half integer value to distinguish maximum correlation difference between different array designs. A total of six correlation matrices are calculated for each array design, with each matrix corresponding to one of superior-inferior, left-right, anterior-posterior, yaw, roll, or pitch motion. These matrices are used to combine the sensor plate sensitivity values into array sensitivity. For each motion, the sensor plate with the highest average sensitivity, as defined by equation 3.7, is identified as the primary sensor plate. All sensor plates that are directly correlated (correlation value of 1) or anticorrelated (correlation value of -1) with the primary sensor plate are identified as the active plates and used to calculate the sensitivity for that motion, as shown in equation 3.8 below. For dimension D, S_D denotes the absolute value of the average sensitivity of the array, $S_{i,j,D}$ is defined in equation 3.6, $C_{i,P,D}$ is the correlation or anticorrelation value (1 or -1) between the primary plate (P) and the active plate (i), and A denotes the total number of active plates. This formula allows direct comparison of different array responses to each dimension of motion.

$$S_D = \left| \left[\sum_{i=1}^{A} \left(\sum_{j=-3}^{2} \left(C_{i,P,D} \times S_{i,j,D} \right) / N \right) \right] \right| \qquad \text{eq 3.8}$$

Aside from sensitivity, the array design's ability to distinguish between the different motion dimensions is an important factor for clinical use. The rounded matrices calculated for each array design are also used to determine the uniqueness of the array

response to each motion. In other words, an array which presents a unique matrix for each motion has a higher potential of successful motion classification for clinical use since the different sensor plates illustrate a unique response to each motion dimension. On the other hand, when the rounded correlation matrices for two or more of the six dimensions of motion are not differentiable, it is harder to predict whether simple classification of different motion dimensions would be possible based on the array response to motion.

3.5 RESULTS

3.5.1 Finite Element Analysis

3.5.1.1 Comparison of FEA Model to Experimental Prototype

Figure 3.4 shows simulated, and experimental data acquired during cranial translation using array design I as shown in figure 3.2 (a). The sensor plates are referred to by their position with respect to the cranium as anterior, left, right, and posterior plates. Figure 3.5 shows the simulated and experimental data acquired during cranial rotation using the above-mentioned array design. Since the simulation data had a wider motion range, the normalized data in figure 3.4 and figure 3.5 are cropped to match the range of experimental data to facilitate direct comparison. Sensor sensitivities (eq 3.7) for normalized experimental and simulated data show an average difference of 0.03 ± 0.07, 0.01 ± 0.03, and 0.08 ± 0.09 per millimeter motion for superior-inferior, left-right, and anterior-posterior motion, respectively, averaged over all three volunteers. Sensor sensitivities differences between normalized experimental and simulated data show an

average difference of 0.03 ± 0.07, 0.03 ± 0.1, and 0.1 ± 0.07 per degree for roll, pitch, and yaw, respectively, averaged over all three volunteers.

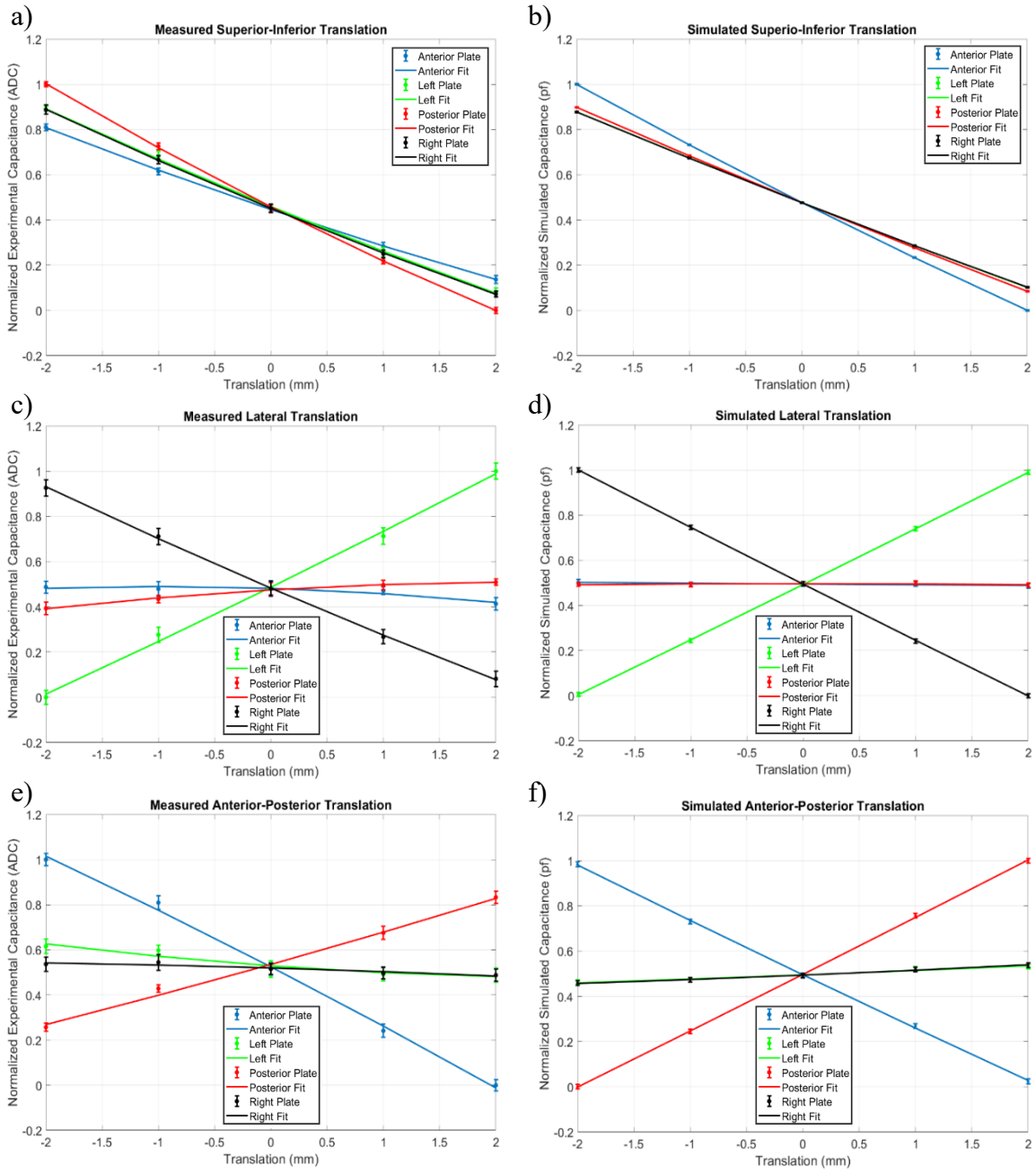

Figure 3.4 Normalized capacitive signal acquired during volunteer experiments of translation motion detection (a, c, e) and the corresponding normalized simulated capacitive signal using FEA modelling (b, d, f).

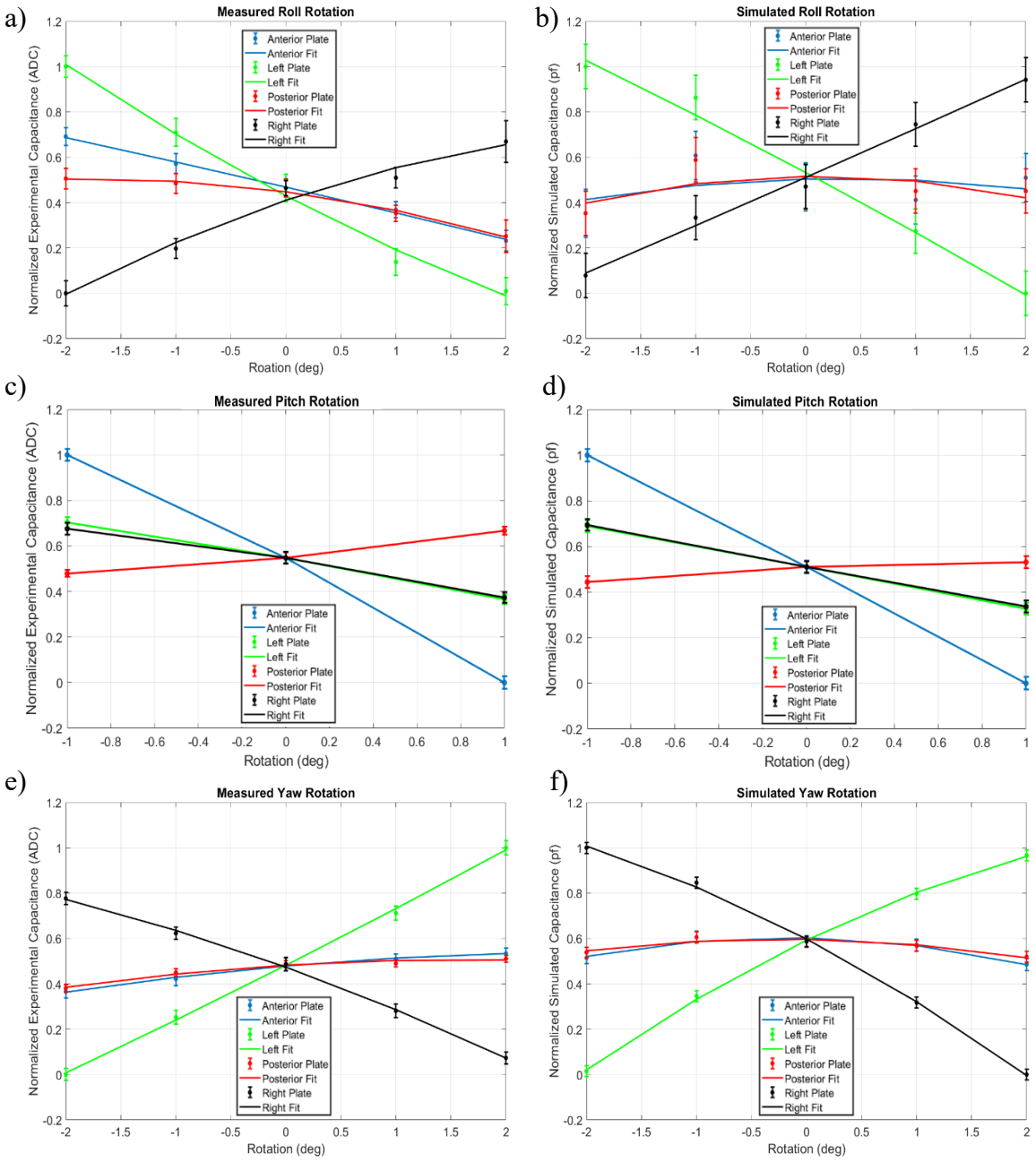

Figure 3.5 Normalized capacitive signal acquired during volunteer experiments of rotation detection (a, c, e) and the corresponding normalized simulated capacitive signal using FEA modelling (b, d, f).

3.5.1.2 Comparison of Array Designs

The average simulated sensitivity values for different array designs and motions are shown in table 3.1. The rounded Spearman correlation matrices associated with each design are illustrated in figure 3.6. The matrices are symmetric and the main diagonal elements are equal to one. The value of the unique elements of each matrix are depicted with colors.

Table 3.1 Simulated array sensitivity to translation and rotation. The underlined values specify the cases where the average sensitivity was lower than the associated error value.

	Translation sensitivity per millimeter (pF)			**Rotation sensitivity per degree (pF)**		
	SI	*Lat*	*AP*	*Roll*	*Pitch*	*Yaw*
Design I *	0.1570 ± 0.0003 **	0.0277 ± 0.0005	0.0266 ± 0.0004	0.0022 ± 0.0005	0.0178 ± 0.0004	0.0103 ± 0.0005
Design II	**0.1754 ± 0.0007** **	0.0635 ± 0.0006	0.0817 ± 0.0006	*0.0007 ± 0.0009*	**0.0517 ± 0.0007**	0.0492 ± 0.0006
Design III	0.1717 ± 0.0004 **	0.0643 ± 0.0006	**0.1127 ± 0.0005**	*0.0006 ± 0.0007*	0.0514 ± 0.0006	0.0501 ± 0.0006
Design IV	0.1610 ± 0.0004 **	**0.1090 ± 0.0004**	0.0562 ± 0.0004	**0.0180 ± 0.0004**	0.0351 ± 0.0004	**0.0885 ± 0.0004**

* Indicates unique rounded correlation matrices for all motion dimensions.
** Indicates the motion dimension with the highest associated sensitivity for each array design.
Bold indicates the highest overall sensitivity for each of the six motion dimensions.

The sensitivity value for roll rotation for designs II and III are lower than their associated errors. As a result, these two designs are not desirable for clinical use. Array design VI shows the highest sensitivity averaged over all six dimensions, however, its rounded correlation matrices associated with lateral translation and yaw rotation are equal (figure 3.6). This is a trend also observed in designs II and III. The only array design with

unique rounded correlated matrices for all motion dimensions is design I which also presents reasonable sensitivity (higher than the associated uncertainty) for all motion dimensions. This is the design using four sensors placed at the cranium vertex.

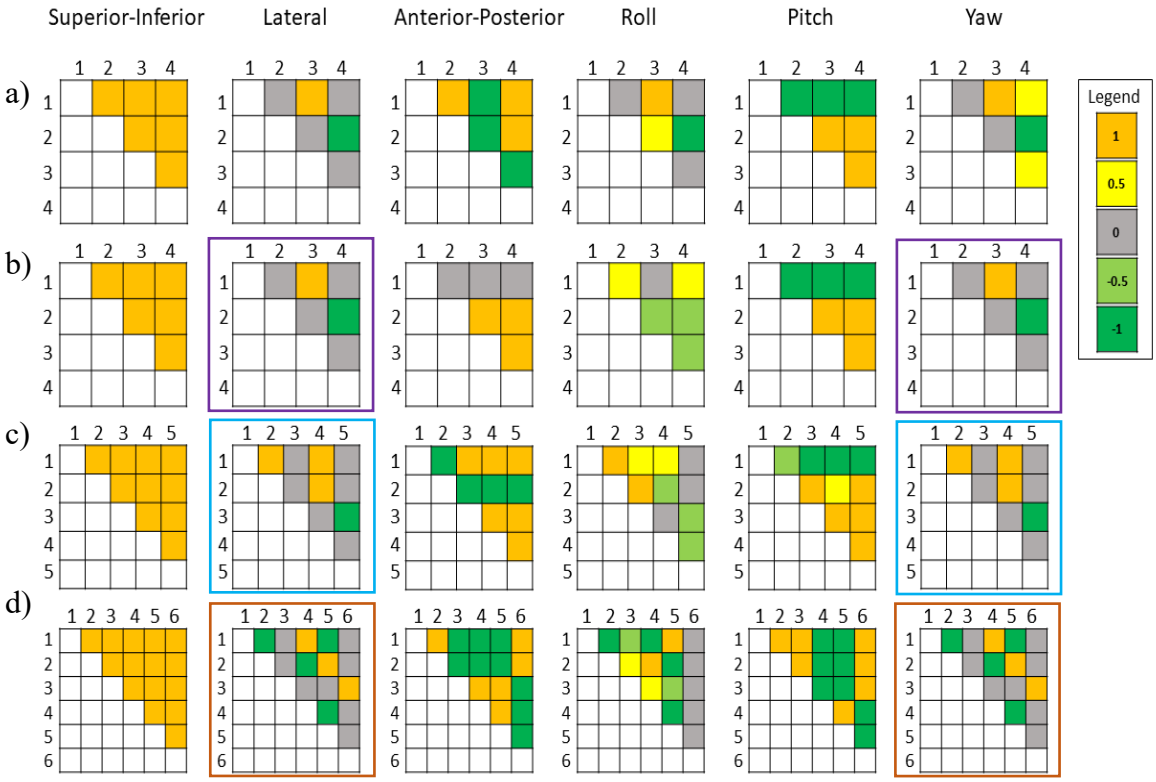

Figure 3.6 Rounded Spearman correlation matrices for (a) array design I, (b) array design II, (c) array design III, and (d) array design IV. The colored cells represent the unique elements of the matrix. The numbers on the rows and columns of each matrix correspond to the sensor plates of each array design. The diagrams encircled with lines of the same color exhibit the same correlation matrix for the specified motion dimensions.

3.6 DISCUSSION

The purpose of this investigation was to design and compare multiple prototypes for continuous six-dimensional monitoring of patient cranial motion using a finite element analysis, and volunteer data was used to validate the FEA model. The FEA cranium model is comprised of conductive components of the cranium (average brain, cerebellum, eyes, and muscle tissue) and includes the head and neck region. Finite element analysis provides a useful tool to determine the performance of each array design. However, multiple approximations are made in the design of the FEA model. The model does not include the linac body itself, the couch, the hexapod stage, or the electronic components of the CMS system. Additionally, the differences between the cranium size and shapes are not implemented in the FEA model. As a result of these approximations, we expect the simulations to exhibit similar trends to the volunteer data as opposed to an absolute match. Some of the volunteer motion data are illustrated in figures 3.4 and 3.5. Sensor sensitivities for normalized experimental and simulated data show an average difference of 0.03 ± 0.07, 0.01 ± 0.03, and 0.08 ± 0.09 per millimeter motion for superior-inferior, left-right, and anterior-posterior motion, respectively, averaged over all three volunteers. Sensor sensitivities differences between normalized experimental and simulated data show an average difference of 0.03 ± 0.07, 0.03 ± 0.1, and 0.1 ± 0.07 per degree for roll, pitch, and yaw, respectively, averaged over all three volunteers. These values could change depending on the shape and size of the volunteer cranium, and a volunteer study has been designed to look at the effects of cranial features on the system response. As a result, the study was focused on the comparative analysis of the simulated behavior of the different arrays designs.

All four designs presented in this study display maximum sensitivity during superior-inferior motion and minimum sensitivity during roll rotations. For array designs II and III, the roll sensitivity was lower than the associated error and as a result, these two designs were deemed deficient, leaving only design I and IV for consideration. While design IV presented the highest average sensitivity and the highest minimum sensitivity (roll), it also presents certain clinical challenges. First, the array includes six sensor plates, resulting in lower readout frequency (10 Hz) compared with design I with four sensor plates and consequently, a longer detection latency time in a clinical setting. A higher readout frequency is advantageous in reducing the latency in detecting motion and determining the new cranial position in a clinical setting. From figure 3.6 it is observed that with design IV lateral and yaw motions are not classified uniquely. Additionally, in design IV the sensors lateral to the patients' head will be close to features with large inter-patient variations. Design I also has the unique advantage of having all sensors placed away from patient-specific facial features/variations, which improves the probability of achieving similar array behavior for different individuals. It is because of these considerations that array design I was deemed the best candidate for a multi-volunteer clinical study.

3.7 CONCLUSION

This work presents a non-contact six-dimensional motion detection solution for intrafraction cranial motion management. This study also presents a cranial FEA model as a tool for simulation of different array designs for performance optimization. The FEA

model is verified against experimental data and allows for comparison of the sensitivity and uniqueness of response of different array designs.

CHAPTER 4 SIX-DIMENSIONAL INTRAFRACTION CRANIAL MOTION DETECTION USING A NOVEL CAPACITIVE MONITORING TECHNIQUE: EVALUATION WITH HUMAN SUBJECTS

4.1 PREAMBLE

Following the investigation into various capacitive arrays outlined in manuscript 2 (Chapter 3), the most promising capacitive array design is chosen for a volunteer study. The aim of the study was to investigate the performance of the system with a variety of cranial shapes and sizes. The study focuses on classification and calibration of translational and rotational cranial motion.

The following chapter only differs from the below manuscript in the addition of revisions to improve clarity. Publication: P. Sadeghi, D. Bastin-Decoste, and J. L. Robar. "Six-dimensional intrafraction cranial motion detection using a novel capacitive monitoring technique: evaluation with human subjects." *(Under review)*.

4.2 ABSTRACT

The purpose of this work is to introduce and evaluate a capacitive monitoring array capable of continuous 6D cranial motion detection during high precision radiotherapy. The ring-shaped capacitive array is comprised of four equally sized conductive sensors positioned at the cranial vertex. The system is modular, non-contact, and provides continuous motion information through the thermoplastic immobilization mask without relying on skin monitoring or use of ionizing radiation.

The array performance was evaluated through a volunteer study with a cohort of twenty-five individuals. The study was conducted in a linac suite and the volunteers were fitted with an S-frame thermoplastic mask. Each volunteer took part in one data acquisition session per day for three consecutive days. During the data acquisition, the conductive array was translated and rotated relative to their immobilized cranium in 1 mm and 1° steps to simulate cranial motion. Capacitive signals were collected at each position at a frequency of 20 Hz. The data from the first acquisition session was then used to train a classifier model and establish calibration equations. The classifier and calibration equations were then applied to data from the subsequent acquisition sessions to evaluate classifier and calibrator robustness.

The trained classifier had an average success rate of 92.6 % over the volunteer cohort. The average error associated with calibration had a mean value below 0.1 mm or 0.1° for all six motions. The capacitive array system provides a novel method to detect translational and rotational cranial motion through a thermoplastic mask.

4.3 Introduction

Relocatable thermoplastic mask systems are common for patient immobilization during SRS and SRT treatments to reduce inter- and intrafraction motion but do not eliminate it [7–9,59,60,112]. Therefore, combining the use of relocatable thermoplastic mask systems and intrafraction motion monitoring techniques is recommended for reducing dose to normal tissue and preventing a geometric miss [4].

Current practice for clinical motion monitoring includes the use of x-rays (stereoscopic x-ray imaging) or optical surface monitoring techniques. Both systems are

installed in a particular imaging or treatment room and provide three-dimensional motion information. While stereoscopic x-ray imaging systems use ionizing radiation to capture a snapshot of the patient position [71,113], optical surface monitoring techniques [72,114–116] have the advantage of providing continuous motion monitoring without the use of ionizing radiation. However, optical monitoring systems use the skin as a surrogate for cranial motion and require direct view of the skin by using less restrictive, open-faced thermoplastic masks. Using skin as a surrogate has been shown to lead to false positive and false negative results [72,73].

A capacitive motion monitoring technology has been recently developed to provide non-contact, continuous motion information [132–134] without the use of ionizing radiation. This technique employs capacitive sensors, which have the ability to sense the cranial position inside a thermoplastic mask due to the high conductivity of the cranium relative to that of thermoplastic [132]. As a result, this technique can detect cranial motion without a direct unobstructed view of the patient and does not require an open-faced thermoplastic mask. The capacitive sensing system is modular and therefore can be easily moved from one treatment room to another.

We have previously reported on the capabilities of this method in detecting translational motion in three dimensions through the thermoplastic mask and in the therapeutic radiation beam [132,133]. This study evaluates the performance of a new capacitive array design for six-dimensional cranial motion detection in the context of a volunteer study.

4.4 Materials and Methods

4.4.1 Detector and Array Design

The capacitive system included a conductive sensor array in the shape of a ring, with inner and outer radii of 8 cm and 16 cm, at the vertex of the cranium. The sensor ring was divided into four quadrants with 5 mm minimum separation between the neighboring quadrants, and each quadrant is covered with a layer of 0.025 mm thick copper foil [132,134]. The proposed array leverages the shunt mode [11] for capacitive motion detection. An illustration depicting this mode is provided in figure 4.1. The shunt mode introduces the grounded body part into the electric field present between two conductive plates. The change induced in the electric field translates into change in sensed capacitance. This mode thus provides the advantage of arranging multiple sensors on the same plate that is positioned at the cranial vertex. This geometry offers several possible advantages, including reducing variation due to facial features, minimizing patient-specific signal variations based on the muscle and fat components, and not obstructing the patient's view.

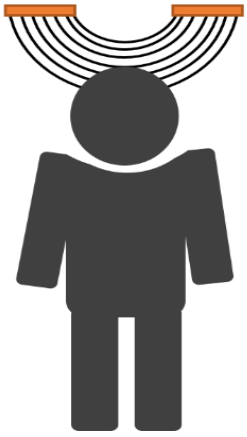

Figure 4.1 Shunt mode for capacitive proximity sensing.

4.4.2 Human Study

The study was approved by the Nova Scotia Health Authority Research Ethics Board (NSHAREB #1022359). The research was conducted in accordance with the principles embodied in the Declaration of Helsinki with local statutory requirements. All participants gave written informed consent to participate in the study.

Twenty-five healthy adult volunteers were included in the study. Each subject was fitted with an S-frame thermoplastic mask affixed to the linear accelerator treatment couch, as shown in figure 4.2. Subject cranial dimensions were determined by measuring the lateral temple separation on the thermoplastic masks. The array was placed at the cranial vertex at 5 mm distance from the closest part of the thermoplastic mask. Depending on the shape of the mask, the closest part of the thermoplastic mask to the array could vary depending on whether the cranium vertex is the most protruding point of the mask. All thermoplastic masks were CT imaged (without the subject) to determine the actual distance achieved between the center of the array and the thermoplastic mask during the experiment. Given that it is difficult to translate and rotate a subject's cranium in a controlled reproducible manner, the cranium was fixed and the array was translated and rotated relative to the cranium using a H-820 6-Axis hexapod stage (Physik Instrumente (PI) GmbH & Co. KG, Auburn, Massachusetts, USA) to simulate cranial translation and rotation with 1.5 μm and 25 μ-radian motion precision, respectively.

The literature is sparse on cranial rotation axes for subjects in treatment position but subject-specific pivot points were established using anatomical landmarks to approximate standard human cranial rotation axes [139]. The first cranial rotation axis was

defined as a line connecting the volunteers' ear canals. The secondary cranial rotation axis was defined as the line perpendicular to the first axis, intercepting it at the midline, and exiting from the cranial vertex. The third cranial rotation axis was defined as the line perpendicular to the first axis, perpendicular to the second axes, and exiting upwards toward the nasal septum [139].

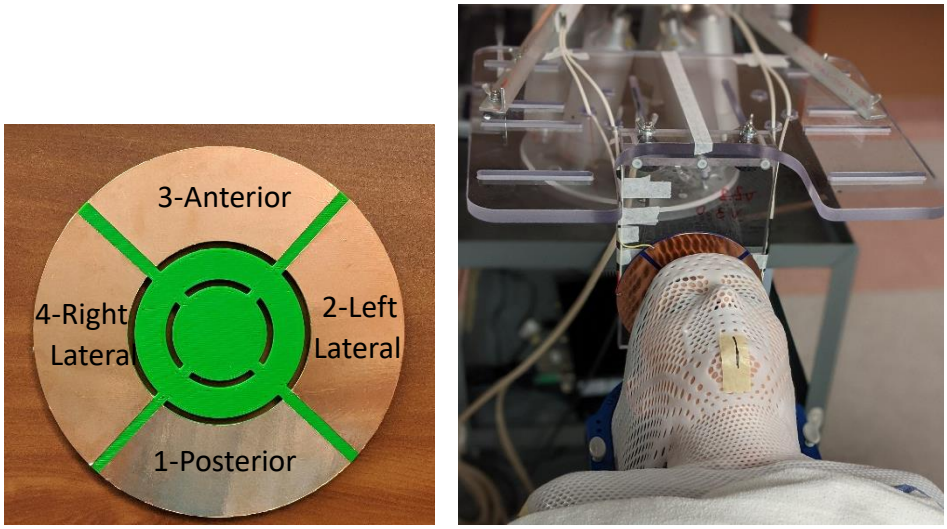

Figure 4.2 The array is comprised of four quadrant sensors and located at the cranial vertex. The backing is 3D printed using PLA (shown in green) covered with copper foil to form the conductive sensors. The array is connected to the hexapod stage and moved to simulate cranial motion.

After establishing the rotation pivot points, the array was moved using the hexapod stage, in 1° steps of rotational motion (roll, pitch, and yaw) and 1 mm steps of translational motion (anterior-posterior, superior-inferior, and left-right). These step sizes were chosen primarily to decrease the subjects' time in the mask to reduce discomfort, as well as cover the anticipated data range required for calibration.

All translations were performed in the range of -2 mm to 2 mm from the original position. The rotations were performed similarly over the range from -2° to 2° except for pitch, for which the range of -2° to 2° could not be reached due to the range of motion on the hexapod stage. Consequently, we chose the range of -1.5° to 1.5° for pitch rotation during the volunteer study. Signals from all four plates were acquired at each position for 8 s using an FDC 2214 proximity sensing chip (Texas Instruments, Dallas, TX) at 20 Hz. Each subject took part in one data acquisition session per day for three consecutive days. Two sets of rotation and two sets of translation data were acquired in each session.

4.4.2.1 Data Processing

While the hexapod stage was used to introduce motion in a controlled manner, additional involuntary volunteer motion during data acquisition could not be prevented. Consequently, the first step of data analysis was to review the data for any additional motion signal during the hexapod stationary states. Out of the twenty-five volunteers, seven were excluded due to their excessive motion during the data acquisition. This was determined based on the fact that the signal stability of the system has been studied and reported previously [132–134], and checked on a daily basis for each day of the experiments. Additionally, physical motions of the volunteers were noted when observed during the experiment and even self-reported by the volunteers in some cases.

Two rotation datasets and two translation datasets were acquired in each session. The translation and rotation datasets with least volunteer motion were selected for each participant. This is done because some volunteers show additional motion as their time in the mask increases while some might show more motion at the beginning of the

experiment and relax over time. A rolling average with a 41 sample window was applied to reduce random noise. This averaging window size was chosen to limit the filter delay to one second. In order to calculate calibration equations, capacitive signal from known motion was required. To isolate known hexapod motion from unknown volunteer motion, any transient signal changes resulting from involuntary motion during a stationary state of the hexapod were removed, and the associated datapoints were eliminated from all four sensor channels. The transient motion was defined as fast, self-correcting motion that show up as spikes in data, superimposed on the steady state, that returned back to the steady state baseline. The spike amplitudes were a minimum of two times the standard deviation of the baseline signal and the spike lengths were larger than 8 samples (at 20 Hz). The capacitance baseline at the original position was subtracted from each of the data sets. A two-tier analysis was used for classification of the 6D motion and subsequent calibration to quantify the motion, as detailed below.

4.4.2.1.1 Classification

Six different types of motions are introduced during the study: superior-inferior, left-right, anterior-posterior, roll, pitch, or yaw. Classification is required to determine the type of cranial motion introduced. Logistic regression is a classical machine learning algorithm widely used for binary classification of data [140–146] and can be expanded to perform multiclass classification [147,148]. In this study, a logistic regression classifier with one-versus-all (OVA) multiclass classification is used to classify all six motion dimensions [147,148]. Motion classification is performed in three steps: feature definition, classifier training, and classifier testing.

In this study, a total of six signals are used as the basis for all classifier features. These signals are the capacitive signals from the four channels (anterior, posterior, right, and left sensor plates) as well as the (left-right) and (posterior-anterior) differential signals. The signals were computed for each dimension of motion using the data acquired on the first day of data acquisition for each volunteer. The two signals with the highest sensitivity on the first day of data acquisition were identified for each dimension of motion, and a second degree polynomial was fitted to each. In total, six pairs of polynomial fits were calculated, for a total of twelve parameterized functions. These functions were applied to their respective signals to yield the twelve raw classifier features.

Feature transformation and standardization were used to improve classifier performance [149]. A logarithmic transformation was applied to each raw feature to reduce the effect of outliers, as shown in equation 4.1**,** where f_{ij} represents the j^{th} raw feature computed on the i^{th} day of data acquisition and f_{ij}' represents the transformed feature. A base of two and a constant term of one were chosen to ensure that raw feature values in the range of zero to one were not attenuated.

$$f_{ij}' = \log_2 \left(abs\left(f_{ij}\right) + 1\right) \qquad \text{eq 4.1}$$

Each transformed feature was then standardized according to the mean and standard deviation of its respective training dataset, as shown in equation 4.2, where f_{ij}'' represents the transformed and standardized feature.

$$f_{ij}'' = \frac{f_{ij'} - mean(f_{1j'})}{std(f_{1j'})} \qquad \text{eq 4.2}$$

Training of the OVA logistic regression multiclass classifier was performed using the transformed and standardized features. These features were calculated from the data acquired on the subject's first session and a classifier model is trained for each subject. Logistic regression models were trained using MATLAB R2020a function *fitclinear* with L2 regularization ($\lambda = 0.12$). Classifier testing was performed using the transformed and scaled features calculated from the data acquired on the second and third acquisition sessions.

4.4.2.1.2 Calibration

Six variables were constructed using the signals acquired from the four sensors by leveraging the geometry of the array and the respective motions. Each variable is used to calibrate the associated motion. Equations 4.3 – 4.8 show the formula for each variable, represented as V, and the subscripts determine the specific motion corresponding to the variable. Subscripts Z, Y, and X represent superior-inferior, left-right, and anterior-posterior translations, respectively. Similarly, roll, pitch, and yaw are specified with subscripts of U, V, and W, respectively. Capacitive signals from the four plates are presented as S with the subscript referring to the sensor plate position with respect to the cranium; posterior, left, anterior, or right. Note that the variables for yaw and left-right motion are similar. This is due to the fact that both the aforementioned motions result in a change in distance between the cranium and lateral plates.

$$V_Z\,(t) = S_{Posterior} + S_{Left} + S_{Anterior} + S_{Right} \qquad \text{eq 4.3}$$

$$V_Y\,(t) = S_{Left} - S_{Right} \qquad \text{eq 4.4}$$

$$V_X\,(t) = S_{Anterior} \quad \text{eq 4.5}$$

$$V_U\,(t) = S_{Posterior} - S_{Anterior} + S_{Right} - S_{Left} \quad \text{eq 4.6}$$

$$V_V\,(t) = S_{Posterior} - S_{Anterior} \quad \text{eq 4.7}$$

$$V_W\,(t) = S_{Left} - S_{Right} \quad \text{eq 4.8}$$

The data acquired from the first session for each volunteer subject was used to calculate the six variables (eqs. 4.3 – 4.8) for each subject. A second degree polynomial function was then fitted to the data to describe the relationship of the variable to the cranial motion for each dimension [132]. The subject-specific fitted functions are used for calibration of the data acquired during the subsequent volunteer session. Since the motion was known, the calibration equations were applied to data acquired each day and the residual error between calculated and actual motion was calculated for each day of the experiment and each motion over the complete subject cohort.

4.4.2.1.3 Detection Precision

Detection precision [133] is a measure of smallest step of motion in each dimension, starting at the origin, that can be detected by the capacitive monitoring array. Detection precision within the ± 1 mm and ± 1° range was calculated for each dimension of motion using equation 4.9, where k, ΔN, and ΔS represent detection precision, noise amplitude at the origin (neutral position), and absolute change in the baseline signal, respectively [133].

$$k = {}^{\Delta N}/_{\Delta S} \quad \text{eq 4.9}$$

For each dimension of motion, two detection precision values (k-values) were defined, corresponding to a step in the positive and a step in the negative direction starting from the neutral position. While ΔN remained the same for both steps, ΔS represented the change in signal mean as a result of the motion. The two k-values were averaged for each motion over the volunteer cohort, resulting in the average detection precision for each motion.

4.5 RESULTS

4.5.1 Human Study

Out of the twenty-five volunteers, seven were excluded due to their excessive motion during the data acquisition. Figure 4.3 shows an example of an excluded data set due to excessive motion exceeding the introduced motion steps during the study. All excluded volunteers exhibited involuntary motion lasting throughout a single steady state with a magnitude larger than the signal change resulting from a single motion step during the experiment.

The cohort of eighteen subjects included in the study was comprised of nine males and nine females, and cranial lateral separation was used to determine the cranial size for the subject cohort. Figure 4.4 (a) shows the cranial lateral separation distribution for this cohort. Based on these data, the cohort of crania were divided to three groups of small (14.4 cm -15.5 cm lateral separation), medium (15.5 cm -16.5 cm lateral separation), and large (16.5 cm -17.5 cm lateral separation). The subject cohort was comprised of seven small, six medium, and five large crania. Figure 4.4 (b) depicts the distance between the thermoplastic mask and the center of the array during the experiments.

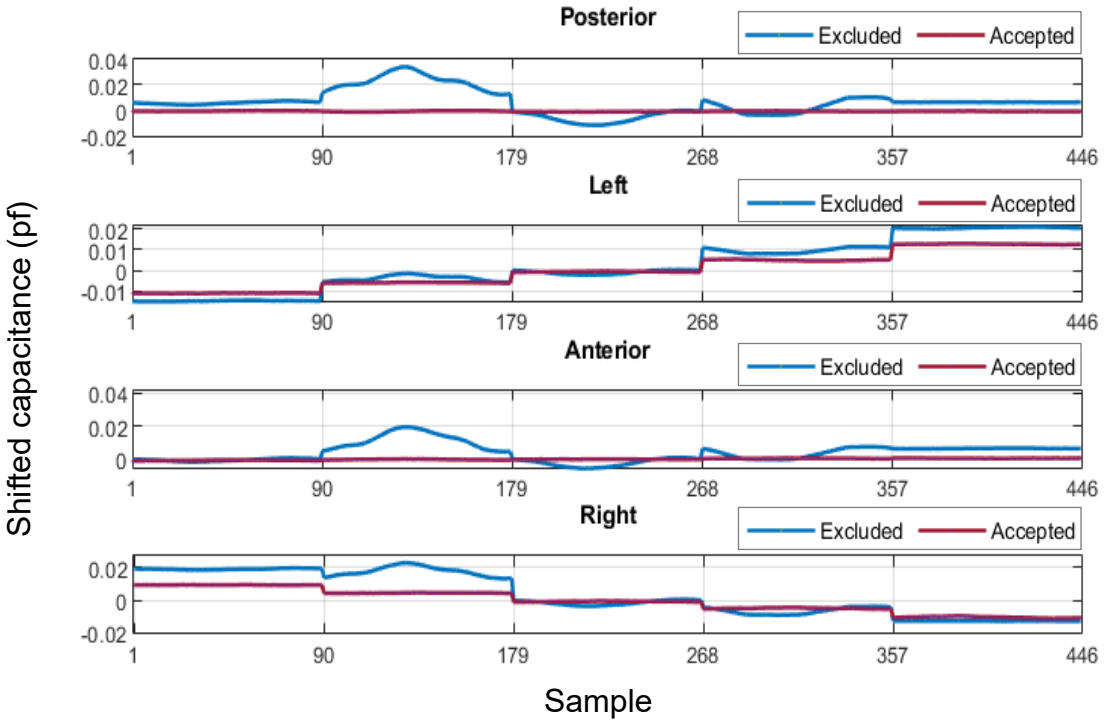

Figure 4.3 An excluded dataset gathered during lateral translation from a subject with excessive involuntary motion (blue) and a similar dataset from a compliant subject (red).

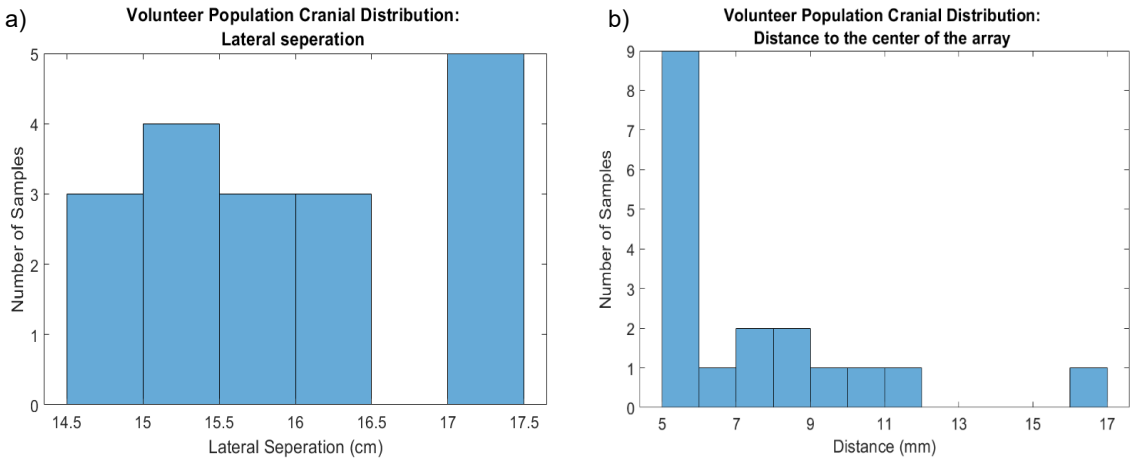

Figure 4.4 (a) The cranial size distribution for the volunteer cohort and (b) the distance between the thermoplastic mask and the center of the array.

4.5.1.1 Data Processing

The involuntary transient motion signals removed during pre-processing had, on average, maximum peak signal 7.0 ± 5.0 times larger than the standard deviation of the corresponding baseline signal and thus were easily removed from the analysis. The average removed signal duration was 37 ± 15 samples at 20 Hz. Figure 4.5 (a) shows an example of an involuntary motion while the hexapod was in a stationary state between anterior-posterior translations. The transient spike in signal resulting from the involuntary motion is marked in red and subsequently removed from the anterior plate data which is the active signal used for anterior- posterior motion calibration (eq. 4.5). The data acquired during that period is removed from all four channels to maintain synchronization between all four signals. The resulting signals are zeroed by subtracting the average baseline capacitance, as shown in figure 4.5 (b). The effects of the remaining smaller involuntary motion that is observed superimposed on the steady state signal is mitigated by the use of the rolling average filter with a window length of 41 samples. The resulting signals are shown in figure 4.5 (c).

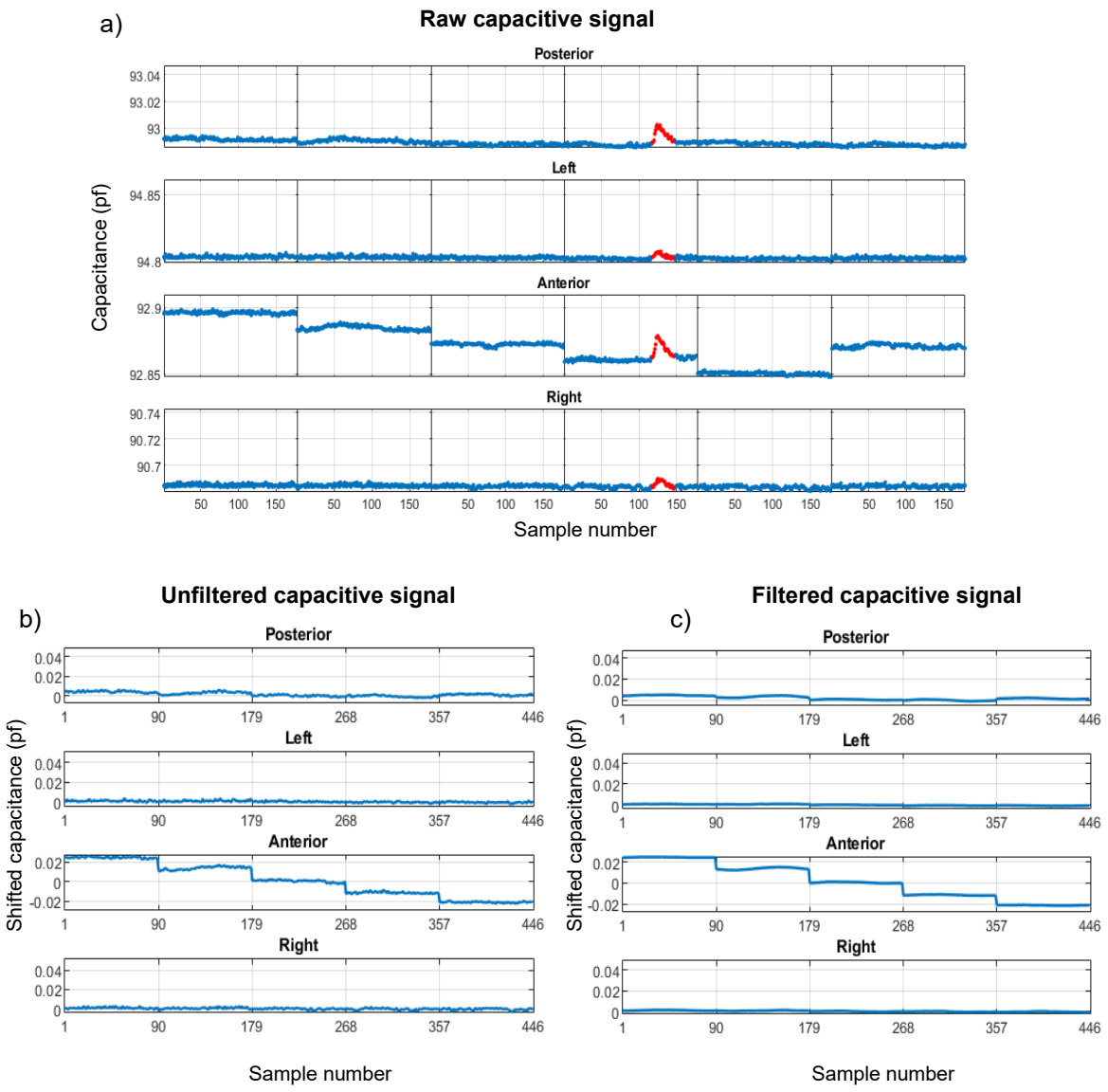

Figure 4.5 (a) The raw signal acquired from each sensor plate during anterior-posterior motion. The red section shows the section of the signal resulting from involuntary motion during the steady state. (b) The cleaned data are shifted by subtracting the baseline, and (c) the cleaned and shifted data are filtered using a rolling average filter with a window width of 41 samples.

4.5.1.1.1 Classification

The performance of the trained classifiers over the subject cohort can be visualized as a confusion matrix. Each row of the matrix illustrates the actual class (truth) while each column represents the predicted class (classifier output), depicting the instances of correct classifier output as well as any confusion between different classes. The confusion matrix shown in figure 4.6 illustrates the accuracy of the trained logistical regression model in classifying the different motion in detecting ± 1° or ± 1 mm of motion for the whole volunteer cohort. Figure 4.6 (a) shows the classifier acting on the data from the first day of experiments (training data) with an average success rate of 96.4 % ± 4.37 %. Figure 4.6 (b) shows the performance of the trained classifier on subsequent data with an average success rate of 92.6 % ± 4.68 %.

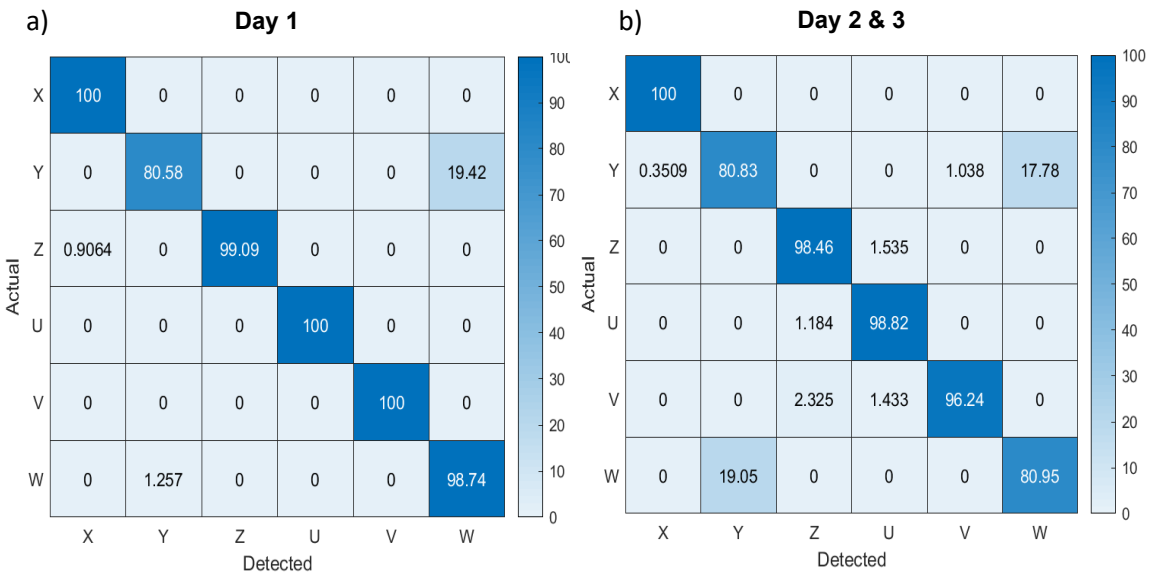

Figure 4.6 Confusion matrices showing the performance of (a) the classifier acting on the data from the first day of experiments (training data) with an average success rate of 96.4 % and (b) the trained classifier on subsequent data with an average success rate of 92.6 %.

The lowest success rates of 80.82 % and 80.95 % refer to the lateral translation and yaw rotation, respectively. The confusion between the two motions can be explained geometrically, as both motions lead to a lateral displacement of the cranium. Additionally, the small training sample size aggravates the effects of any small involuntary motion remaining in the dataset during the steady states. This could increase the chance of confusion in classifying motions with similar displacements.

4.5.1.1.2 Calibration

Calibration equations are used to quantify the magnitude of the motion. The residual error is defined as the difference between the calculated motion and actual motion introduced during the experiment. Residual error associated with calibration of the different motion dimensions is presented in figure 4.7, where the mean and standard deviation of the residual error is shown for each day of the experiment for the whole volunteer cohort (N = 18) for detecting ± 1° or ± 1 mm of motion. As the calibration equations are acquired using data from the first day of the experiments, the associated residual error is an indication of the minimum expected error when using the calibration. Some error is expected on the first day since small involuntary motion of the subjects is observed throughout the experiments.

Overall, the average error and standard deviation resulting from the use of predetermined calibration equations on subsequent days of experiment were -0.01 mm ± 0.19 mm, -0.02 mm ± 0.14 mm, and 0.04 mm ± 0.21 mm for superior-inferior, left-right, and anterior-posterior translation, respectively, while the values associated with roll,

pitch, and raw rotations were -0.04° ± 0.41°, 0.01° ± 0.12°, and -0.02° ± 0.15°, respectively.

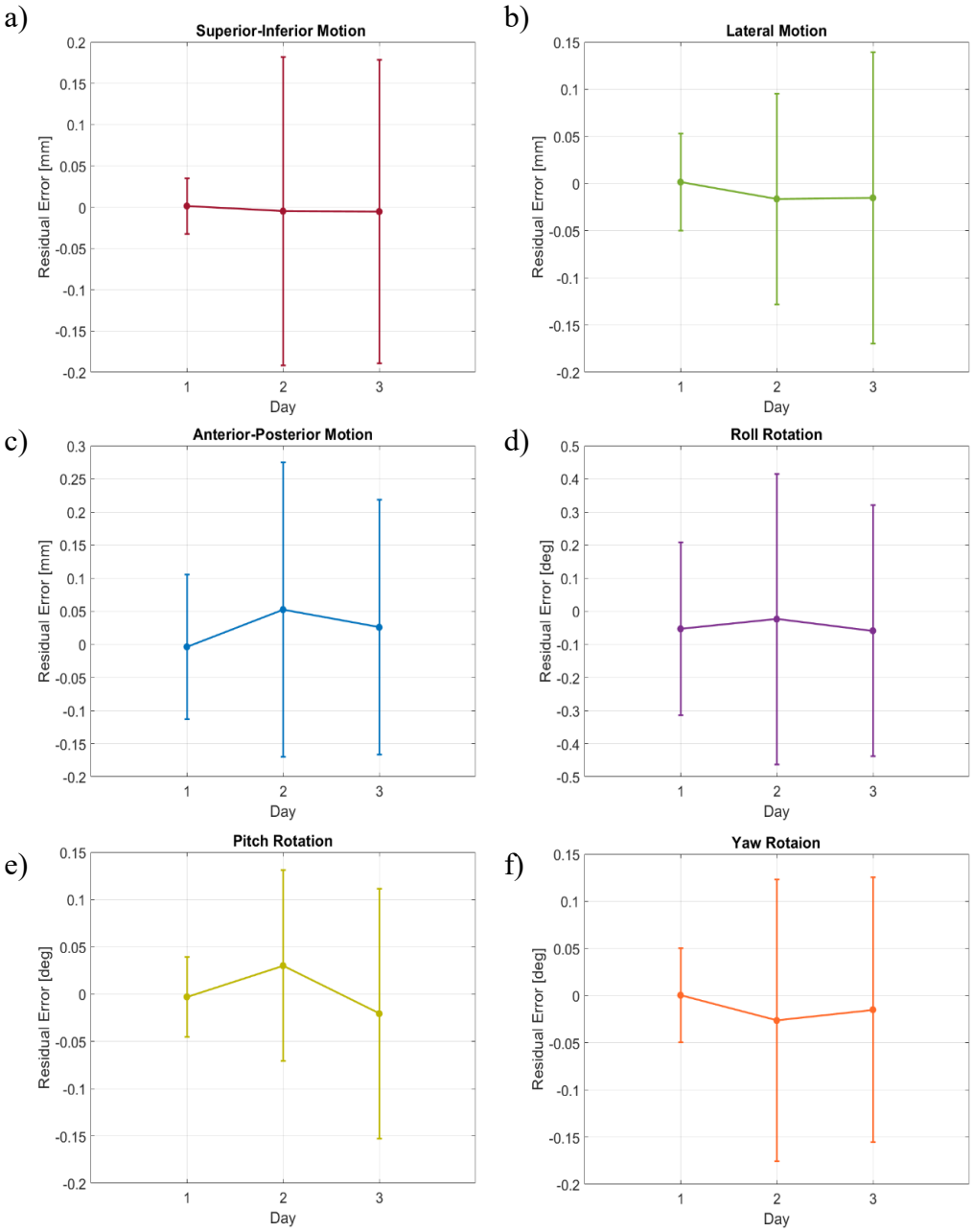

Figure 4.7 Residual error associated with calibration of the different motion dimensions of (a) superior-inferior translation, (b) left-right translation, (c) anterior-posterior translation, (d) roll rotation, (e) pitch rotation, and (f) yaw rotation. The mean value and standard deviation of the residual error is shown for each day of the experiment for the whole volunteer cohort (N = 18).

4.5.1.1.3 Detection Precision

The average detection precision values for different motion dimensions are shown in figure 4.8 over all 18 volunteers for ±1mm and ±1° motion. The translational and rotational motions show sub-millimeter and sub-degree detection precision. Average detection precision in superior-inferior, left-right, and anterior-posterior translations are 0.04 ± 0.02 mm, 0.08 ± 0.03 mm, and 0.14 ± 0.07 mm, respectively. Average detection precision in roll, pitch, and yaw rotations are 0.5° ± 0.3°, 0.05° ± 0.03°, and 0.07° ± 0.04°, respectively.

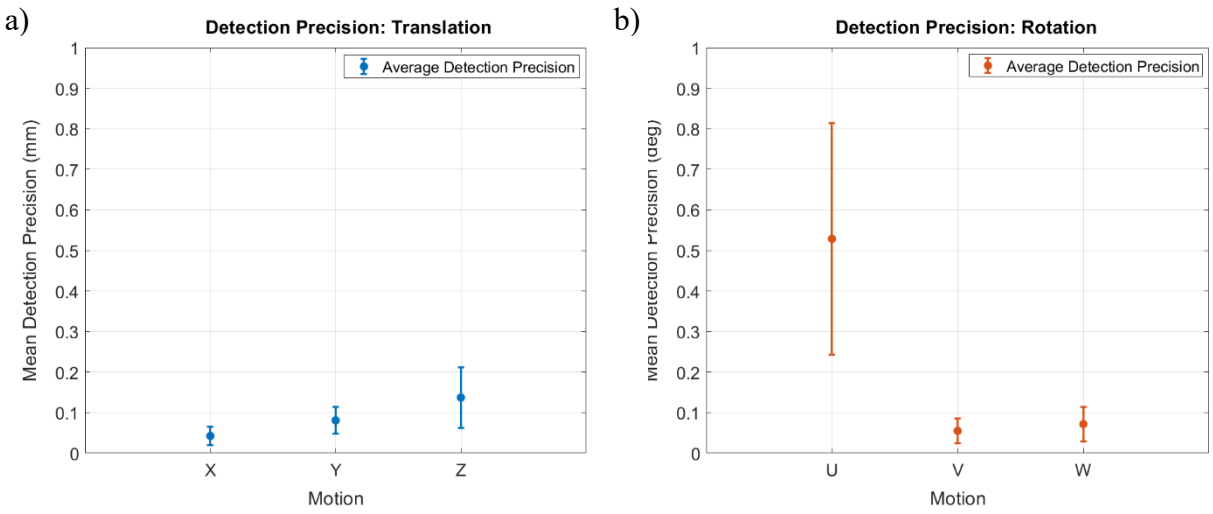

Figure 4.8 Detection precision averaged over the volunteer cohort (N=18) for (a) translational motion (X, Y, and Z represent superior-inferior, left-right, and anterior-posterior dimensions, respectively) and (b) rotational motion (U, V, and W represent roll, pitch, and yaw dimensions, respectively).

4.6 Discussion

The purpose of this investigation was to study the performance of a capacitive monitoring array for 6D cranial motion detection on a volunteer cohort with a range of cranium sizes and shapes. The study shows that the system is capable of 6D motion

detection with sub-millimeter and sub-degree precision. The system offers the unique properties of being non-contact, modular (not room-based), and able to detect the cranium through the thermoplastic mask. For the purpose of this study, the capacitive array was attached to a hexapod stage and moved to simulate cranial motion with high precision and accuracy in order to perform a controlled analysis. However, in a clinical setting, the system would be indexed to the couch and provide continuous motion information. This arrangement would be ideal for use with the emerging noncoplanar [150–152] treatments since maintaining a constant unobstructed view of the subject is not required.

The study shows that a classifier and calibrator can be pre-trained using volunteer data and used on data acquired during subsequent sessions. This means that in a clinical setting, classification and calibration data can be acquired prior to treatment day, e.g., at the time of simulation, similar to the current protocols for acquiring patient respiratory traces prior to treatment. A version of the system would be available at the time of CT simulation. The system would be indexed to the couch, and for calibration the array would be moved in small predefined steps, either manually (e.g. with indexed stops at set positions) or with the use of stepping motors while calibration data is acquired. This motion information would then be used to acquire patient-specific classification and calibration information prior to treatment. While these steps present a practical workflow for calibration, with further development it is also possible that class solutions based on patient geometry could be employed to pre-determine the classifier parameters, thus obviating the need for pre-treatment course calibration, and this remains the subject of a forthcoming investigation.

With regard to use during treatment delivery, absolute patient positioning would be done first, via existing image guidance. The capacitive system would then be 'zeroed' and its acquisition would be started. The continuous capacitive monitoring then provides continuous motion information. Exceeding a user-defined threshold of motion in any of the 6 dimensions would trigger an intervention. This could send an alert to the therapist or interrupt the beam through an interlock, for example. In concept 6D motion data could inform the robotic couch to perform the necessary shifts.

While this study shows the viability of the system in detecting 6D cranial motion, the small subject cohort prevents the use of neural networks to achieve a more universal classifier and calibrator system and study the effects of combined cranial motion in different directions. However, we believe that a natural extension to this study would entail the concurrent use of the capacitive array, indexed to the couch, and a secondary status quo monitoring system with a large study cohort. This would allow the capacitive system to gather more realistic cranial motion information in smaller and varied increments that can be used to train a more robust classifier and calibrator capable of detection and classification of compound cranial motion. Acquiring more data could also improve the behavior of the classifier. Since the patient-specific classifiers in this study were trained on one set of motion data, they could be affected more strongly by noise and outliers and were not trained to classify more complex simultaneous motion in different dimension. This is especially important for yaw and lateral translation that can be confused approximately 18 % of the time. Additionally, design alterations such as increasing the area of the sensor plates or adding an additional plate could help with classification.

The study was conducted by including subjects with minimal involuntary motion. This was due to the nature of the study where known motion steps were required to acquire calibration equations.

4.7 Conclusion

This work introduces a novel, non-ionizing, continuous detector array capable of 6D intrafraction motion detection and shows its applicability for a range of subjects in a volunteer study. The array is placed at the cranial vertex and has been previously shown to be stable under radiation while being able to detect the cranium motion within the thermoplastic mask.

The study shows sub-millimeter and sub-degree detection precision in all six motion dimensions. Average detection precision in superior-inferior, left-right, and anterior-posterior translations was 0.04 ± 0.02 mm, 0.08 ± 0.03 mm, and 0.14 ± 0.07 mm, respectively. Average detection precision in roll, pitch, and yaw rotations was 0.5° ± 0.3°, 0.05° ± 0.03°, and 0.07° ± 0.04°, respectively.

The system provides capacitive information at 20 Hz, which then is used to classify and quantify cranial motion. The trained classifiers have an average success rate of 92.6 % ± 4.68 % for 6D motion classification.

The system performance shows promising results for 6D cranial motion detection. Future work will focus on expanding this technology to detecting more complex simultaneous motion in different dimension.

CHAPTER 5 CAPACITIVE MONITORING SYSTEM FOR REAL-TIME RESPIRATORY MOTION MONITORING DURING RADIATION THERAPY

5.1 PREAMBLE

Following the investigation into cranial translational and rotational intrafraction motion detection, the following manuscript investigates the extension of the capacitive monitoring technology for respiratory motion detection. This chapter focuses on prototype design and testing with the help of human volunteers. The performance of the system is compared with clinical status quo monitoring system. Additionally, the performance of the system is investigated with and without an unobstructed view of the region of interest.

The following chapter only differs from the below manuscript in the addition of revisions to improve clarity. Publication: P. Sadeghi, K. Moran, and J. L. Robar. "Capacitive monitoring system for real-time respiratory motion monitoring during radiation therapy." *Journal of Applied Clinical Medical Physics* 21, no. 9 (2020): 16-24.

5.2 ABSTRACT

This work presents and evaluates a novel capacitive monitoring system (CMS) technology for continuous detection of respiratory motion during radiation therapy. This modular system provides real-time motion monitoring without any contact with the patient, ionizing radiation, or surrogates, such as reflective markers on the skin.

The novel prototype features an array of capacitive detectors that are sensitive to the position of the body and capable of high temporal frequency readout. Performance of

this system was investigated in comparison to the Real-time Position Management (RPM) infrared (IR) monitoring system (Varian Medical Systems, Inc., Palo Alto, USA). The prototype included three (5 cm × 10 cm) capacitive copper sensors in one plane, located at a distance of 8 cm to 10 cm from the volunteer. Capacitive measurements were acquired for central and lateral-to-central locations during chest free-breathing and abdominal breathing. The RPM IR data were acquired with the reflector block at corresponding positions simultaneously. The system was also tested during deep inspiration and expiration breath-hold maneuvers.

CMS data demonstrate close agreement with the RPM status quo at all locations examined. Cross-correlation analysis on RPM and CMS data showed an average absolute lag of 0.07 s (range: 0.03 s to 0.23 s) for DIBH and DEBH data and 0.15 s (range: 0 s to 0.43 s) for free breathing with the CMS data lagging behind in all but two instances. Amplitude difference between the normalized CMS and RPM amplitude signals during chest and abdominal breathing was within 0.15 for 94.3 % of the data points after synchronization. CMS performance was not affected when the subject was clothed.

This novel technology permits sensing of both free-breathing and breath-hold respiratory motion. It provides data comparable to the RPM system, but without the need for an IR tracking camera in the treatment room or use of reflective markers on the patient.

5.3 INTRODUCTION

External beam radiation therapy (RT) involves the precise delivery of ionizing radiation to pre-defined locations within the body to kill cancer cells while sparing the

surrounding healthy tissue. For many sites, special attention to motion management is required to ensure accurate delivery. One of the most prevalent sources of motion is respiration, and it has a prominent effect when treating breast, lung, or abdominal indications. Management of respiratory motion can result in improved targeting accuracy and reduced normal tissue toxicity, and also ameliorates imaging motion artifacts, thereby enabling improved tumor visualization and alignment [153,154]. Common methods of motion management include reduction of motion through abdominal compression, gating to a specific breathing amplitude or phase, or performing defined breath-hold maneuvers, such as Deep Inspiration Breath Hold (DIBH) and Deep Expiration Breath Hold (DEBH). The DIBH method works by delivering the treatment while the patient holds their breath at the end of a deep inhalation. This method, when used during breast radiation treatment, for example, largely eliminates the breathing motion and pushes the heart further away from the radiation field for left sided breast cancer treatments [153,155,156]. Similarly, the DEBH method works by delivering the treatment while the patient holds their breath at the end of a deep exhalation. For thoracic or abdominal indications, DIBH/DEBH acts to stabilize tumor motion, allowing for decreased planning and treatment margins [153,155,157]. However DEBH maneuvers have reportedly shown higher reproducibility and stability [80,81]. Breath-hold techniques have shown dosimetric advantages and have become widely used [158]. In contrast, respiratory gating methods do not eliminate the breathing motion. Rather, they introduce a gating window wherein the radiation beam is delivered during a predefined phase of the breathing cycle. The aforementioned techniques require a continuous monitoring system to ensure the reproducibility of the breathing pattern or breath-hold position, and the systems employed have traditionally included: laser or optical surface

scanning, spirometry, infrared marker tracking, or implanted radiofrequency transponders [153,154,158–163].

Implanted radiofrequency transponders are used for motion management, but involve surgical intervention with a chance of major or minor complications, transponder migration, and introduce imaging artifacts [163]. Spirometric methods work by voluntarily or involuntarily blocking the patient's breathing. While this may minimize motion, the approach may be limited by a patient's limited respiratory capacity, as well as the equipment costs and patient preparation time [158]. Infrared tracking devices rely on a limited number of markers placed on the patient's abdomen or thorax. Markers may be obscured from the IR camera view by patient body habitus and often need to be placed prior to having complete knowledge of the patient's breathing habits [154,162]. While laser or optical based surface imaging provides a non-contact three-dimensional view of the chestwall anatomy, camera placement must allow a non-obstructed view of the patient's chestwall surface. Accurate surface imaging can be hindered by the position of the gantry/imaging arms and immobilization devices, requires the patient to be fully uncovered throughout the treatment, and may be affected by body hair [161]. Maintaining a constant and unobstructed view with either reflective markers or surface imaging methods may become more challenging with emerging non-coplanar treatments [151,152].

In this work, we present the first report of a capacitive-sensing technology capable of detecting respiratory motion. The technology extends the application of capacitive sensors described previously [132] in a geometry suitable for sensing motion in various regions of the thoracic or abdominal anatomy. In the development of the prototype device described herein, we aimed to satisfy the requirements of i) not requiring direct contact

with the patient, ii) modularity, i.e., a portable device that is moveable and indexable between treatment systems and imaging couch tops, iii) capacity to sense motion through clothing or plastic immobilization devices [132], and iv) high temporal frequency (200 Hz) in detecting respiratory motion. We compare this novel technology with the status quo infrared marker tracking approach.

5.4 Materials and Methods

5.4.1 Capacitive Sensing and Prototype Design

Our respiratory monitoring system works by tracking the position of the area of interest, e.g., chest wall or abdomen. It can detect the motion of the region of interest (ROI) and provide information used for gating or determining breath-hold amplitude. The system is comprised of thin (0.0254 mm) copper conductive sensors mounted on an acrylic horizontal plate above the patient's chest or abdominal area. The human body is naturally electrically conductive [88,95,96], therefore placing the copper sensors close to the body forms a capacitor. A review of electrical properties of bone performed by Singh *et al.* reported that conductivity values can vary based on the sample [100], but in general, bone exhibits low conductivity in the range of 4.5×10^{-3} S/m to 10^{-2} S/m. Skin also exhibits low conductivity with values around 10^{-5} S/m at low frequencies [101] and is considered an insulator [102]. Muscle tissue possesses a conductivity of 0.2 S/m to 0.3 S/m [95] and excised lung tissue possesses a conductivity of 0.1 S/m [164]. In its simplest form, the capacitance of a parallel plate system follows equation 5.1 and shows that capacitance depends on the distance between the plates (d), the area of the capacitor plates (A), and the material between the plates, which is introduced as permittivity (ε). Therefore, capacitance will change as the distance between the sensor and patient changes due to breathing.

$$C = \varepsilon \, {}^{A}/_{d} \qquad \text{eq 5.1}$$

Constant monitoring of the system capacitance allows tracking of the motion of the region of interest. Multiple sensors can be used to track the motion of different regions of the body depending on the clinical needs. Capacitive monitoring of the system can be accomplished by using a capacitive proximity sensor such as MPR121 (Freescale Seminconductor, Inc., Austin, USA). This system has been shown to be stable in linac conditions and under high dose rate photon irradiation [132].

The prototype shown in figure 5.1 is indexed to the treatment couch and can be moved in the cranial-caudal direction to monitor the respiratory motion of different areas, such as the chest or abdomen. The sensor platform height can be adjusted to accommodate different body types, and the current prototype is 60 cm wide, 20 cm deep, and 41 cm high.

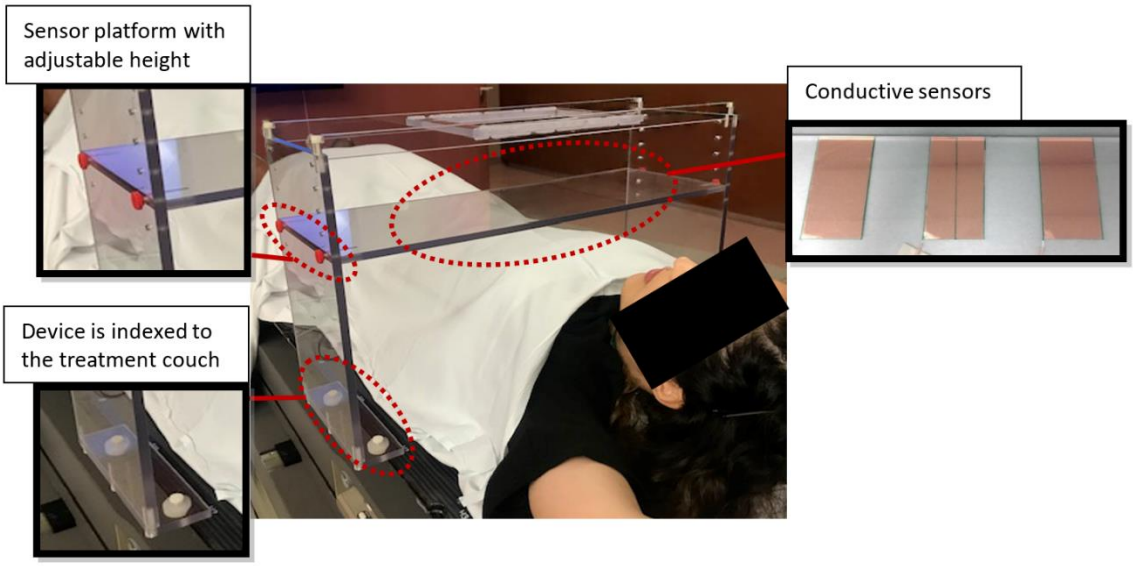

Figure 5.1 The design of the relocatable respiratory CMS prototype. Three capacitive pads are 5 cm by 10 cm each and mounted 5 cm apart. The current prototype is 60 cm wide, 20 cm deep, and 41 cm high.

The thin conductive copper sensors can be placed on the platform in midline or lateral to midline position to monitor the respiratory motion of different regions of interest. Three capacitive sensors are 5 cm by 10 cm each and mounted 5 cm apart. The sensors do not come in contact with the patient at any time. While the substrate for the sensors is acrylic in this prototype, in a clinical version of the device we anticipate that this would be replaced by a rigid, minimally attenuating material, such as thin carbon fiber. Additionally, the final design will be optimized to reduce the amount of carbon fiber in the beam, accommodate patient habitus, and reduce gantry clearance issues similar to existing devices, such as abdominal compression devices. Further optimization would also provide flexibility by allowing for an arms-down setup.

To ensure clearance with the gantry, the prototype was placed around an anthropomorphic phantom as shown in figure 5.2. The phantom was placed at 95 cm SSD to the xiphoid position, and gantry clearance was found to be sufficient during 180° rotation. Additionally, CBCT images were acquired to ensure no artifacts are introduced in the presence of the copper sensors (figure 5.2).

(a) (b)

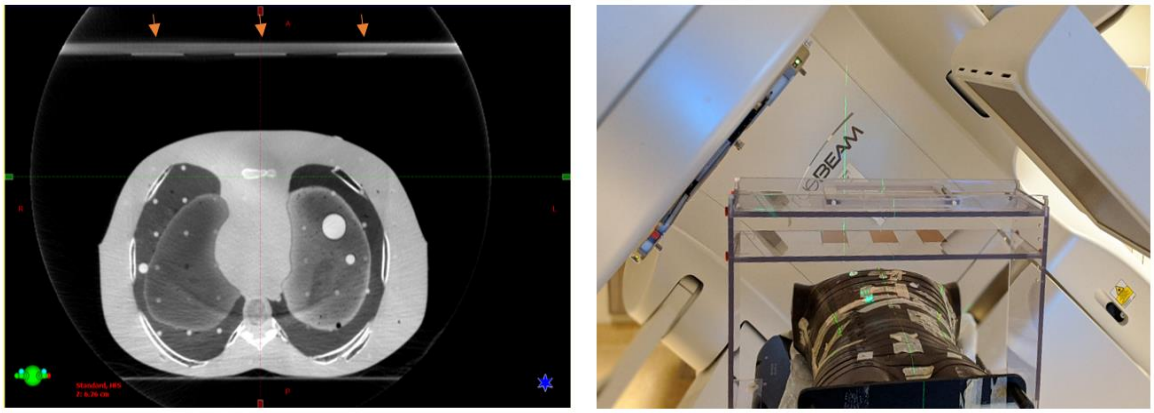

Figure 5.2 (a) Cone beam CT acquired of the CMS prototype with an anthropomorphic phantom on the linac couch at 95 cm SSD on the Xiphoid position shows no significant image artifacts due to the presence of the copper sensors. The three copper sensors are marked with arrows on the image. (b) The setup and gantry clearance.

5.4.2 Respiratory Motion Detection

Data collection was performed with the help of a volunteer. The volunteer was made comfortable using a knee wedge and positioned supine on the couch, comfortably level, with both arms raised and supported on an indexed breast board (Civco Radiotherapy, Orange City, USA). The breast board was centrally indexed to the treatment couch using a standard carbon fiber locating bar (CDR Systems, Calgary, Canada). Experiments were conducted on a Lightspeed CT simulator (GE Healthcare, Chicago, USA) equipped with standard flat top carbon fiber couch top and Real-time Position Management (RPM) system (Varian Medical Systems, Inc., Palo Alto, USA). The CMS sensors have been shown to be unaffected by the environment of the linear accelerator, and a similar setup and measurement could be achieved in the CT simulator environment [132].

The RPM block was set up in contact with the anatomy of interest (lateral or central position on chest or abdomen), and the CMS sensor array was located anterior to the same region. The volunteer was asked to take a deep breath to synchronize both systems in post processing. The CMS system was setup to acquire data for 150 s at 200 Hz using in-house software. Once the CMS data acquisition was concluded, the RPM system was turned off. The CMS data were processed using an exponential weighting method with a forgetting factor of 0.99 [165] followed by a moving average filter of 10 samples to reduce random noise. The exponential weighting method applies a set of weights to the data samples recursively, such that as the age of the data increases, the weighting factor decreases exponentially. The value of the forgetting factor determines the rate of change for the weighting factors [165].

The data were synchronized and normalized to compare the behavior of the two systems. Cross-correlation analysis was performed to determine any relative time lag (phase shift) between the two datasets. Since the CMS data were acquired at 200 Hz it was down-sampled to 30 Hz to match the RPM data to allow cross-correlation analysis. Amplitude comparison was performed on synchronized and normalized CMS and RPM data during free breathing after applying the cross-correlation shifts.

To investigate the similarity of the measurements from the two systems under different possible clinical conditions, experiments were repeated during chest breathing, belly breathing, deep inhalation, and expiration breath-hold.

5.4.2.1 Free Breathing

Breathing amplitude traces were acquired during chest free-breathing using CMS and RPM simultaneously for three ROIs: central, where the central sensor was place on the xiphoid process; and left/right lateral, where the sensors were placed 5 cm lateral to the central sensor. An additional set of measurements was acquired during abdominal free breathing for central and lateral ROIs which were 10 cm inferior to the chest breathing ROIs.

In each case, the RPM block was affixed to the volunteer's skin and the CMS sensor was positioned above the ROI (central or lateral position on the chest or the abdomen) with a distance of about 8 cm to10 cm from the skin surface. When placing the RPM block in lateral positions, gauze was placed under the block to compensate for the natural curvature of the body and keep the RPM block level and in view of the IR camera.

The volunteer was instructed by a radiation therapist to perform chest breathing by concentrating on sternal rise and fall during inhale/exhale, and belly breathing by concentrating on abdominal rise and fall during inhale/exhale. The volunteer was instructed to maintain even breathing by counting to four each for inhale and exhale. A total of six chest breathing and seven abdominal breathing experiments were performed.

5.4.2.2 Deep Inspiration/Expiration Breath-Hold

Breathing traces were acquired during DIBH and DEBH using CMS and RPM simultaneously for the central region of interest (xiphoid process). In each case, the RPM

block was affixed to the volunteer's skin and the CMS sensor was above the ROI with a distance of 8 cm to10 cm from the volunteer.

The volunteer was coached by a radiation therapist to take a slow deep breath to maximally inflate the chest and to maintain this maneuver for approximately 20 s to 25 s for DIBH. For DEBH, the volunteer was asked to slowly exhale and maximally deflate the chest and to maintain this maneuver for approximately 20 s to 25 s. Additionally, the volunteer was instructed not to arch their back during DIBH/DEBH maneuvers. The volunteer was given time to practice maneuvers and breathing instructions prior to data capture.

5.4.2.3 Motion Detection with Obstructed View

Performance of the CMS system was tested with no direct view of the chest. The volunteer was clothed and the CMS sensor was placed above the xiphoid, again at an 8 cm to 10 cm distance from the skin, and data were gathered for three DIBH instances. The RPM system was inoperable in this scenario due to the fact that the reflective block could not be stably positioned on clothing.

5.4.3 Effect of Sensor-Body Separation on Signal to Noise Ratio (SNR)

Another set of volunteer experiments was performed on a Varian Clinac EX accelerator (Varian Medical Systems, Inc., Palo Alto, USA) to determine the effect of different sensor-body distances on the signal and the SNR values, as well as ensure that no additional effects are present as a result of migration to the linac environment. The volunteer was made comfortable using a knee wedge and positioned supine on the couch,

comfortably level, with both arms raised and supported on an indexed breast board (Civco Radiotherapy, Iowa, USA). These experiments monitored abdominal respiration with the sensor placed 10 cm inferior to the xiphoid process in the absence of the RPM block at sensor-body distances of 3.5 cm, 5.5 cm, and 7.5 cm. These distances are dictated by the geometry of the prototype and the available positions for the adjustable sensor platform.

Signal to noise ratio was calculated for the raw data using equation 5.2, where A denotes the amplitude of signal or noise as specified by the subscript.

$$SNR = \left(\frac{A_{Signal}}{A_{Noise}}\right)^2 \qquad \text{eq 5.2}$$

The amplitude of the signal was defined as the average change in acquired signal from exhale to inhale point (breathing amplitude) over the 120 s of data acquisition. The noise was estimated on a 0.005 s rolling window by calculating the signal change between two adjacent data points, averaged over the time series of acquired data (120 s), and rounded. This provides an understanding of the ratio between the range of signal and the amplitude of noise, which can be helpful for clinical comparison and decision making.

5.5 Results

5.5.1 Capacitive Sensing and Prototype Design

Figure 5.2 illustrates the gantry clearance with the prototype in place in the linac environment. A snapshot of the acquired CBCT is shown in figure 5.2 (b) to show that the presence of copper did not introduce image artifacts.

5.5.2 Free Breathing

Data for the xiphoid sensor trace during chest and abdominal breathing are shown in figure 5.3. Cross-correlation analysis performed on the simultaneously acquired CMS and RPM signals shows an average absolute lag of 0.16 s (range: 0.03 s to 0.43 s) and 0.14 s (range: 0 s to 0.27 s) for chest and abdominal breathing, respectively, with the down-sampled capacitive data lagging behind the RPM data in all but two instances out of thirteen. Figure 5.4 shows a histogram of normalized amplitude differences between the CMS and RPM results after applying the cross-correlation shift during chest and abdominal breathing. On average, over all thirteen chest and abdominal free-breathing trials, the amplitude of 94.3 % of CMS and RPM data points were within 15 % of each other by direct comparison of the normalized amplitude values of the RPM and CMS time series acquired simultaneously. In other words, a difference of 0.15 or less was observed between 94.3 % of data points. When considering only the central sensor experiments, the value increased to 98.2 % and 99.8 % for chest and abdominal breathing, respectively. The normalized amplitude difference histograms are shown in figure 5.4.

5.5.3 Deep Inspiration/Expiration Breath-Hold

Breathing traces for DIBH and DEBH are shown in figure 5.5. The CMS trace during DEBH shows additional noise compared to the RPM data. This is mainly due to the fact that the distance between the chest and sensor plates are maximized during expiration breath-hold, leading to a decrease in capacitance in accordance with equation 5.1. Cross-correlation analysis shows an average absolute lag of 0.07 s (range: 0.03 s to

0.23 s) between the CMS and RPM data during DEBH and DIBH maneuvers combined, with the down-sampled capacitive data lagging behind the RPM data.

(a)

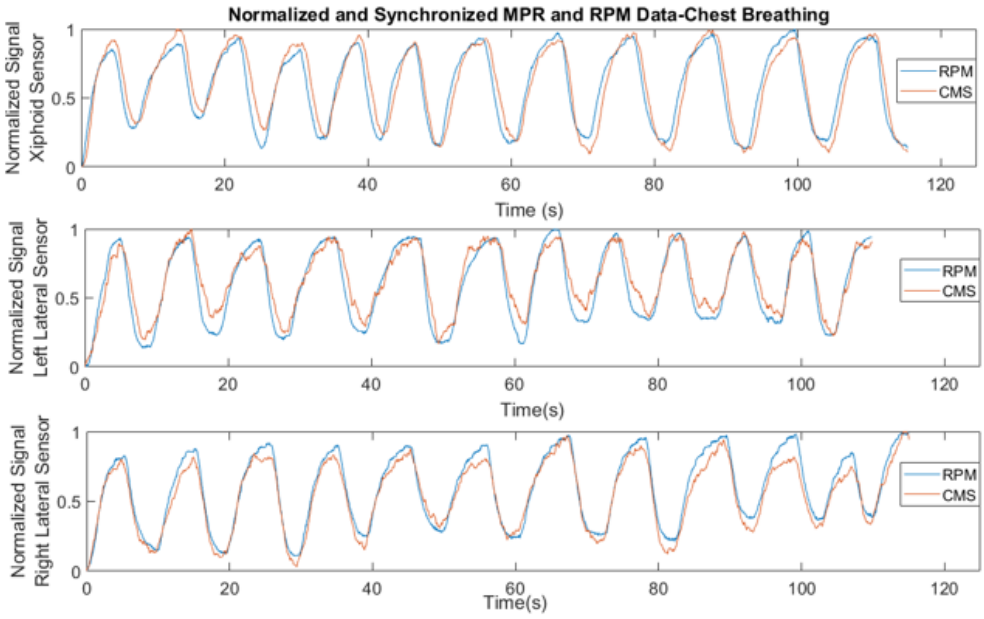

(b)

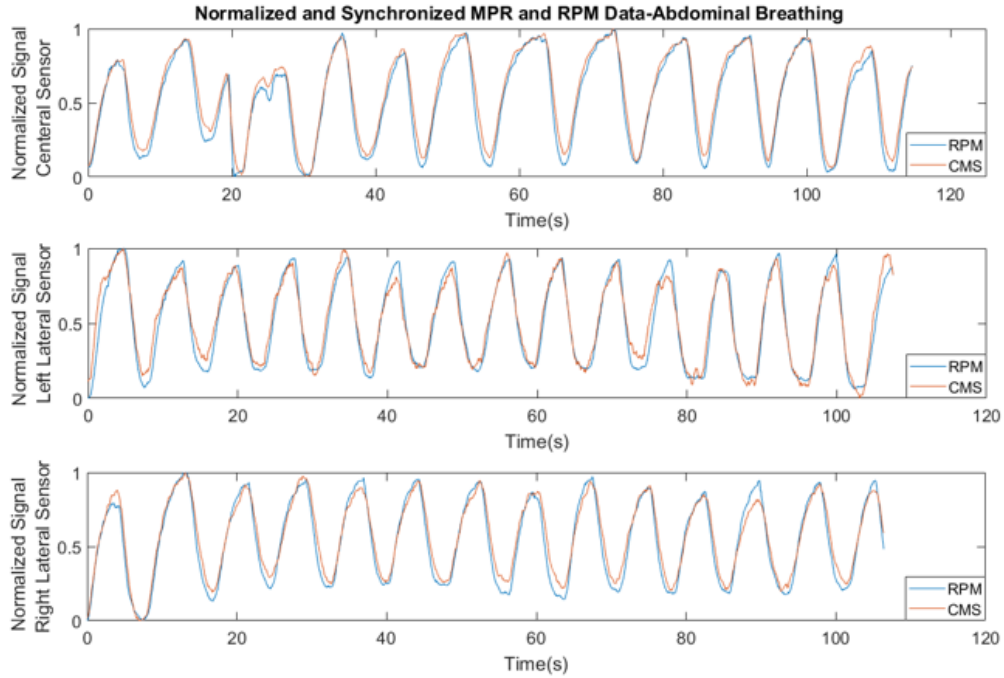

Figure 5.3 Simultaneous RPM and CMS breathing signal gathered from (a) chest free breathing and (b) abdominal free breathing for central, left lateral and right lateral locations. The central sensor was placed on the xiphoid process and 10 cm inferior to the xiphoid process for chest and abdominal breathing, respectively. The lateral sensors were positioned 5 cm lateral to central sensor.

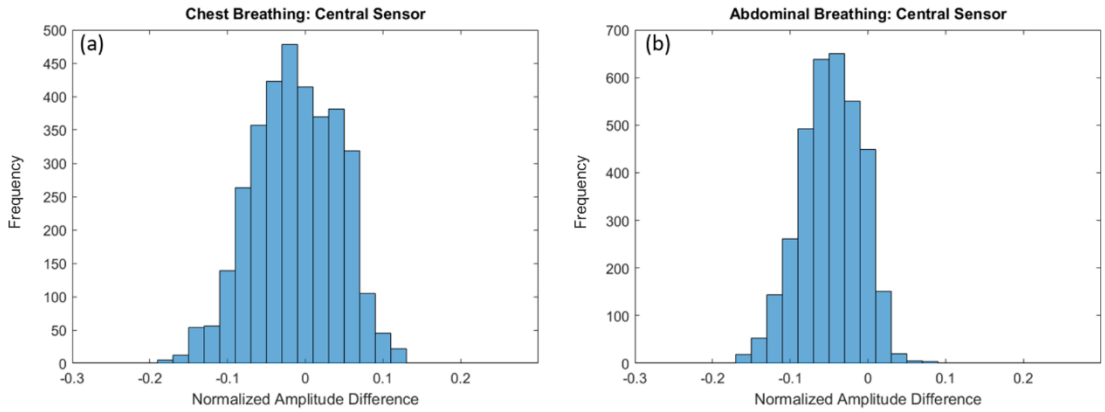

Figure 5.4 Histogram of normalized amplitude difference between CMS and RPM systems during chest (a) and abdominal (b) breathing. Data were gathered using the central sensor.

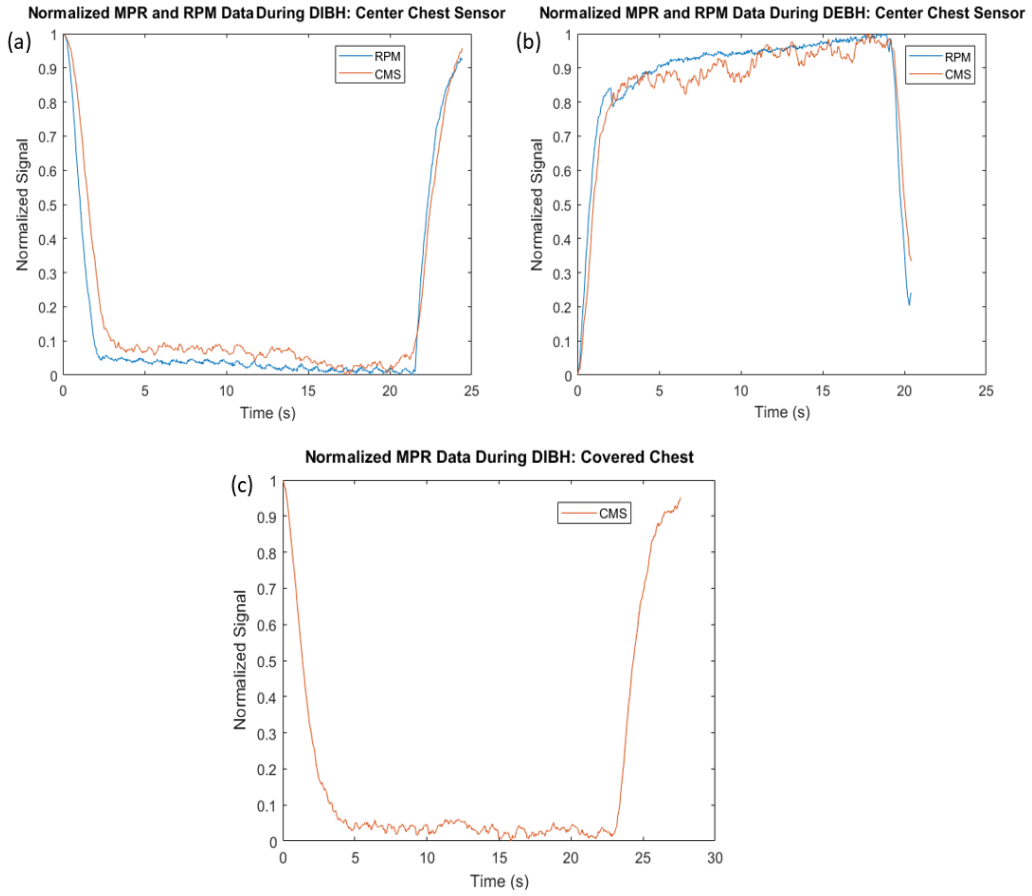

Figure 5.5 Simultaneous RPM and CMS breathing signal gathered during (a) DIBH and (b) DEBH. Sensors were placed over the xiphoid process on bare chest. (c) CMS breathing signal gathered using the central sensor during DIBH with obstructed view of the chest (the volunteer was clothed).

5.5.4 Motion Detection with Obstructed View

Figure 5.5c shows the results for the DIBH data acquired with the clothed volunteer using CMS, demonstrating that the presence of clothing between the sensor and skin does not pose a limitation for the system.

5.5.5 Effects of Sensor-Body Separation on Signal to Noise Ratio (SNR)

Figure 5.6 shows the raw and post-processed signal at different sensor-body separation values. Signal to noise ratio for the raw signal is shown on each graph. The SNR values decrease as the sensor-body distance increases with SNR values of 113, 363, and 1419 corresponding to sensor-body distances of 7.5 cm, 5.5 cm, and 3.5 cm, respectively. While our experiments, performed with CMS and RPM systems at large sensor-body separation (8-10 cm), provide evidence that detection is possible at the lower SNR value range, we recommend minimum possible sensor-body distance for improved SNR.

5.6 DISCUSSION

This manuscript presents a novel method for non-contact respiratory motion detection. The system provides near real-time (200 Hz) respiratory motion information during treatment. The system is modular, low cost in comparison to IR or surface monitoring cameras, requires no contact with the patient, and offers the flexibility of using different regions of interest. Additionally, the system does not require unobstructed view of the patient, as it can detect motion through clothes and was previously shown to detect human motion even within a full thermoplastic mask [132]. As a result, it can be used in conjunction with different thermoplastic immobilization systems or simple blankets. The

sensors and acquisition system have been shown to be stable in the linac environment and under high dose rate photon irradiation [132].

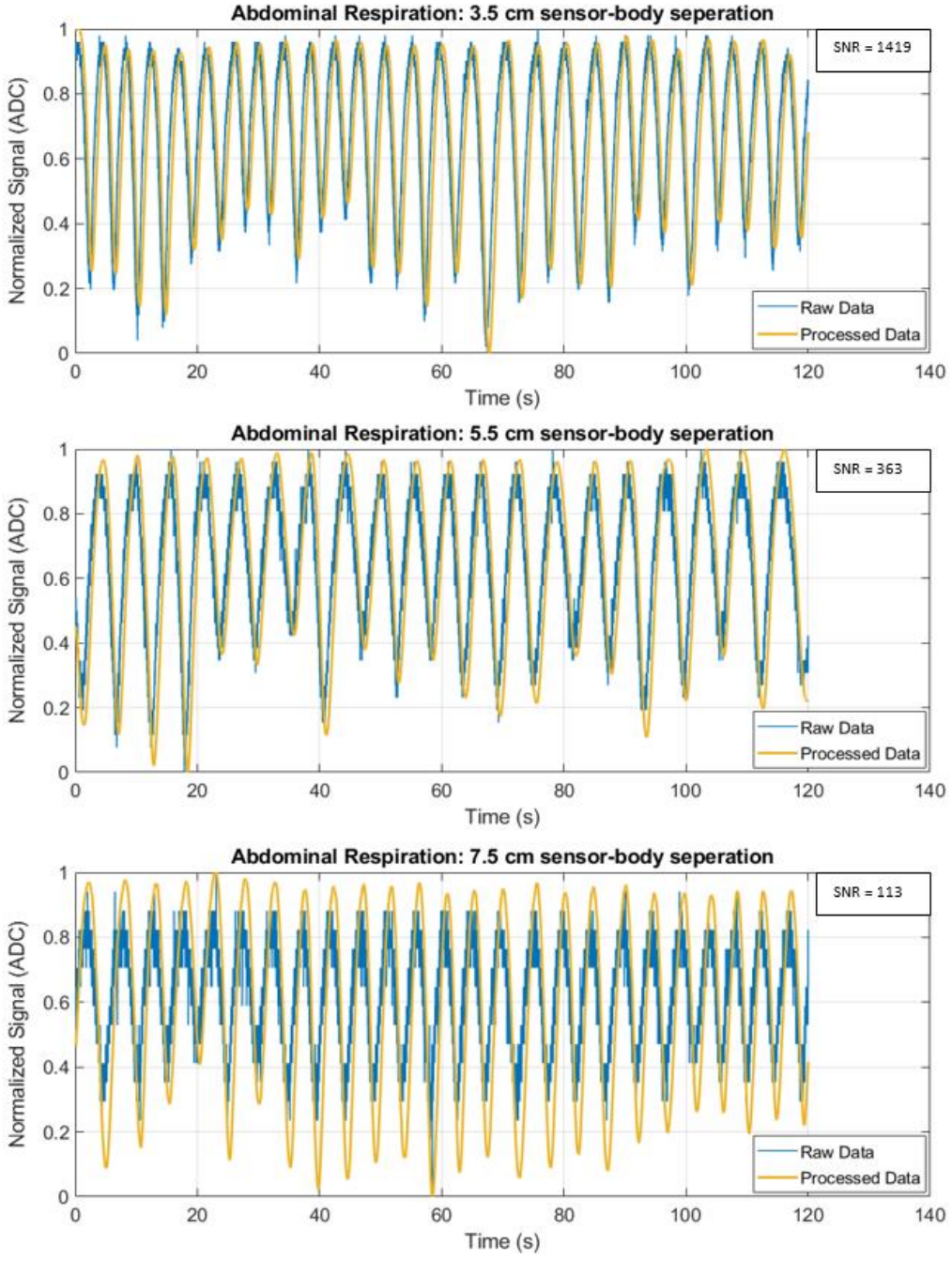

Figure 5.6 Normalized raw and post-processed CMS signal acquired during abdominal respiration at different sensor-body distances. Signal to noise ratio for the raw signal is shown on each graph. The data are acquired at 200 Hz and processed using an exponential weighting method with a forgetting factor of 0.99 followed by a moving average filter of 10 samples (0.05 s) to reduce random noise.

The modular nature of this device presents several advantages relative to IR or surface imaging camera-based systems: (a) the device may be coupled reproducibly to a couch top and therefore may be relocated easily between treatment units, CT, PET/CT or angiography platforms; (b) it may be used outside of these rooms, e.g., on a mock-up of a treatment couch, thereby providing an offline platform for patient education and coaching without tying up expensive capital equipment resource; and (c) the device could be produced at comparatively low cost, which is amenable to equipping multiple treatment and imaging rooms. Cost is increasingly important as techniques such as DIBH for treatment of left-sided breast cancer become more common [166].

Additionally, While the RPM system detects motion from a single plane, the CMS sensor detects one single capacitance value that is related to the average distance between the sensor and the body over the area of the sensor. As the breathing occurs, the distance between the sensor and body surface varies. The distance averaging resulting from a strip sensor geometry, rather than a point sensor, helps detect the global respiratory motion despite the curvature of the individual's body.

The system charge/discharge time is 2 μs and draws a low current of 24 μA with the charge/discharge process, which occurs at 200 Hz. Considering these variables, and the fact that the dielectric material used in this case is air, no significant capacitive leakage or stability issues are observed or expected.

The capacitive system signal relies on the electrical conductivity of the body. This precludes conducting a phantom study, specifically in the chest/abdominal area. In this study, the CMS detection system was used on two volunteers to acquire proof of concept

data and to investigate the viability of the design. However, our next step would be a clinical study with a cohort of volunteers in different clinical setup positions. The presented CMS data shows good agreement with the RPM infrared monitoring system that has been used for both gating and breath-hold monitoring in our institution. However, increased noise in signal was observed in case of DEBH (figure 5.5). This was mainly due to the fact that our CMS sensors were mounted farther away from the chest to allow enough space for the RPM block to be attached to the patient while still ensuring no contact between the block and the CMS sensors occurred during the different breathing stages. This distance was maximized during the DEBH and the increase in the chest-to-sensor distance resulted in a decrease in capacitance and an increase in noise. This effect could be mitigated during normal operation of the system with the sensors mounted closer to the patient in the absence of the RPM block.

The cross-correlation analysis shows a small lag between the RPM and CMS systems. The average absolute lag value of 0.15 s was observed for free breathing. The absolute lag value averaged over all instances of DIBH and DEBH was 0.07 s. A contributing factor to the lag is the synchronization process of the RPM and CMS positioning data. That, combined with the mandatory down-sampling of the high frequency MPR data from 200 Hz to 30 Hz, in order to perform the cross-correlation analysis, could explain the sub-second lag values due to interpolation used to match the frequencies on the two datasets. Additionally, the respiratory motion with larger amplitude (DIBH/DEBH) shows almost twice the average lag value compared to the respiratory motion with smaller amplitude (free breathing). We believe parameters such as the nature of post-processing of data (our protocol vs. what might be used in the RPM

software) and the change in capacitive signal sensitivity at different sensor-body distances could also be responsible for this difference.

Amplitude comparison analysis for RPM and CMS central chest and abdominal experiments, showed that on average, 98.2 % and 99.8 % of all data points were within 15 % of one another for chest and abdominal breathing, respectively. The value decreased to 94.3 % when averaged over all chest and abdominal respiration experiments for central and lateral sensors. This is possibly due to the fact that, in order to detect the lateral motion using the RPM block, the block is taped in place on a curved section of the body surface and gauze is placed under the block to help compensate for the curvature of the body, and this may introduce additional uncertainties in the RPM data due to the reduced stability of the RPM block during respiratory motion.

A comparison of the raw and processed signals shows a slight temporal shift in the processed data. This difference could be important in the context of clinical respiratory phase gating. The phase shift was measured at the maxima (end of exhale point) for the cases presented in figure 5.6 and was found to be 6.5°, 8°, and 10° for 3.5 cm, 5.5 cm, and 7.5 cm sensor-body separation, respectively. As a result, reducing the sensor-body distance is advised, for example to 4 cm, in clinical conditions. Considering a 40 % gating window as an example [167] (144°), the introduced phase shift at low sensor-body separation would lead to a small (6.5° / 144° = 4.5 %) uncertainty.

While this comparison was made to show the similarity between the operation of this technology compared to a clinical status quo (RPM), clinical use of the CMS device would require the acquisition of the breathing trace at the time of CT simulation and during

treatment with the CMS device. This would reduce any effects of inter-device variations in respiratory amplitude detection.

The current prototype provides one dimensional positional information regarding respiratory motion. In concept, the system can be extended to include a larger array of sensors in different axial planes to provide a three-dimensional mapping of respiratory motion during treatment. The prototype described herein included an acrylic frame for ease of machining and construction. A clinical version will be made of carbon fiber, which is the status quo for clinical accessories in radiation therapy due to its radio-transmissive properties. Additionally, the current design only requires an area of 10 cm by 5 cm for the conductive sensor. This allows for reducing the size of the sensor platform (figure 5.1) and optimizing the design to reduce the amount of carbon fiber in the beam, accommodate larger patient habitus, and increase gantry clearance similar to existing devices, such as abdominal compression devices.

5.7 Conclusion

This work presents a novel, non-contact, and modular technology for real time monitoring of respiratory motion. The current prototype can detect respiratory motion at different regions, providing positional data at 200 Hz readout frequency. The system is minimally intrusive as it does not require unobstructed view of the chest, and can provide motion detection for extracranial lesions through fabric or thermoplastic immobilization material. [132] Furthermore, the system requires no contact with the patient and is not anchored to a treatment room. This study acts as proof of concept and our next step would be a clinical study with a cohort of volunteers in different clinical setup positions.

CHAPTER 6 CONCLUSION

6.1 SUMMARY

The purpose of this thesis was to develop a novel technology for intrafraction patient motion monitoring during SRS and SBRT treatment. Our main design criteria were that it should be:

• **Continuous** – the system should offer continuous patient motion monitoring throughout the treatment.

• **Non-ionizing** – the system should not use ionizing radiation to acquire motion information.

• **Non-contact** – the system should not come in contact with the patient at any point. This would minimize any infection-control restrictions arising from having a system used by multiple patients and assist with workflow efficiency.

• **Sensitive to the human body and insensitive to common immobilization accessories** – the system should be insensitive to common immobilization accessories such as the thermoplastic material. This means that the system should be capable of detecting the cranium through the thermoplastic mask without having a direct view of the cranium. Similarly, the system should detect respiratory motion through blankets and articles of clothing.

• **Modular and portable** – the system is not room based. It is modular and can be moved from one treatment room to another.

With the above-mentioned criteria in mind, our first prototype was designed and constructed for cranial motion monitoring during SRS treatment (Chapter 2). The system was shown to be capable of translational motion detection with sub-millimetre accuracy. The system was stable under radiation and was insensitive to the thermoplastic immobilization mask.

Following the proof of concept prototype, finite element analysis modeling was used to simulate the response of different capacitive arrays due to cranial translation and rotation (Chapter 3). The model was verified against experimental data and the most promising array design was chosen for a volunteer study.

A volunteer study was conducted to investigate the performance of the array design to different cranium shapes and sizes (Chapter 4). The system was shown to have sub-millimetre and sub-degree detection accuracy.

In addition to the implementation of this capacitive monitoring technique for cranial motion detection, the system was modified to detect respiratory motion during SBRT treatment (Chapter 5). A prototype was designed and constructed, and the system performance was compared against a clinical status quo motion monitoring system. Our system was capable of detecting respiratory motion despite clothing articles obstructing direct view of the region of interest.

6.2 Future Work

The work conducted in this thesis introduces a new technology with working prototype designs applicable to motion tracking during SRS and SBRT treatment. While the results are promising, multiple refinements and expansions can be made to improve

the system as well as apply the technology to other treatment sites. Refinements to the 6D cranial motion detection array could improve array sensitivity and motion classification and calibration through different modifications, such as addition of sensor plates, increasing the sensor plate areas, and improving the classification and calibration algorithms. Additionally, the system needs to be tested for more complicated motion detection such as simultaneous rotation and translation motion. The respiratory detection prototype could also be refined to provide 3D motion information through addition of sensor plates and implementing a classification algorithm. Additionally, the behavior of the system could be examined in the presence of fiducial markers. The technology also could be expanded to provide intrafraction motion monitoring for other extracranial treatment sites. For example, a prototype could be designed to detect intrafraction motion during spinal radiation treatment.

In summation, this thesis introduces a working novel technology, outlines the process of design and refinement of multiple prototypes, and evaluates their performance in a clinical setting. This information can be used as a roadmap for further improvements and expansions of the system.

BIBLIOGRAPHY

1. Chung HT, Kim DG. Introduction to radiosurgery. *J Korean Med Assoc*. 2008;51(1):5-15. doi:10.5124/jkma.2008.51.1.5
2. Ma L, Nichol A, Hossain S, et al. Variable dose interplay effects across radiosurgical apparatus in treating multiple brain metastases. *Int J CARS*. 2014;9:1079-1086. doi:10.1007/s11548-014-1001-4
3. Ruiz EAA. A CAPACITIVE MONITORING SYSTEM FOR STEREOTACTIC RADIOSURGERY: DETECTOR DESIGN. Published online 2017.
4. Bichay TJ, Mayville A. The Continuous Assessment of Cranial Motion in Thermoplastic Masks During CyberKnife Radiosurgery for Trigeminal Neuralgia. *Cur us*. 2016;8(5):e607. doi:10.7759/cureus.607
5. Minniti G, Valeriani M, Clarke E, et al. Fractionated stereotactic radiotherapy for skull base tumors: Analysis of treatment accuracy using a stereotactic mask fixation system. *Radiat Oncol*. 2010;5(1). doi:10.1186/1748-717X-5-1
6. Ali I, Tubbs J, Hibbitts K, et al. Evaluation of the setup accuracy of a stereotactic radiotherapy head immobilization mask system using kV on-board imaging. *J Appl Clin Med Phys*. 2010;11(3):26-37. doi:10.1120/jacmp.v11i3.3192
7. Babic S, Lee Y, Ruschin M, et al. To frame or not to frame? Cone-beam CT-based analysis of head immobilization devices specific to linac-based stereotactic radiosurgery and radiotherapy. *J Appl Clin Med Phys*. 2018;2:111-120. doi:10.1002/acm2.12251
8. Ramakrishna N, Rosca F, Friesen S, Tezcanli E, Zygmanszki P, Hacker F. A clinical comparison of patient setup and intra-fraction motion using frame-based radiosurgery versus a frameless image-guided radiosurgery system for intracranial lesions. *Radiother Oncol*. 2010;95(1):109-115.
9. Gevaert T, Verellen D, Engels B, et al. Clinical evaluation of a robotic 6-degree of freedom treatment couch for frameless radiosurgery. *Int J Radiat Oncol Biol Phys*. 2012;83(1):467-474.
10. Gabriel C, Peyman A. Dielectric properties of biological tissues; variation with age. In: *Conn's Handbook of Models for Human Aging*. Elsevier; 2018:939-952. doi:10.1016/B978-0-12-811353-0.00069-5
11. Smith J, White T, Dodge C, Paradiso J, Gershenfeld N, Allport D. Electric field sensing for graphical interfaces. *IEEE Comput Graph Appl*. 1998;18(3):54-59. doi:10.1109/38.674972
12. Canadian Cancer Statistics Advisory Committee. Canadian Cancer Statistics. Toronto, ON: Canadian Cancer Society. Available at: cancer.ca/Canadian-Cancer-Statistics-2019-EN , [Accessed May 2021].
13. *American Society for Radiation Oncology, ASTRO Legislative Priorities*.; 2015. Accessed May 26, 2021. www.astro.org%7Cwww.rtanswers.org

14. *American Society of Radiation Oncology, ASTRO Legislative Priorities*.; 2017.

15. Hall EJ. *Radiobiology for the Radiologist*. 7th ed.. Philadelphia : Wolters Kluwer Health/Lippincott Williams & Wilkins; 2012.

16. Podgorsak EB. *Review of Radiation Oncology Physics: A Handbook for Teachers and Students*. INTERNATIONAL ATOMIC ENERGY AGENCY VIENNA, AUSTRIA; 2003.

17. Halvorsen PH, Cirino E, Das IJ, et al. AAPM-RSS Medical Physics Practice Guideline 9.a. for SRS-SBRT. Published online 2017. doi:10.1002/acm2.12146

18. Klein EE, Hanley J, Bayouth J, et al. Task Group 142 report: Quality assurance of medical accelerators a… Fang-Fang Yin. Published online 2009. doi:10.1118/1.3190392

19. Shaw E, Scott C, Souhami L, et al. Single dose radiosurgical treatment of recurrent previously irradiated primary brain tumors and brain metastases: Final report of RTOG protocol 90- 05. *Int J Radiat Oncol Biol Phys*. 2000;47(2):291-298. doi:10.1016/S0360-3016(99)00507-6

20. Loeffler JS, Kooy HM, Wen PY, et al. The treatment of recurrent brain metastases with stereotactic radiosurgery. *J Clin Oncol*. 1990;8(4):276-582. doi:10.1200/jco.1990.8.4.576

21. Hanson PW, Elaimy AL, Lamoreaux WT, et al. A concise review of the efficacy of stereotactic radiosurgery in the management of melanoma and renal cell carcinoma brain metastases. *World J Surg Oncol*. 2012;10(1):1-4. doi:10.1186/1477-7819-10-176

22. Barnholtz-Sloan JS, Sloan AE, Davis FG, Vigneau FD, Lai P, Sawaya RE. Incidence proportions of brain metastases in patients diagnosed (1973 to 2001) in the Metropolitan Detroit Cancer Surveillance System. *J Clin Oncol*. 2004;22(14):2865-2872. doi:10.1200/JCO.2004.12.149

23. Flickinger JC, Dade Lunsford L, Linskey ME, Duma CM, Kondziolka D. Gamma knife radiosurgery for acoustic tumors: multivariate analysis of four year results. *Radiother Oncol*. 1993;27(2):91-98. doi:10.1016/0167-8140(93)90127-T

24. Black PM, Tariq F. What Every Neurosurgeon Should Know About Stereotactic Radiosurgery. In: *Textbook of Stereotactic and Functional Neurosurgery*. Springer Berlin Heidelberg; 2009:977-986. doi:10.1007/978-3-540-69960-6_63

25. Engenhart R, Kimmig BN, Höver KH, et al. Stereotactic single high dose radiation therapy of benign intracranial meningiomas. *Int J Radiat Oncol Biol Phys*. 1990;19(4):1021-1026. doi:10.1016/0360-3016(90)90028-I

26. Kondziolka D, Lunsford LD, Coffey RJ, Flickinger JC. Stereotactic radiosurgery of meningiomas. In: *Journal of Neurosurgery*. Vol 74. Journal of Neurosurgery Publishing Group; 1991:552-559. doi:10.3171/jns.1991.74.4.0552

27. Fokas E, Henzel M, Wittig A, Grund S, Engenhart-Cabillic R. Stereotactic radiosurgery of cerebral arteriovenous malformations: Long-term follow-up in 164 patients of a single institution. *J Neurol*. 2013;260(8):2156-2162.

doi:10.1007/s00415-013-6936-9

28. Byun J, Kwon DH, Lee DH, Park W, Park JC, Ahn JS. Radiosurgery for cerebral arteriovenous malformation (AVM): Current treatment strategy and radiosurgical technique for large cerebral AVM. *J Korean Neurosurg Soc*. 2020;63(4):415-426. doi:10.3340/jkns.2020.0008

29. Friehs GM, Park MC, Goldman MA, Zerris VA, Norén G, Sampath P. Stereotactic radiosurgery for functional disorders. *Neurosurg Focus*. 2007;23(6):E2. doi:10.3171/FOC-07/12/E3

30. Celis MA, Garduño OAG, Moreno-Jiménez S. Stereotactic Radiosurgery for Epilepsy. In: *Shaped Beam Radiosurgery*. Springer Berlin Heidelberg; 2011:219-228. doi:10.1007/978-3-642-11151-8_19

31. Mousavi SH, Niranjan A, Huang MJ, et al. Early radiosurgery provides superior pain relief for trigeminal neuralgia patients. *Neurology*. 2015;85(24):2159-2165. doi:10.1212/WNL.0000000000002216

32. Pokhrel D, Sood S, Mcclinton C, et al. Linac-based stereotactic radiosurgery (SRS) in the treatment of refractory trigeminal neuralgia: Detailed description of SRS procedure and reported clinical outcomes. *J Appl Clin Med Phys*. 2017;18(2):136-143. doi:10.1002/acm2.12057

33. Leksell L. The stereotactic method and radiosurgery of the brain. *Acta Chir Scand*. 1952;102:316-319.

34. Johns HE, Bates LM, Watson TA. 1000 Curie cobalt units for radiation therapy. I. The Saskatchewan. *Br J Radiol*. 1952;25(294):296-302. doi:10.1259/0007-1285-25-294-296

35. Leksell L. Stereotactic radiosurgery. *Neurosurgery, and Psychiatry*. 1983;46:797-803. doi:10.1136/jnnp.46.9.797

36. Leksell L. Irradiation of small structures through the skull. *Acta radiol Onicol Radiat Phys Biol*. 1974;13:512-534.

37. Benedict S, Schlesinger D, Goetsch S, Kavanagh B. *Stereotactic Radiosurgery and Stereotactic Body Radiation Therapy*. CRC Press; 2015.

38. Betti O, Derenchinsky V. Hyperselective encephalic irradiation with linear accelerator. *Acta Neurochir*. 1984;Suppl 33:385-390.

39. Colombo F, Benedetti A, Pozza F, et al. External Stereotactic Irradiation by Linear Accelerator. *Neurosurgery*. 1985;16(2):154-160. doi:10.1227/00006123-198502000-00005

40. Lutz W, Winston KR, Maleki N. A system for stereotactic radiosurgery with a linear accelerator. *Int J Radiat Oncol*. 1988;14(2):373-381. doi:https://doi.org/10.1016/0360-3016(88)90446-4

41. Podgorsak EB, Pike GB, Olivier A, Pla M, Souhami L. Radiosurgery with high energy photon beams: a comparison among techniques. *Int J Radiat Oncol Biol Phys*. 1989;16(3):857-865. doi:10.1016/0360-3016(89)90506-3

42. Sahgal A, Roberge D, Schellenberg D, et al. The Canadian Association of Radiation Oncology Scope of Practice Guidelines for Lung, Liver and Spine Stereotactic Body Radiotherapy. *Clin Oncol*. 2012;24(9):629-639. doi:10.1016/j.clon.2012.04.006

43. Benedict SH, Yenice KM, Followill D, et al. Stereotactic body radiation therapy: The report of AAPM Task Group 101. *Med Phys*. 2010;4078:4078. doi:10.1118/1.3438081

44. Gunderson LL, Tepper JE, Bogart JA. *Clinical Radiation Oncology*. Fourth edi. Philadelphia, PA : Elsevier; 2016.

45. Kelley KD, Benninghoff DL, Stein JS, et al. Medically inoperable peripheral lung cancer treated with stereotactic body radiation therapy. *Radiat Oncol*. 2015;10(1):1-9. doi:10.1186/s13014-015-0423-7

46. Choy H, Akerley W, Safran H, et al. Multiinstitutional phase II trial of paclitaxel, carboplatin, and concurrent radiation therapy for locally advanced non-small-cell lung cancer. *J Clin Oncol*. 1998;16(10):3316-3322. doi:10.1200/JCO.1998.16.10.3316

47. McPartlin A, Swaminath A, Wang R, et al. Long-Term Outcomes of Phase 1 and 2 Studies of SBRT for Hepatic Colorectal Metastases. *Int J Radiat Oncol Biol Phys*. 2017;99(2):388-395. doi:10.1016/j.ijrobp.2017.04.010

48. McPartlin AJ, Barry AS, Murray L, et al. Stereotactic Body Radiation Therapy for Colorectal Liver Metastases—Long-Term Follow-up of a Single Center's Sequential Prospective Studies. *Int J Radiat Oncol*. 2016;96(2):E184. doi:10.1016/j.ijrobp.2016.06.1052

49. Sandler KA, Veruttipong D, Agopian VG, et al. Stereotactic body radiotherapy (SBRT) for locally advanced extrahepatic and intrahepatic cholangiocarcinoma. *Adv Radiat Oncol*. 2016;1(4):237-243. doi:10.1016/j.adro.2016.10.008

50. Dahele M, Fehlings MG, Sahgal A. Stereotactic radiotherapy: An emerging treatment for spinal metastases. *Can J Neurol Sci*. 2011;38(2):247-250. doi:10.1017/S0317167100011410

51. Thibault I, Chang EL, Sheehan J, et al. Response assessment after stereotactic body radiotherapy for spinal metastasis: A report from the SPIne response assessment in Neuro-Oncology (SPINO) group. *Lancet Oncol*. 2015;16(16):e595-e603. doi:10.1016/S1470-2045(15)00166-7

52. Sahgal A, Bilsky M, Fehlings MG, et al. Stereotactic body radiotherapy for spinal metastases: current status, with a focus on its application in the postoperative patient: A review. *J Neurosurg Spine*. 2011;14(2):151-166. doi:10.3171/2010.9.SPINE091005

53. Park JJ, Hajj C, Reyngold M, et al. Stereotactic body radiation vs. intensity-modulated radiation for unresectable pancreatic cancer) Stereotactic body radiation vs. intensity-modulated radiation for unresectable pancreatic cancer Stereotactic body radiation vs. intensity-modulated radiatio. *Acta Oncol (Madr)*. 2017;56:1746-1753. doi:10.1080/0284186X.2017.1342863

54. Phillips JG, Wo JY, Hong TS. Stereotactic body radiation therapy (SBRT) for pancreatic and non-hepatobiliary gastrointestinal (GI) malignancies. *J Radiat Oncol*. 2013;2(4):381-390. doi:10.1007/s13566-012-0027-x

55. Milano MT, Zhang H, Metcalfe SK, Muhs AG, Okunieff P. Oligometastatic breast cancer treated with curative-intent stereotactic body radiation therapy. *Breast Cancer Res Treat*. 2009;115(3):601-608. doi:10.1007/s10549-008-0157-4

56. Trovo M, Furlan C, Polesel J, et al. Radical radiation therapy for oligometastatic breast cancer: Results of a prospective phase II trial. *Radiother Oncol*. 2018;126(1):177-180. doi:10.1016/j.radonc.2017.08.032

57. Schell MC, Bova FJ, Larson DA, et al. Stereotactic radiosurgery. *AAPM Rep*. 1995;54.

58. Willoughby T, Lehmann J, Bencomo JA, et al. Quality assurance for nonradiographic radiotherapy localization and positioning systems: Report of Task Group 147. *Med Phys*. 2012;39(4):1728-1747. doi:10.1118/1.3681967

59. Guckenberger M, Roesch J, Baier K, Sweeney RA, Flentje M. Dosimetric consequences of translational and rotational errors in frame-less image-guided radiosurgery. *Radiat Oncol*. 2012;7(1):63.

60. Feygelman V, Walker L, Chinnaiyan P, Forster K. Simulation of intrafraction motion and overall geometric accuracy of a frameless intracranial radiosurgery process. *J Appl Clin Med Phys*. 2008;9(4):68-86.

61. Murphy MJ, Chang SD, Gibbs IC, et al. Patterns of patient movement during frameless image-guided radiosurgery. *Int J Radiat Oncol Biol Phys*. 2003;55(5):1400-1408. doi:S0360301602045972 [pii]

62. Mangesius J, Seppi T, Weigel R, et al. Intrafractional 6D head movement increases with time of mask fixation during stereotactic intracranial RT-sessions. doi:10.1186/s13014-019-1425-7

63. Tarnavski N, Engelholm SA, Af Rosenschold PM. Fast intra-fractional image-guidance with 6D positioning correction reduces delivery uncertainty for stereotactic radiosurgery and radiotherapy. *J radiosurgery SBRT*. 2016;4(1):15-20. Accessed May 27, 2021. http://www.ncbi.nlm.nih.gov/pubmed/29296422

64. Kang KM, Chai GY, Jeong BK, et al. Estimation of optimal margin for intrafraction movements during frameless brain radiosurgery. *Med Phys*. 2013;40(5):51716. doi:10.1118/1.4801912 [doi]

65. Li W, Cashell A, Lee I, et al. Patient perspectives on frame versus mask immobilization for gamma knife stereotactic radiosurgery Journal of Medical Imaging and Radiation Sciences. *J Med Imaging Radiat Sci*. 2020;51:567-573. doi:10.1016/j.jmir.2020.08.001

66. Badakhshi H, Barelkowski T, Wust P, Budach V, Boehmer D, Graf R. Intrafraction variations in linac-based image-guided radiosurgery of intracranial lesions. *Cancer/Radiothérapie*. 2013;17(7):664-667. doi:http://dx.doi.org.ezproxy.library.dal.ca/10.1016/j.canrad.2013.05.011

67. Wurm RE, Erbel S, Schwenkert I, et al. Novalis frameless image-guided noninvasive radiosurgery: initial experience. *Neurosurgery*. 2008;62(suppl_5):A11-A18.

68. Davies ER. *Machine Vision: Theory, Algorithms, Practicalities*. Burlington: Elsevier Science & Technology; 2005.

69. Willoughby T, Lehmann J, Bencomo JA, et al. Quality assurance for nonradiographic radiotherapy localization and positioning systems: Report of Task Group 147. *Med Phys*. 2012;39(4):1728-1747. doi:10.1118/1.3681967

70. Gevaert T, Verellen D, Tournel K, et al. Setup accuracy of the Novalis ExacTrac 6DOF system for frameless radiosurgery. *Int J Radiat Oncol Biol Phys*. 2012;82(5):1627-1635.

71. Ackerly T, Lancaster CM, Geso M, Roxby KJ. Clinical accuracy of ExacTrac intracranial frameless stereotactic system. *Med Phys*. 2011;38(9):5040-5048. doi:10.1118/1.3611044 [doi]

72. Li G, Ballangrud Å, Kuo LC, et al. Motion monitoring for cranial frameless stereotactic radiosurgery using video-based three-dimensional optical surface imaging. *Med Phys*. 2011;38(7):3981-3994. doi:http://dx.doi.org/10.1118/1.3596526

73. Manger RP, Paxton AB, Pawlicki T, Kim G. Failure mode and effects analysis and fault tree analysis of surface image guided cranial radiosurgery. *Med Phys*. 2015;42(5):2449-2461.

74. Bertholet J, Knopf A, Eiben B, et al. Real-time intrafraction motion monitoring in external beam radiotherapy. *Phys Med Biol*. 2019;64. doi:10.1088/1361-6560/ab2ba8

75. Keall PJ, Mageras GS, Balter JM, et al. The management of respiratory motion in radiation oncology report of AAPM Task Group 76. *Med Phys*. 2006;33(10):3874-3900. doi:10.1118/1.2349696

76. Brandner ED, Chetty IJ, Giaddui TG, Xiao Y, Huq MS. Motion management strategies and technical issues associated with stereotactic body radiotherapy of thoracic and upper abdominal tumors: A review from NRG oncology. *Med Phys*. 2017;44(6):2595-2612. doi:10.1002/mp.12227

77. Dieterich S, Green O, Booth J. SBRT targets that move with respiration. *Phys Medica*. 2018;56:19-24. doi:10.1016/j.ejmp.2018.10.021

78. Mahadevan A, Emami B, Grimm J, et al. Potential Clinical Significance of Overall Targeting Accuracy and Motion Management in the Treatment of Tumors That Move With Respiration: Lessons Learnt From a Quarter Century of Stereotactic Body Radiotherapy From Dose Response Models. *Front Oncol*. 2021;10:591430. doi:10.3389/fonc.2020.591430

79. Ohara K, Okumura T, Akisada M, et al. Irradiation synchronized with respiration gate. *Int J Radiat Oncol Biol Phys*. 1989;17(4):853-857. doi:10.1016/0360-3016(89)90078-3

80. Wölfelschneider J, Brandt T, Lettmaier S, Fietkau R, Bert C. Quantification of an external motion surrogate for quality assurance in lung cancer radiation therapy. *Biomed Res Int*. 2014;2014. doi:10.1155/2014/595430

81. Plathow C, Ley S, Zaporozhan J, et al. Assessment of reproducibility and stability of different breath-hold maneuvres by dynamic MRI: Comparison between healthy adults and patients with pulmonary hypertension. *Eur Radiol*. 2006;16(1):173-179. doi:10.1007/s00330-005-2795-9

82. Mampuya WA, Matsuo Y, Ueki N, et al. The impact of abdominal compression on outcome in patients treated with stereotactic body radiotherapy for primary lung cancer. *J Radiat Res*. 2014;55(5):934-939. doi:10.1093/jrr/rru028

83. Heinzerling JH, Anderson JF, Papiez L, et al. Four-Dimensional Computed Tomography Scan Analysis of Tumor and Organ Motion at Varying Levels of Abdominal Compression During Stereotactic Treatment of Lung and Liver. *Int J Radiat Oncol Biol Phys*. 2008;70(5):1571-1578. doi:10.1016/j.ijrobp.2007.12.023

84. Harrington RF. *Introduction to Electromagnetic Engineering.* New York,; 1958. Accessed June 9, 2021. http://hdl.handle.net/2027/mdp.39015004530591

85. Griffiths DJ (David J. Capacitors. In: 2nd ed.. Introduction to electrodynamics. Englewood Cliffs, N.J. : Prentice Hall; 1989:105.

86. Cole KS, Cole RH. Dispersion and absorption in dielectrics I. Alternating current characteristics. *J Chem Phys*. 1941;9(4):341-351. doi:10.1063/1.1750906

87. Zheng F, Tao J, Rappe AM. *Frequency-Dependent Dielectric Function of Semiconductors with Application to Physisorption*.; 2016.

88. Gabriel C, Gabriel S, y. E. Corthout. The dielectric properties of biological tissues: I. Literature survey. *Phys Med Biol*. 1996;41(11):2231.

89. MacDonald JR. Comparison of the universal dynamic response power-law fitting model for conducting systems with superior alternative models. *Solid State Ionics*. 2000;133(1):79-97. doi:10.1016/S0167-2738(00)00737-2

90. Chandra A, Bagchi B. Frequency dependence of ionic conductivity of electrolyte solutions. *J Chem Phys*. 2000;112(4):1876-1886. doi:10.1063/1.480751

91. Chandra A, Wei D, Patey GN. The frequency dependent conductivity of electrolyte solutions. *J Chem Phys*. 1993;99:234501. doi:10.1063/1.465274

92. Jonscher AK. The “universal” dielectric response. *Nature*. 1977;267(5613):673-679. doi:10.1038/267673a0

93. Peyman A. Dielectric properties of tissues. *ICEAA*. Published online 2009:863-864. doi:10.1109/ICEAA.2009.5297351

94. Schaefer M, Gross W, Ackemann J, Gebhard MM. The complex dielectric spectrum of heart tissue during ischemia. *Bioelectrochemistry*. 2002;58(2):171-180. doi:10.1016/S1567-5394(02)00152-4

95. Gabriel C, Peyman A, Grant EH. Electrical conductivity of tissue at frequencies below 1 MHz. *Phys Med Biol*. 2009;54(16):4863.

96. Gabriel C. *Compilation of the Dielectric Properties of Body Tissues at RF and Microwave Frequencies*.; 1996. http://niremf.ifac.cnr.it/docs/DIELECTRIC/Report.html

97. Singh S, Saha S. Electrical properties of bone. A review. *Clin Orthop Relat Res*. 1984;(186)(186):249-271.

98. Latikka J, Kuurne T, Eskola H. Conductivity of living intracranial tissues. *Phys Med Biol*. 2001;46(6):1611-1616. doi:10.1088/0031-9155/46/6/302

99. Baumann SB, Wozny DR, Kelly SK, Meno FM. The electrical conductivity of human cerebrospinal fluid at body temperature. *Biomed Eng IEEE Trans*. 1997;44(3):220-223. doi:10.1109/10.554770

100. Isaacson BM, Bloebaum RD. Bone bioelectricity: what have we learned in the past 160 years? *J Biomed Mater Res Part A*. 2010;95(4):1270-1279.

101. Gabriel C, Gabriel S, Corthout E. The dielectric properties of biological tissues: I. Literature survey. *Phys Med Biol*. 1996;41(11):2231-2249. doi:10.1088/0031-9155/41/11/001

102. Fish RM, Geddes LA. Conduction of electrical current to and through the human body: a review. *Eplasty*. 2009;9:e44.

103. Hamalainen MS, Sarvas J. Realistic conductivity geometry model of the human head for interpretation of neuromagnetic data. *IEEE Trans Biomed Eng*. 1989;36(2):165-171.

104. Vorwerk J, Cho J-H, Rampp S, Hamer H, Knösche TR, Wolters CH. A guideline for head volume conductor modeling in EEG and MEG. *Neuroimage*. 2014;100:590-607.

105. Michel E, Hernandez D, Lee SY. Electrical conductivity and permittivity maps of brain tissues derived from water content based on T1-weighted acquisition. *Magn Reson Med*. 2017;77(3):1094-1103.

106. Peyman A, Gabriel C, Grant EH. Complex Permittivity of Sodium Chloride Solutions at Microwave Frequencies. *Bioelectromagnetics*. 2007;28:264-274. doi:10.1002/bem.20271

107. Westerman W, Elias JG, Hedge A. Multi-touch: A new tactile 2-d gesture interface for human-computer interaction. In: *Proceedings of the Human Factors and Ergonomics Society Annual Meeting*. Vol 45. SAGE Publications Sage CA: Los Angeles, CA; 2001:632-636.

108. Togura T, Nakamura Y, Akashi K. Long-range human body sensing modules with electric field sensor. Published online 2008.

109. Valtonen M, Maentausta J, Vanhala J. Tiletrack: Capacitive human tracking using floor tiles. In: *Pervasive Computing and Communications, 2009. PerCom 2009. IEEE International Conference On*. IEEE; 2009:1-10.

110. Karlsson N. A capacitance sensor for safeguarding operators of industrial robots. *Robotica*. 1999;17(1):33-39.

111. Friedman WA, Bova FJ. Stereotactic radiosurgery. *Contemp Neurosurg*. 1989;11(12):1-8. doi:10.1227/00006123-199504000-00036

112. Harat M, Furtak J. Large In-mask Motion during Frameless Radiosurgery of a Brain Metastasis. *J Neurol Surg Part A Cent Eur Neurosurg*. Published online 2018.

113. Infusino E, Trodella L, Ramella S, et al. Estimation of patient setup uncertainty using BrainLAB Exatrac X-Ray 6D system in image-guided radiotherapy. *J Appl Clin Med Phys*. 2015;16(2):99-107.

114. Wiersma RD, Tomarken SL, Grelewicz Z, Belcher AH, Kang H. Spatial and temporal performance of 3D optical surface imaging for real-time head position tracking. *Med Phys*. 2013;40(11):111711-111712.

115. Zhao B, Maquilan G, Jiang S, Schwartz DL. Minimal mask immobilization with optical surface guidance for head and neck radiotherapy. *J Appl Clin Med Phys*. 2018;19(1):17-24.

116. Mancosu P, Fogliata A, Stravato A, Tomatis S, Cozzi L, Scorsetti M. Accuracy evaluation of the optical surface monitoring system on EDGE linear accelerator in a phantom study. *Med Dosim*. 2016;41(2):173-179.

117. Semiconductor F. Proximity Capacitive Touch Sensor Controller-Document number: MPR121. 2013;2018(February/15).

118. Spyker RL, Nelms RM. Classical equivalent circuit parameters for a double-layer capacitor. *IEEE Trans Aerosp Electron Syst*. 2000;36(3):829-836.

119. Show Y, Imaizumi K. Decrease in equivalent series resistance of electric double-layer capacitor by addition of carbon nanotube into the activated carbon electrode. *Diam Relat Mater*. 2006;15(11):2086-2089. doi:https://doi-org.ezproxy.library.dal.ca/10.1016/j.diamond.2006.08.004

120. Pawar SD, Murugavel P, Lal DM. Effect of relative humidity and sea level pressure on electrical conductivity of air over Indian Ocean. *J Geophys Res Atmos*. 2009;114(D2):D02205.

121. Matula RA. Electrical resistivity of copper, gold, palladium, and silver. *J Phys Chem Ref Data*. 1979;8(4):1147-1298.

122. Chang J, Yenice KM, Narayana A, Gutin PH. Accuracy and feasibility of cone-beam computed tomography for stereotactic radiosurgery setup. *Med Phys*. 2007;34(6Part1):2077-2084.

123. Dhabaan A, Schreibmann E, Siddiqi A, et al. Six degrees of freedom CBCT-based positioning for intracranial targets treated with frameless stereotactic radiosurgery. *J Appl Clin Med Phys*. 2012;13(6):215-225.

124. Guckenberger M, Baier K, Guenther I, et al. Reliability of the bony anatomy in image-guided stereotactic radiotherapy of brain metastases. *Int J Radiat Oncol Biol Phys*. 2007;69(1):294-301. doi:S0360-3016(07)00847-4 [pii]

125. Fontenot JD, Alkhatib H, Garrett JA, et al. AAPM Medical Physics Practice

Guideline 2. a: Commissioning and quality assurance of X-ray-based image-guided radiotherapy systems. *J Appl Clin Med Phys*. 2014;15(1):3-13.

126. Robar JL, Clark BG, Schella JW, Kim CS. Analysis of patient repositioning accuracy in precision radiation therapy using automated image fusion. *J Appl Clin Med Phys*. 2005;6(1):71-83.

127. Systems VM. TrueBeam Technical ReferenceGuide-Volume 2: Imaging. 2018(February/15).

128. Rahimian J, Chen JCT, Girvigian MR, Miller MJ, Rahimian R. Frame-based and frameless accuracy of Novalis® radiosurgery. In: Shaped Beam Radiosurgery. Springer; 2011:37-46.

129. Ahmadipour M, Ain MF, Ahmad ZA. A short review on copper calcium titanate (CCTO) electroceramic: synthesis, dielectric properties, film deposition, and sensing application. *Nano-Micro Lett*. 2016;8(4):291-311.

130. Balter JM, Wright JN, Newell LJ, et al. Accuracy of a wireless localization system for radiotherapy. *Int J Radiat Oncol*. 2005;61(3):933-937. doi:http://dx.doi.org.ezproxy.lib.ucalgary.ca/10.1016/j.ijrobp.2004.11.009

131. Willoughby TR, Kupelian PA, Pouliot J, et al. Target localization and real-time tracking using the Calypso 4D localization system in patients with localized prostate cancer. *Int J Radiat Oncol Biol Phys*. 2006;65(2):528-534. doi:S0360-3016(06)00253-7 [pii]

132. Sadeghi P, Lincoln J, Ruiz EAA, Robar JL. A novel intra-fraction motion monitoring system for stereotactic radiosurgery: proof of concept. *Phys Med Biol*. 2018;63(16):165019.

133. Semeniuk O, Sadeghi P, Farah JD, Moran K, Robar J. Performance optimization of capacitive motion sensing (CMS) system for intra-fraction motion detection during stereotactic radiosurgery. *Biomed Phys Eng Express*. 2020;6(1):015013. doi:10.1088/2057-1976/AB5BFF

134. Sadeghi P, Moran K, Robar JL. Capacitive monitoring system for real-time respiratory motion monitoring during radiation therapy. *J Appl Clin Med Phys*. 2020;21(9):16-24. doi:10.1002/acm2.12958

135. Gabriel C. No Title. *Compil Dielectr Prop Body Tissues RF Microw Freq*. Published online 1996.

136. Baxter LK. *Capacitive Sensors : Design and Applications*. New York : IEEE Press; 1997.

137. Kim N-H. *Introduction to Nonlinear Finite Element Analysis*. Boston, MA : Springer US : Imprint: Springer; 2015.

138. Bonse MHW, Mul C, Spronck JW. Finite-Element Modeling as a Tool for Designing Capacitive Position Sensors. *Sensors and Actuators A-Physical*. 1995;46(1-3):266-269. doi:10.1016/0924-4247(94)00903-U

139. Kunin M, Osaki Y, Cohen B, Raphan T. Rotation axes of the head during

positioning, head shaking, and locomotion. *J Neurophysiol*. 2007;98(5):3095-3108.

140. Cui S, Tseng H, Pakela J, Ten Haken RK, El Naqa I. Introduction to machine and deep learning for medical physicists. *Med Phys*. 2020;47(5):e127-e147. doi:10.1002/mp.14140

141. Lynam AL, Dennis JM, Owen KR, et al. Logistic regression has similar performance to optimised machine learning algorithms in a clinical setting: application to the discrimination between type 1 and type 2 diabetes in young adults. *Diagnostic Progn Res*. 2020;4(1). doi:10.1186/s41512-020-00075-2

142. Hsieh MH, Sun LM, Lin CL, Hsieh MJ, Hsu CY, Kao CH. Development of a prediction model for pancreatic cancer in patients with type 2 diabetes using logistic regression and artificial neural network models. *Cancer Manag Res*. 2018;10:6317-6324. doi:10.2147/CMAR.S180791

143. Schumacher M, Roßner R, Vach W. Neural networks and logistic regression: Part I. *Comput Stat Data Anal*. 1996;21(6):661-682. doi:10.1016/0167-9473(95)00032-1

144. Vach W, Roßner R, Schumacher M. Neural networks and logistic regression: Part II. *Comput Stat Data Anal*. 1996;21(6):683-701. doi:10.1016/0167-9473(95)00033-X

145. Stoltzfus JC. Logistic regression: A brief primer. *Acad Emerg Med*. 2011;18(10):1099-1104. doi:10.1111/j.1553-2712.2011.01185.x

146. Subasi A, Erçelebi E. Classification of EEG signals using neural network and logistic regression. *Comput Methods Programs Biomed*. 2005;78(2):87-99. doi:10.1016/j.cmpb.2004.10.009

147. Rifkin R, Klautau A. *In Defense of One-Vs-All Classification*. Vol 5.; 2004.

148. Rocha A, Klein Goldenstein S. Multiclass from Binary: Expanding One-Versus-All, One-Versus-One and ECOC-Based Approaches. *IEEE Trans NEURAL NETWORKS Learn Syst*. 2014;25(2). doi:10.1109/TNNLS.2013.2274735

149. Sammut C. *Encyclopedia of Machine Learning and Data Mining*. Springer; 2017.

150. Burghelea M, Verellen D, Dhont J, et al. Treating patients with Dynamic Wave Arc: First clinical experience. *Radiother Oncol*. 2017;122(3):347-351. doi:10.1016/j.radonc.2017.01.006

151. MacDonald RL, Robar JL, Thomas CG. Overlap-guided fixed-patient support positioning optimization for cranial SRT. *Med Phys*. 2017;44(1):17-27.

152. MacDonald RL, Thomas CG. Dynamic trajectory-based couch motion for improvement of radiation therapy trajectories in cranial SRT. *Med Phys*. 2015;42(5):2317-2325.

153. Pollock S, Keall R, Keall P. Breathing guidance in radiation oncology and radiology: A systematic review of patient and healthy volunteer studies. *Med Phys*. 2015;42(9):5490-5509. doi:10.1118/1.4928488 [doi]

154. Hess M, Buther F, Gigengack F, Dawood M, Schafers KP. A dual-Kinect approach to determine torso surface motion for respiratory motion correction in PET. *Med Phys*. 2015;42(5):2276-2286. doi:10.1118/1.4917163 [doi]

155. Mageras GS, Yorke E. Deep inspiration breath hold and respiratory gating strategies for reducing organ motion in radiation treatment. *Semin Radiat Oncol*. 2004;14(1):65-75. doi:S1053-4296(03)00090-0 [pii]

156. Bruzzaniti V, Abate A, Pinnaro P, et al. Dosimetric and clinical advantages of deep inspiration breath-hold (DIBH) during radiotherapy of breast cancer. *J Exp Clin Cancer Res*. 2013;32:88. doi:10.1186/1756-9966-32-88 [doi]

157. Molitoris JK, Diwanji T, 3rd JWS, et al. Optimizing immobilization, margins, and imaging for lung stereotactic body radiation therapy. *Transl lung cancer Res*. 2019;8(1):24-31. doi:10.21037/tlcr.2018.09.25 [doi]

158. Giraud P, Morvan E, Claude L, et al. Respiratory gating techniques for optimization of lung cancer radiotherapy. *J Thorac Oncol*. 2011;6(12):2058-2068. doi:10.1097/JTO.0b013e3182307ec2 [doi]

159. Garibaldi C, Catalano G, Baroni G, et al. Deep inspiration breath-hold technique guided by an opto-electronic system for extracranial stereotactic treatments. *J Appl Clin Med Phys*. 2013;14(4):14-25.

160. Schonecker S, Walter F, Freislederer P, et al. Treatment planning and evaluation of gated radiotherapy in left-sided breast cancer patients using the Catalyst(TM)/Sentinel(TM) system for deep inspiration breath-hold (DIBH). *Radiat Oncol*. 2016;11(1):143-145. doi:10.1186/s13014-016-0716-5 [doi]

161. Hoisak JDP, Pawlicki T. The Role of Optical Surface Imaging Systems in Radiation Therapy. *Semin Radiat Oncol*. 2018;28(3):185-193. doi:S1053-4296(18)30015-8 [pii]

162. Stock M, Kontrisova K, Dieckmann K, Bogner J, Poetter R, Georg D. Development and application of a real-time monitoring and feedback system for deep inspiration breath hold based on external marker tracking. *Med Phys*. 2006;33(8):2868-2877. doi:10.1118/1.2219775 [doi]

163. Worm ES, Hoyer M, Hansen R, et al. A Prospective Cohort Study of Gated Stereotactic Liver Radiation Therapy Using Continuous Internal Electromagnetic Motion Monitoring. *Int J Radiat Oncol Biol Phys*. 2018;101(2):366-375. doi:S0360-3016(18)30258-X [pii]

164. Wang Y, Yue S, Chen J, Li Q. Conductivity characteristics of human lung tissues. *Int J Imaging Syst Technol*. Published online 2021. doi:10.1002/ima.22607

165. Bodenham D. No Title. *Adapt Filter Chang Detect streaming data*. Published online 2012.

166. Desai N, Currey A, Kelly T, Bergom C. Nationwide Trends in Heart-Sparing Techniques Utilized in Radiation Therapy for Breast Cancer. *Adv Radiat Oncol*. 2019;4(2):246-252. doi:10.1016/j.adro.2019.01.001 [doi]

167. Oh SA, Yea JW, Kim SK, Park JW. Optimal Gating Window for Respiratory-

Gated Radiotherapy with Real-Time Position Management and Respiration Guiding System for Liver Cancer Treatment. *Sci Rep*. 2019;9(1):1-6.